



저작자표시-비영리-변경금지 2.0 대한민국

이용자는 아래의 조건을 따르는 경우에 한하여 자유롭게

- 이 저작물을 복제, 배포, 전송, 전시, 공연 및 방송할 수 있습니다.

다음과 같은 조건을 따라야 합니다:



저작자표시. 귀하는 원저작자를 표시하여야 합니다.



비영리. 귀하는 이 저작물을 영리 목적으로 이용할 수 없습니다.



변경금지. 귀하는 이 저작물을 개작, 변형 또는 가공할 수 없습니다.

- 귀하는, 이 저작물의 재이용이나 배포의 경우, 이 저작물에 적용된 이용허락조건을 명확하게 나타내어야 합니다.
- 저작권자로부터 별도의 허가를 받으면 이러한 조건들은 적용되지 않습니다.

저작권법에 따른 이용자의 권리는 위의 내용에 의하여 영향을 받지 않습니다.

이것은 [이용허락규약\(Legal Code\)](#)을 이해하기 쉽게 요약한 것입니다.

[Disclaimer](#)

공학박사 학위논문

고 레이놀즈 수 난류 2차 흐름
모사를 위한 PANS 모델 개선

**An improved partially-averaged Navier-Stokes model
for turbulent secondary flow at high Reynolds number**

2020년 2월

서울대학교 대학원
조선해양공학과
석우찬

고 레이놀즈 수 난류 2차 흐름
모사를 위한 PANS 모델 개선

지도교수 이 신 형

이 논문을 공학박사 학위논문으로 제출함
2020년 2월

서울대학교 대학원
조선해양공학과
석 우 찬

석우찬의 공학박사 학위논문을 인준함
2020년 2월

위 원 장 _____ (인)

부 위 원 장 _____ (인)

위 원 _____ (인)

위 원 _____ (인)

위 원 _____ (인)

Abstract

In the present study, modified formulations of the partially-averaged Navier-Stokes (PANS) model are suggested for accurate prediction of the turbulent secondary flow on the propeller plane of the KRISO Very Large Crude-oil Carrier (KVLCC2). The PANS simulations were performed using the open source Computational Fluid Dynamics (CFD) toolkit OpenFOAM, and the PANS results compared with the experimental data. Compared with the experimental data, the original PANS model under-estimated the intensity of the hook shape vortex on the propeller plane at a given level of grid resolution. The original PANS model uses the spatially varying f_k formulation proposed by Luo et al. (2014), depending on the grid scale and the integral length scale of turbulence. As the turbulence length scale is calculated from the transport equations for the unresolved turbulent kinetic energy and dissipation rate derived from the assumption that turbulence is locally isotropic, it is difficult to resolve the accurate hook shape contours of the streamwise component of velocity on the propeller plane. It is well known that the anisotropic turbulence models significantly improved the prediction of hook shape pattern of low velocity. As the turbulence anisotropy is important to resolve turbulent secondary flow, the Reynolds stress model and the algebraic Reynolds stress model were used in the modified PANS model. In addition, the f_k value was reduced in the region where the anisotropic behavior of turbulence dominated. The information on the region where there is highly anisotropic turbulence was procured using the budget analysis, and the anisotropy invariant map and the level of how much f_k should be reduced was determined by model constants.

To assess capability of the modified PANS models in predicting the secondary flow, the PANS simulations on sufficient grid resolution were performed for a square duct. The simulations showed good agreement with the previous DNS results. However, the grid resolution was too dense to use for the RANS simulation in the industry due to an excessive increase in computational cost. The comparatively coarse grid suitable for the RANS simulation was generated and used for the original PANS simulation. On the other hand, the original PANS simulation failed to capture the secondary flow near the corners of the square duct. The modified PANS models required a model constant, and the model constant was determined that could resolve the secondary flow in the square duct.

The hook shape pattern of low velocity on the propeller plane is produced by a stern bilge vortex created by the adverse pressure gradient due to the geometric variations of the afterbody. However, the generation mechanism of the secondary flow in the square duct is different from that of hook shape pattern of low velocity on the propeller plane. So, the reliability of the modified PANS models should be identified by applying to a simple geometry that represents the generation mechanism of the secondary flow by the pressure gradient. The modified PANS simulations of the turbulent flow around a prolate spheroid with a 10° angle of attack were conducted. The modified PANS results compared well with the experimental data for the pressure and skin friction coefficients. The modified PANS models well predicted the three-dimensional separated flow behind the prolate spheroid.

The modified PANS models were also applied to the flow around the KVLCC2 at drift angles of 0° and 12° . At the drift angle of 0° , statistical values of total resistance obtained by using the modified PANS models were in good agreement with experimental data. In addition, they showed an

improved prediction of the hook shape contours of the streamwise component of velocity as compared with the original PANS simulation. At the drift angle of 12° , the modified PANS models showed reliable results for the non-dimensional forces and moment. Moreover, they accurately resolve the vortical structures as well as hook shape contours of the streamwise component of velocity compared to the original PANS results.

Keywords: Secondary flow, Anisotropy, Partially-averaged Navier-Stokes, Turbulence model, Computational fluid dynamics (CFD)

Student number: 2016-37764

Table of Contents

Abstract	i
Table of Contents	iv
List of Tables	vi
List of Figures	vii
Chapter 1. Introduction	1
1.1. Background.....	1
1.2. Motivation.....	6
1.3. Theory and literature review	12
1.3.1. Overview of partially-averaged Navier-Stokes (PANS) equations.....	12
1.3.2. Reynolds-averaged Navier-Stokes (RANS) equations	19
1.3.3. Partially-averaged Navier-Stokes (PANS) equations	24
1.3.4. Reynolds stress model (RSM).....	30
1.3.5. Algebraic Reynolds stress model (ARSM)	34
1.3.6. Budget analysis	37
1.3.7. Anisotropy invariant map.....	40
1.4. Research objectives and outline of thesis.....	45
Chapter 2. Computational methods	47
2.1. Modified formulation of the PANS model	47
2.2. Simulation overview	53
2.2.1. Square duct.....	53
2.2.2. Prolate spheroid.....	58
2.2.3. KVLCC2	61

Chapter 3. Numerical validations.....	68
3.1. Preliminary tests.....	68
3.2 Turbulent square duct flow	71
3.2.1. Introduction.....	71
3.2.2. Results and discussion	75
3.3. Turbulent flow around a prolate spheroid.....	101
3.3.1. Introduction.....	101
3.3.2. Results and discussion	104
Chapter 4. Applications.....	108
4.1. Test model.....	108
4.2. Results and discussion for the case of $\beta = 0^\circ$	112
4.3. Results and discussion for the case of $\beta = 12^\circ$	135
Chapter 5. Summary and Conclusions	153
References	155
Abstract (Korean)	169

List of Tables

Table 1 Grid properties for the square duct simulations	55
Table 2 Main particulars of the KVLCC2.....	109
Table 3 Calculation of grid convergence index	113
Table 4 Non-dimensional total resistance coefficient at the drift angle of 0°	114
Table 5 Hydrodynamic forces and moments at the drift angle of 12°	137

List of Figures

Figure 1 Anisotropy invariant map	44
Figure 2 The formulation using the budget analysis.....	51
Figure 3 The formulation using the anisotropy invariant map	52
Figure 4 Computational domain for the square duct	54
Figure 5 Computational grids: (a) coarse grid; (b) medium grid; (c) fine grid	56
Figure 6 Computational domain for the prolate spheroid.....	59
Figure 7 Computational grid. Left: perspective view; Right: zoon in near the nose	60
Figure 8 Computational domain for $\beta = 0^\circ$ case: geometry and boundary conditions.....	62
Figure 9 Computational grids for $\beta = 0^\circ$ case: (a) find grid; (b) medium grid; (c) coarse grid	64
Figure 10 Computational domain for $\beta = 12^\circ$ case: geometry and boundary conditions	65
Figure 11 Computational grids for $\beta = 12^\circ$ case: (a) fine grid; (b) medium grid; (c) coarse grid.....	67
Figure 12 Comparison of the streamwise component of velocity on the propeller plane: (a) original PANS simulation, (b) experimental measurement	69
Figure 13 Instantaneous distribution of f_k from the original PANS results	69
Figure 14 Contours of the streamwise component of mean velocity with the secondary flow on the medium grid	76
Figure 15 Profiles of the stremwise component of mean velocity on the medium grid.....	78
Figure 16 Profiles of the lateral component of mean velocity on the medium	

grid.....	82
Figure 17 Profiles of the streamwise component of mean velocity on the fine grid.....	83
Figure 18 Profiles of the lateral component of mean velocity on the fine grid.....	84
Figure 19 Contours of the streamwise component of mean velocity with the secondary flow on the fine grid.....	86
Figure 20 Profiles of the streamwise component of mean velocity on the coarse grid.....	89
Figure 21 Profiles of the lateral component of mean velocity on the coarse grid.....	90
Figure 22 Contours of streamwise component of mean velocity with the secondary flow on the coarse grid.....	92
Figure 23 Profiles of the turbulence kinetic energy along the lower wall bisector.....	95
Figure 24 Computational grid for the RANS simulation: (a) Perspective view; (b) Front view.....	97
Figure 25 Contours of the streamwise component of velocity with the secondary flow from the oPANS results on the comparatively coarse grid.....	98
Figure 26 Contours of the streamwise component of velocity with the secondary flow from the mPANS results on the comparatively coarse grid.....	99
Figure 27 Contours of the streamwise component of velocity on cross-plane at $x/L = 0.9$ with 10 degree angle of attack.....	105
Figure 28 Comparison of pressure coefficient on the prolate spheroid.....	106
Figure 29 Comparison of skin friction coefficient on the prolate spheroid	107
Figure 30 The KVLCC2 hull form with the main particulars.....	109
Figure 31 Measured mean velocity fields on the propeller plane of the KVLCC2.....	111

Figure 32	Contours of the streamwise component of velocity and cross-plane vectors on the propeller plane from the $k - \omega$ SST model result	117
Figure 33	Radial and circumferential distributions of the streamwise component of velocity from the $k - \omega$ SST model results	118
Figure 34	Contours of the streamwise component of velocity and cross-plane vectors on the propeller plane from the RSM results.....	119
Figure 35	Radial and circumferential distributions of the streamwise component of velocity from the RSM results	120
Figure 36	Contours of the streamwise component of velocity and cross-plane vectors on the propeller plane from the oPANS results	122
Figure 37	Radial and circumferential distributions of the streamwise component of velocity from the oPANS results.....	123
Figure 38	Contours of the streamwise component of velocity and cross-plane vectors on the propeller plane from the PANS results with constant f_k values	125
Figure 39	Radial and circumferential distributions of the streamwise component of velocity from the PANS results with constant f_k values.....	126
Figure 40	Comparison of the results for the oPANS, mPANS-R and mPANS-A models. Left column: streamwise component of velocity; Right column: unresolved turbulence kinetic energy	129
Figure 41	Radial (left column) and circumferential (right column) distributions of the streamwise component of velocity from the oPANS, mPANS-R and mPANS-A results.....	130
Figure 42	The contours of the streamwise component of velocity and velocity vectors from the mPANS results	132
Figure 43	Radial (left column) and circumferential (right column) distributions of the streamwise component of velocity from the oPANS, mPANS results	133
Figure 44	Contours of the unresolved turbulent kinetic energy from the	

mPANS results	134
Figure 45 Contours of the streamwise component of velocity on the propeller plane at $x/L_{pp} = 0.48$ from the experimental data.....	135
Figure 46 Contours of the streamwise component of velocity on propeller plane from the RANS and oPANS results	139
Figure 47 Contours of the streamwise component of velocity on the propeller plane from the RANS, oPANS and mPANS-BR results.....	141
Figure 48 Contours of the streamwise component of velocity on the propeller plane from the mPANS-BA, mPANS-AR and mPANS-AA results	142
Figure 49 Vortex system around the hull from the RANS results. Left column: bottom view; Right column: zoom in near the stern.....	145
Figure 50 Vortex system around the hull from the oPANS results. Left column: bottom view; Right column: zoom in near the stern.....	146
Figure 51 Vortex system around the hull from the RANS, oPANS and mPANS-BR results. Left column: bottom view; Right column: zoom in near the stern.....	147
Figure 52 Vortex system around the hull from the mPANS-BA, mPANS-AR and mPANS-AA results. Left column: bottom view; Right column: zoom in near the stern.....	148
Figure 53 Bottom view of instantaneous skin friction lines from the RANS, oPANS and mPANS-BR, mPANS-BA, mPANS-AR and mPANS-AA results	150
Figure 54 Instantaneous skin friction lines near the bow from the RANS, oPANS and mPANS-BR, mPANS-BA, mPANS-AR and mPANS-AA results	151
Figure 55 Instantaneous skin friction lines near the stern from the RANS, oPANS and mPANS-BR, mPANS-BA, mPANS-AR and mPANS-AA results	152

Chapter 1. Introduction

1.1. Background

The most widely used turbulence model for investigating turbulent flow in many engineering applications is the Reynolds-averaged Navier-Stokes (RANS) models. Especially, as they provide reasonable accuracy at affordable computational requirements, hydrodynamic performance has been studied using the RANS approach with two-equation turbulence models and wall functions in the shipbuilding industries. In addition, a Rankine panel method was used for predicting the flow field around ships and propellers and presented reasonable results in normal operating conditions, i.e., straight and constant speed in design draft condition.

The international maritime organization (IMO) tightened regulations on exhaust emissions from ships. Since the energy efficiency operational indicator (EEOI) and the energy efficiency design index (EEDI) was made mandatory for new ships, many shipbuilding companies have been faced with the challenge of meeting the regulations. Accordingly, interests on a retrofit of a bulbous bow, retrofit of propeller, low-streaming, air lubrication system, and energy saving devices have increased.

In the shipbuilding industry, many studies have been investigated using the RANS models. Although the RANS models have been applied successfully in many ship hydrodynamic analyses and yielded accurate predictions in time-averaged flow characteristics, they failed to resolve unsteady coherent structures and highly complex phenomena such as separation, re-circulation, and unsteady vortex shedding. (Gaggero *et al.*, 2017; Carrica *et al.*, 2006;

Gaggero *et al.*, 2014; Li, 2006). The RANS simulations attempt to model not only small scale turbulent motions but also fluctuating scales of motion with one-point closure. Besides, the turbulent eddy viscosity based on two-equation closure models is over-estimated, resulting in large damping of the unsteady motion. Therefore, two-equation RANS models predict inaccurate results of turbulence characteristics in complex flow fields, especially where the turbulent flow is highly anisotropic.

Two-equation closure models use the Boussinesq hypothesis to calculate the eddy viscosity from the turbulent kinetic energy (k) and either the dissipation rate (ϵ) or the frequency (ω). Unlike two-equation RANS models that employ an isotropic eddy viscosity, the Reynolds stress model (RSM) solves the transport equations for six independent Reynolds stresses that describe the evolution of individual components of the Reynolds stress tensor. The RSM can account for the directional effects of the Reynolds stresses and complex interactions in turbulent flow, leading to better results than the eddy viscosity models. In addition, the RSM can accurately resolve the return to isotropy of turbulence observed in decaying turbulent flow and yield the behavior of turbulent flow in the rapid distortion limit.

Although the RSM simulations have been able to capture the unsteady coherent structures and represent too complex phenomena more correctly than two-equation RANS models, turbulence quantities were not completely satisfactory comparing with experimental data. The disagreement is probably due to modeling the diffusion, dissipation and pressure-strain correlation terms (Madabhushi and Vanka., 1991). As the RSM depends on the accuracy of the models for the terms, it is difficult to represent them with a high degree of accuracy.

High-fidelity numerical simulations such as the direct numerical simulation (DNS) and the large eddy simulation (LES) should be applied to overcome the limitations of the isotropic turbulence models in two-equation RANS models and reduce the error caused by modeling the diffusion, dissipation and pressure-strain correlation terms in the RSM simulation. As the DNS requires high computational cost, even low Reynolds number and at the finest grids near the wall to resolve all scales of motion, applications of the DNS to high Reynolds number flows around the simple engineering models is limited.

With the rapid advancement of computational power, high-fidelity numerical simulations have been conducted, which demand an extreme cost in terms of computer resources. The DNS numerically solves the Navier-Stokes equations without any turbulence models and can present mean flows and all turbulent velocity fluctuations. Since the DNS resolves all the time and length scales, the spatial grid should be sufficiently fine that can resolve the Kolmogorov length scale at which viscosity dominates, and the turbulent kinetic energy is dissipated into heat. Time steps are also sufficiently small to resolve the smallest turbulent eddies and the fastest fluctuations. If the grid size is not small enough, the energy cascade between large scale eddy and small scale eddy cannot be properly resolved, making the turbulence statistics unpredictable. To accurately simulate the turbulent flow, the DNS has to make the comparatively fine grid at the level of $y^+ \leq 0.1$ on the wall. As the Reynolds number increases, the number of grids required for the DNS increases exponentially in proportion to $Re^{37/14}$, where $Re = UL/\nu$, U is the free-stream velocity, L is the integral scale and ν is the kinematic viscosity (Kim *et al.*, 1987; Spalart 1988; Schlatter *et al.*, 2009).

On the other hand, the DNS requires the extraordinary computational

resource for high Reynolds number flow and too expensive as far more resolved scales are observed. The LES is a preferred method for predicting turbulent flow in which the Reynolds number is too high to apply the DNS and analyzes the flow field by applying spatial filtering to the Navier-Stokes equations. The small size isotropic eddies that are not filtered are estimated by the sub-grid scale (SGS) model. Moreover, the large scales which represent the anisotropic part of the energy spectrum and contain most of the energy are calculated directly (Pope 2000). However, for the simulation of the anisotropic turbulence structures caused by the shear stresses on the wall, the grid spacing of the streamwise direction $\Delta x^+ \approx 50 \sim 150$, the wall normal direction, $\Delta y^+ \leq 1$, and the spanwise direction $\Delta z^+ \approx 15 \sim 40$ should be maintained near the wall. Therefore, like the DNS, the LES also requires the number of grid points in proportion to $Re^{13/7}$ (Choi and Moin, 2012).

Despite recent fast development in high performance computing, it is still expensive for the LES to be widely used in many engineering applications. In addition, the LES requires the excessive computing power requirement for numerical simulations of the high Reynolds number turbulent flows. Catalano *et al.* (2003) represented that the required number of grids for the LES is nearly the same as for the DNS to resolve the small eddies which have essential information near the wall. Recently, a wall-modeled LES that can be applied at $\Delta y^+ \approx 10 \sim 50$ in the normal direction to the wall was proposed to alleviate the grid density near the wall, but it is not widely used.

In highly complex flows such as separation, reattachment, unsteady vortex shedding, and coherent vortical structures, the RANS simulations reproduce physically inadequate results, and the LES requires excessive computing power. There is a need for a numerical approach that provides an adequate description of large scale unsteady flow structures by resolving fluctuating

scales. As such, several hybrid RANS/LES approaches, which combine the advantages of RANS and LES aiming at computing highly complex flows accurately with a reasonable computational resource, were proposed. The representative hybrid RANS/LES are detached eddy simulation (DES). The DES was introduced by Spalart *et al.* (1997), which can explicitly resolve turbulent flow structures for massively separated flow at high Reynolds number (Strelets, 2001). In the DES, regions near the wall where the turbulent length scale is small are treated using the RANS model, and the detached eddies in the far field were simulated by the LES. It provides a suitable description of the near wall flow in a statistical sense which does not require fine grid resolution. So, the DES reduces the considerably computational cost by alleviating the near wall grid requirements and provides accurate results over the RANS models by predicting massively separated flow. However, the analysis of turbulent channel flow using the DES showed that the free stream velocity distribution could be severely distorted at the boundary between the region dominated by the RANS model and the region dominated by the sub-grid scale model of the LES (Nikitin *et al.*, 2000). In other words, it was shown that the unphysical flow field could be simulated depending on the grid structures in the DES.

1.2. Motivation

The flow around ships is extremely complex because the interface between air and water, high Reynolds number flow, and significant change of wake characteristics exist. Besides, turbulent anisotropy and unsteady three-dimensional turbulent flow exist around ships. Nevertheless, early analytical and experimental investigations were focused on the prediction of ship resistance and propulsion performance. Rankine panel methods gave sufficient accuracy for predicting the ship resistance and wave pattern created by ships (Nakos and Sclavounos, 1990; Newman, 1987). However, this method failed to accurately predict the flow at the stern, where three-dimensional flow structures and thickened boundary layer flow along the hull surface existed and were convected downstream in the wake. The flow to the propeller in the wake region causes both unbalanced bearing forces and dynamic change in the pressure distribution on the propeller surface. The propeller cavitation could cause many unexpected consequences: noise, cavitation erosion, and vibration. The cavitation produces pressure fluctuation and vibration, which show that cavity volume variations are the main source of ship vibration (Huse., 1972). In addition, when subjected to higher pressure, the cavitation bubbles collapse and produce shock waves, leading to noise. If the cavitation collapses on the propeller surface, propeller erosion could occur. These phenomena have been investigated from model tests in a cavitation tunnel using full scale wake field obtained from CFD simulation results. As a propeller cavitation behavior is strongly influenced by propeller inflow, accurate wake description is essential for predicting the propeller cavitation performance.

The damage of a propeller shaft bearing increased significantly in the early 1990s. The main reason for the bearing damage was estimated that the thrust

eccentricity was not considered in shaft alignment (Vartdal *et al.*, 2009). Recently, thrust eccentricity, which is caused by three-dimensional non-uniform wake, is considered in shaft alignment. Shin (2015) also proposed that thrust eccentricity in turning conditions should be considered in shaft alignment to prevent shaft bearing damage. Therefore, it is crucial to accurately predict the non-uniform wake for shaft alignment and predicting the propeller cavitation performance. Ghassemi (2009) showed the influence of the wake on propeller performance. The different inflow produced different pressure fluctuations for the same propeller, resulting in fluctuating thrust and torque with time. Therefore, it is crucial to predict the wake accurately. To assess state of the art in CFD for ship hydrodynamic applications and discuss the numerical results obtained from different method results, many research groups participated in CFD workshops such as Gothenburg 2000 and Tokyo 2005. Many research groups performed the computational benchmark tests for the KVLCC2. As the KVLCC2 has a U shaped stern, complex flow features such as separation, reattachment, unsteady vortex shedding, and three-dimensional flow structures are observed when compared with the flow around the other ships.

Most computational studies for the KVLCC2 focused on the prediction of the propeller plane wake, resistance, and moment. In particular, capturing the hook shape pattern of low velocity created by the bilge vortex was of primary interest. The bilge vortex is resulting in a pair of vortices, which are caused by a three-dimensional vortex flow separation. A pair of vortices is generated as the flows from the port side or starboard side and bottom of the ship meet at the curved surface between the bottom and side of the hull. These are usually strong and gradually developed into the wake. So, they significantly cause vibration, noise and cavitation and decrease the efficiency of the propeller.

Vibration and noise are essential for many ships due to the requirement for crew comfort. In particular, vibration and noise are crucial for naval vessels to prevent detection from enemies. Cavitation causes severe propeller blade erosion, and tip vortices away from the blade tip damage the rudder. Besides, the propulsion efficiency decreases with increasing cavitation phenomena. Thus, it is crucial to predict the bilge vortices accurately.

However, a great number of results for the KVLCC2 in Tokyo 2005 CFD workshop could not capture the hook shape contours of the streamwise component of velocity. The reason for the failure to capture the hook shape contours was much debated at the workshop. Deng *et al.* (1994) showed that the turbulence model with low values of eddy viscosity predicted a reasonably accurate distribution of the streamwise component of velocity with hook shape pattern. The isotropic two-equation turbulence models over-predicted the eddy viscosity, which results in excessive damping of unsteady motion. Larsson *et al.* (2003) reported that the simulation based on the isotropic turbulence models failed to resolve the hook shape pattern of low velocity on the propeller plane due to the fact that the flow around a ship showed turbulence anisotropy generated by the free-surface; the streamwise component of turbulence normal stresses ($\overline{u'u'}$) is more than twice larger than the cross-stream stresses ($\overline{v'v'}$, $\overline{w'w'}$). Kim *et al.* (2002) used several two-equation models, such as the standard $k - \epsilon$ model (SKE), the RNG $k - \epsilon$ model (RNG), and the realizable $k - \epsilon$ model (RKE) to identify the wake flow difference according to the turbulence model. The numerical simulations were performed for the KVLCC2 with the scale ratio of 1/58, and the calculated results were compared with the experimental data. The SKE and RNG failed to predict the distribution of streamwise component of velocity with the hook shape pattern, and RKE showed a slight difference in the nominal wake.

As described above, as the isotropic turbulence models over-predicted eddy viscosity, they failed to account for the unsteady fluctuations in the flow field and hence were inadequate turbulence models to resolve the hook shape contours of the streamwise component of velocity on the propeller plane. Larsson *et al.* (2003) identified that the anisotropic turbulence model, such as the RSM, well resolves the details of the nominal wake flow pattern for the KVLCC2. The anisotropic turbulence models for both mean velocity and turbulence quantities presented the details of the nominal wake for the KVLCC2 at the Tokyo 2005 CFD Workshops. The DES simulations for two unsteady flows around the KVLCC2 and KCS were performed by Carrica *et al.* (2010). In the medium resolution case, the DES captured the complex flows for free surface, vortical structures, and other local flow features. Moreover, the agreement of the DES calculations for the velocity contours was reasonable when compared with the experimental data. Gaggero *et al.* (2017) used a coupled RANS/BEM approach for the evaluation of the performance in self-propulsion conditions. They achieved satisfactory estimations of the self-propulsion data and identified that the predicted nominal wakes compared well with experimental measurements when the anisotropic turbulence models were employed.

The results obtained by using the anisotropic turbulence models greatly improved the prediction of force, turbulence quantities, and local flow over isotropic models for a straight ahead condition. More recently, the anisotropic turbulence models were used for oblique conditions. Ships operate in various oblique conditions because of environmentally induced motions, such as waves, wind and currents, and maneuvering. In these circumstances, wake characteristics are significantly changed, and noticeable asymmetric wake distribution is observed. Consequently, the wake characteristics unexpectedly

increase the thrust and torque of the propeller and produce an additional propeller eccentricity. Moreover, further stresses appear at the blade hub, shaft, energy saving devices, and hull stern, which can amplify the cavitation, vibration, and erosion phenomena. For these reasons, a deeper understanding of the three-dimensional complex flow in the wake of ships under maneuvering operations is also important.

For the KVLCC2 at different drift angles, many studies have been carried out using CFD approaches based on hybrid RANS/LES methods. Ismail *et al.* (2010) performed CFD simulations for the KVLCC2 at the drift angles of 0° , 10° and 30° using the blended $k - \varepsilon/k - \omega$ (BKW) model and the algebraic Reynolds stress model (ARSM). The ARSM improved the prediction of resistance and turbulent quantities when compared with the BKW model. In particular, capturing the hook shape contours of the streamwise component of velocity was significantly improved. Pereira *et al.* (2017) used the explicit algebraic Reynolds stress model (EARSM) and the isotropic eddy viscosity model to investigate the quantification of numerical and modeling errors for the results of the flow around the KVLCC2. The EARSM estimated small numerical uncertainties of the resistance coefficient, and the hook shape pattern of low velocity was more clearly visible on the propeller plane over the eddy viscosity model.

For oblique flow, however, integral quantities such as forces and moments were over-predicted using the anisotropic turbulence models compared to experimental data (Hino, 2015). In addition, when the drift angle was large, more massive vortical and turbulent structures separated from the hull existed in the wake field. For an accurate prediction of the vortical and turbulent flow structures, a high fidelity turbulence model is required, such as the LES, but it demands too much computational cost for resolving wall-bounded flows at the

high Reynolds number. Therefore, a hybrid RANS/LES emerged with an aim to compute unsteady complex vortical structures with high accuracy and meanwhile at moderate computational resources. Fureby *et al.* (2016) investigated the detailed flow field around the KVLCC2 in the oblique condition using the RANS model, LES, and hybrid RANS/LES. With the increase of drift angle, fairly complex vortex systems such as Kelvin-Helmholtz instabilities, von-Karman vortex shedding, and helical instabilities were captured. The simulation results were compared against each other. At the drift angle of 0° , they predicted similar overall features. However, at drift angles of 12° and 30° , the hybrid RANS/LES and LES simulations provided the most accurate results for the streamwise component of velocity on the propeller plane and complex vortex system compared with the RANS results. Xing *et al.* (2012) examined the flow past the KVLCC2 for identifying vortical and turbulent flow structures using the DES at drift angles (β) of 0° , 12° and 30° . For $\beta = 0^\circ$ case, the DES showed significantly improved prediction of the resistance and hook shape contours of the streamwise component of velocity compared to the experiment. $\beta = 12^\circ$ and 30° cases, they showed complex vortical structures, such as aft-body side vortex, bilge vortex, and contours of the streamwise component of velocity.

1.3. Theory and literature review

1.3.1. *Overview of partially-averaged Navier-Stokes (PANS) equations*

Numerical analysis of unsteady turbulent flow that resolves the large fluctuating scales at a reasonable computational cost is essential in many engineering applications. Speziale (1998) proposed a new turbulence model that changes seamlessly from RANS to DNS with respect to the numerical resolution. It functions as the RANS model, when the cut-off wavenumber is in the largest scales, and as the DNS if all relevant scales are resolved. Germano (1999) suggested the idea of bridging between RANS and LES by introducing a new LES definition that should be more flexible and compatible with the RANS approach. It is known as a bridging model. Contrary to the bridging model, a zonal model divides a computational domain into two modeling regions, such as the RANS model near the wall and the LES in the rest of the domain. An essential drawback of the zonal model is how to deal with the interface between different turbulence models.

Girimaji (2006) proposed a new bridging model that can vary seamlessly between RANS and DNS. It provides the best possible fidelity on a given level of physical resolution and improves accuracy with increasing resolution. The bridging model is known as the PANS. The degree of resolution is determined by specifying the value of the filter control parameters, which serves the same function as a cut-off wavenumber in the LES. The extent of filtering is quantified by the statistical parameters, which are the ratio of unresolved-to-total kinetic energy (f_k) and the ratio of unresolved-to-total dissipation rate (f_ε). With $f_k = 1$, all the turbulent kinetic energy of the flow field is modeled, and the PANS model reproduces RANS results. On the other hand, the PANS simulation with $f_k = 0$ provides the DNS results due to resolving all

turbulent kinetic energy. In high Reynolds number flows, the dissipation scales are not resolved, hence $f_\varepsilon = 1$. However, as the dissipation scales are resolved in low Reynolds number, the parameter f_ε is close to 0. So, the physical resolution is independent of the numerical resolution. As the f_k decreases, the eddy viscosity of unresolved scales decreases, leading to more resolved scales of motion and improving the accuracy.

The PANS models have been successfully used in separated flow problems such as flow past a square cylinder (Girimaji, 2006; Jeong and Girimaji, 2010) and circular cylinder (Lakshmi pathy and Girimaji, 2010; Lakshmi pathy and Togiti, 2011; Luo *et al.*, 2014), flow over a backward facing step (Frendi *et al.*, 2006). Jeong and Girimaji (2010) carried out the PANS simulations of the flow past a square cylinder at $Re = 22,000$. Three different values of f_k ($= 1.0, 0.7$ and 0.4) were used as a spatial constant value and the computed results compared with the experimental data and LES results. With decreasing f_k , more resolved scales of motion and fluctuation were captured, and the integrated values, such as drag and lift got closer to the experimental data. Lakshmi pathy and Girimaji (2010) used the PANS model based on $k - \varepsilon$ for simulation of flow past a circular cylinder at $Re_D = 140,000$. Their simulations were conducted with three different f_k values ranging from 0.5 to 0.7. As the f_k decreases, more and more unsteady and three-dimensional flow structures were resolved, and the PANS simulations with the smaller f_k value yielded an improved characterization of the wake structure behind the circular cylinder. Also, the mean velocity in the wake region and pressure on the cylinder surface were reasonable when compared with the experimental data. Lakshmi pathy and Togiti (2011) performed the PANS simulations with different f_k values (0.5, 0.7, and 1.0) and DES simulation of flow past a circular cylinder at $Re_D = 140,000$. The numerical results compared with

experimental data and LES results, and they showed considerable discrepancies in drag coefficient when using $f_k = 0.5$. Moreover, with decrease f_k value from 1.0 to 0.5, the velocity defects were in agreement with the experimental data, but the PANS simulation with $f_k = 0.5$ under-predicted the velocity defect. Flow past a backward facing step was computed by Frendi *et al.* (2006) to investigate the effects of varying f_ε using the DES, URANS, and PANS models. The PANS results were similar to the experimental data better than the DES and URANS models on the same grid. Decreasing f_ε had the effect of lowering the Reynolds number. The PANS simulations showed that the range of resolved fluctuations decreased with decreasing f_ε .

As the $k - \varepsilon$ PANS model was derived based on the standard $k - \varepsilon$ RANS model, the turbulent shear stresses were over-estimated in the boundary layer in an adverse pressure gradient. Accordingly, there is a problem of suppressing the separation on the wall (Peyret and Krause, 2000). To overcome the shortcomings, Wilcox (1988, 1993) proposed the $k - \omega$ model, using the turbulent frequency ($\omega = \varepsilon/k$). The $k - \omega$ model was proved to be numerically more stable than the $k - \varepsilon$ model. In addition, it does not need wall damping functions compared to the $k - \varepsilon$ model and then well predicts the boundary layer. Therefore, many researchers are interested in the $k - \omega$ model for well predicting the boundary layer. Lakshimipathy and Girimaji (2006) introduced the PANS model based on $k - \omega$ and performed the simulation for the flow past a circular cylinder at $Re = 1.4 \times 10^5$. The numerical results were compared with those of $k - \varepsilon$ PANS model, LES, and experimental data. The PANS model based on $k - \omega$ with $f_k = 0.5$ predicted mean pressure distribution over the cylinder surface and streamwise component of velocity in the near wake region with higher accuracy than the

$k - \varepsilon$ PANS model. Moreover, the PANS predictions for the retarded stagnation point and the Strouhal number showed good agreement with the experimental data and LES results.

From the results mentioned above, the value of the filter control parameter (f_k) was kept constant throughout the whole computational domain. However, the optimum value of f_k can hardly be determined in advance of numerical analysis. So, spatially varying and dynamic update of f_k are reasonable as the degree of resolution is altered in different regions depending on the local grid size and flow information. Girimaji and Abdol-Hamid (2005) proposed a spatially varying function of f_k depending on the grid scale and the integral length scale of turbulence. The smallest resolved length scale was assumed to be the Kolmogorov length scale, and the proposed function was written as

$$f_k = \frac{1}{\sqrt{C_\mu}} \left(\frac{\Delta}{\Lambda} \right)^{\frac{2}{3}} \quad (1)$$

where C_μ is 0.09 which is the same as in the RANS simulation based on $k - \varepsilon$ model and Δ is the smallest grid dimension, defined as $\Delta = (\Delta x \times \Delta y \times \Delta z)^{1/3}$. Λ is the turbulence length scale, given by

$$\Lambda = \frac{k^{3/2}}{\varepsilon}. \quad (2)$$

The test case was an axisymmetric jet with a nozzle at Mach number of

0.55. The PANS results with spatially varying f_k were much closer to the experimental data than the RANS results. In addition, it showed that the turbulent kinetic energy was quite similar to the experimental data and most of the turbulent kinetic energy was resolved at the given level of grid size. Song and Park (2009) derived the spatially varying f_k function assuming that the grid spacing used for the PANS simulation exists between the integral length scale and the Kolmogorov length scale. The two-stage approach which Abdoal-Hamid and Girimaji (2004) introduced was used to determine the f_k value. This approach determined the appropriate grid system for the PANS simulation based on the turbulence length scales which was obtained from the RANS results. Song and Park (2009) performed the PANS simulation of the flow past a square cylinder. The RANS simulations were performed for the first time to estimate the turbulence length scale and then f_k was determined using the calculated length scale for the initial distribution. In the PANS simulation, f_k was updated according to the following function

$$f_k = \left(\frac{\Delta}{\eta}\right)^{2/3} \left[1 - \left(\frac{\eta}{\Delta}\right)^{2/3}\right] \left(\frac{\eta}{l_{turb}}\right)^{2/3} \quad (3)$$

The length scales in Eq. (3) are expressed as

$$l_{turb} = \frac{k_u^{1/2}}{\beta^* \omega_u}, \quad \eta = \left(\frac{\nu^3}{\varepsilon_u}\right)^{1/4} = \left(\frac{\nu^3}{\beta^* \omega_u k_u}\right)^{1/4} \quad (4)$$

where k_u and ω_u are the unresolved turbulent kinetic energy and

unresolved turbulent frequency, respectively.

With the reduced grid spacing, more coherent structures around the square cylinder were resolved and the PANS results with constant f_k less than about 0.5 were in good agreement with the experimental data.

Luo *et al.* (2014) introduced the formulation of spatial change of f_k as follows

$$f_k = \min \left[C_{PANS} \left(\frac{\Delta}{l_u} \right)^{2/3}, 1 \right] \quad (5)$$

$$l_u = \frac{\sqrt{k_u}}{\beta^* \omega_u} \quad (6)$$

where l_u is the unresolved turbulent length scale and C_{PANS} is an arbitrary constant. They used 0.1 for the C_{PANS} which is needed to be calibrated according to the analysis conditions. Luo *et al.* (2014) performed the PANS simulations of the flow past a circular cylinder at $Re = 3900$ and $Re = 1.4 \times 10^5$ using constant f_k values and variable f_k function. DES simulations were also conducted for comparisons. For a low Reynolds number case, the integral flow quantities predicted by the PANS model with the smallest f_k value and spatially varying f_k were in good agreement with the experimental data and DES results. At high Reynolds number, DES and variable f_k PANS simulations well predicted the flow quantities. On the other hand, the PANS simulation with the smallest constant f_k over-predicted the flow quantities in a high Reynolds number flow. Therefore, the PANS simulations with low value of constant f_k do not always provide well-

predicted results.

A new formulation for spatially varying f_k was developed considering the energy spectrum $E(k)$ by Foroutan and Yavuzkurt (2014). The total turbulent kinetic energy (k) can be obtained by integrating the energy spectrum in the entire range of wavenumbers while the resolved turbulent kinetic energy was calculated by integrating the energy spectrum to the cut-off wave number. The proposed f_k function can be expressed as follows

$$f_k = 1 - \left[\frac{\left(\frac{\Delta}{\Delta}\right)^{2/3}}{\left(\frac{C_k}{(1+s)\pi^{2/3}} + \left(\frac{\Delta}{\Delta}\right)^{2/3}\right)} \right]^{\frac{3}{2}(1+s)} \quad (7)$$

where C_k and s are constants. The new PANS model showed lower value of f_k than the previous formula near the wall. So, it resolved more turbulent motions in unsteady turbulent flow.

1.3.2. Reynolds-averaged Navier-Stokes (RANS) equations

The incompressible Navier-Stokes equations in conservation forms are

$$\frac{\partial u_i}{\partial x_i} = 0 \quad (8)$$

$$\frac{\partial u_i}{\partial t} + \frac{\partial}{\partial x_j} (u_i u_j) = -\frac{1}{\rho} \frac{\partial p}{\partial x_i} + \nu \frac{\partial^2 u_i}{\partial x_j \partial x_j} \quad (9)$$

where u_i is the fluid velocity, p is the pressure and ν is the fluid kinematic viscosity. Reynolds decomposition refers to separation of the flow variable into the mean (time-averaged) components (\bar{u}_i, \bar{p}) and the fluctuating component (u'_i, p') as

$$u_i = \bar{u}_i + u'_i \quad (10)$$

where the bar denotes the time average.

By substituting Eq. (10) into Eq. (8) and (9), the averaged continuity and momentum equations can be written as

$$\frac{\partial \bar{u}_i}{\partial x_i} = 0 \quad (11)$$

$$\frac{\partial \bar{u}_i}{\partial t} + \frac{\partial}{\partial x_j} (\bar{u}_i \bar{u}_j) = -\frac{1}{\rho} \frac{\partial \bar{p}}{\partial x_i} + \nu \frac{\partial^2 \bar{u}_i}{\partial x_j \partial x_j} - \frac{\partial}{\partial x_j} (\overline{u'_i u'_j}) \quad (12)$$

where $\tau_{ij} = -\overline{u'_i u'_j}$ is known as the Reynold stress tensor which is symmetric and has six independent components. The system of equations is not a closed system for the calculation of the four dependent variables (\overline{u}, p) and six additional independent unknowns ($\overline{u'_i u'_j}$). To close the Reynolds-averaged Navier-Stokes equations, the Reynolds stress term should be appropriately modeled. A common method employs the Boussinesq assumption.

In 1877, Boussinesq proposed that the Reynolds stress tensor, τ_{ij} , is proportional to the mean strain rate tensor, S_{ij} . This is called the Boussinesq assumption or hypothesis and leads to the eddy viscosity model for the Reynolds stresses.

$$\tau_{ij} = 2\nu_t S_{ij} - \frac{2}{3}k\delta_{ij} \quad (13)$$

where k is the turbulent kinetic energy given by $k = (\overline{u'^2} + \overline{v'^2} + \overline{w'^2})/2$ and ν_t is the turbulent eddy viscosity assumed as an isotropic scalar quantity. S_{ij} is the mean strain rate tensor:

$$S_{ij} = \frac{1}{2} \left(\frac{\partial \overline{u}_i}{\partial x_j} + \frac{\partial \overline{u}_j}{\partial x_i} \right) \quad (14)$$

There are classical turbulence models, such as zero equation, one-equation, two-equation and seven-equation models. Among the turbulence models, two equation turbulence models such as the $k - \varepsilon$ and $k - \omega$ shear stress

transport (SST) are commonly used for most type of engineering applications.

In the flow where convection and diffusion cause significant difference between production and destruction of turbulence, a simple algebraic model, such as the mixing length model is not acceptable. So, the $k - \varepsilon$ model was introduced by Launder and Spalding (1983) and focused on the mechanisms that affect the turbulent kinetic energy. This model has two transport equations, one for the turbulent kinetic energy (k) and the other for the turbulent dissipation rate (ε) as follows

$$\frac{\partial k}{\partial t} + \bar{u}_j \frac{\partial k}{\partial x_j} = P_k - \varepsilon + \frac{\partial}{\partial x_j} \left[\left(\nu + \frac{\nu_t}{\sigma_k} \right) \frac{\partial k}{\partial x_j} \right] \quad (15)$$

$$\frac{\partial \varepsilon}{\partial t} + \bar{u}_j \frac{\partial \varepsilon}{\partial x_j} = C_{\varepsilon_1} P_k \frac{\varepsilon}{k} - C_{\varepsilon_2} \frac{\varepsilon^2}{k} + \frac{\partial}{\partial x_j} \left[\left(\nu + \frac{\nu_t}{\sigma_\varepsilon} \right) \frac{\partial \varepsilon}{\partial x_j} \right] \quad (16)$$

where ν_t represents the eddy viscosity , which can be expresses by

$$\nu_t = C_\mu \frac{k^2}{\varepsilon} \quad (17)$$

The $k - \varepsilon$ model contains five parameters; the most commonly used values are

$$C_{\varepsilon_1} = 1.44, C_{\varepsilon_2} = 1.92, C_\mu = 0.09, \sigma_k = 1.0, \sigma_\varepsilon = 1.3 \quad (18)$$

where the value of C_μ is chosen to give results consistent with the law of the wall.

Menter (1992) showed that the results of the $k - \varepsilon$ model near wall are unsatisfactory for boundary layer with adverse pressure gradients. To overcome these problems, he suggested a hybrid model, called $k - \omega$ SST, that $k - \omega$ model is applied in the near wall region and $k - \varepsilon$ model is used in the fully turbulent region far from the wall (Menter, 1994, 1997). The Reynolds stress and turbulent kinetic energy transport equations are the same as in Wilcox's $k - \omega$ model (1988), but the transport equation for turbulence frequency (ω) is expressed by substituting $\varepsilon = k\omega$.

$$\frac{\partial k}{\partial t} + \bar{u}_j \frac{\partial k}{\partial x_j} = P_k - \varepsilon + \frac{\partial}{\partial x_j} \left[\left(\nu + \frac{\nu_t}{\sigma_k} \right) \frac{\partial k}{\partial x_j} \right] \quad (19)$$

$$\begin{aligned} \frac{\partial \omega}{\partial t} + \bar{u}_j \frac{\partial \omega}{\partial x_j} = & \alpha \frac{\omega}{k} P - \beta \omega^2 + \frac{\partial}{\partial x_j} \left[\left(\nu + \sigma_\omega \nu_t \right) \frac{\partial \omega}{\partial x_j} \right] \\ & + 2(1 - F_1) \sigma_{\omega_2} \frac{1}{\omega} \frac{\partial k}{\partial x_i} \frac{\partial \omega}{\partial x_i} \end{aligned} \quad (20)$$

where ν_t represents the eddy viscosity, which can be expressed by

$$\nu_t = \frac{a_1 k}{\max(a_1 \omega, SF_2)} \quad (21)$$

Each of the constants is a blend of inner (ϕ_1) and outer (ϕ_2) constants

$$\phi = F_1\phi_1 + (1 - F_1)\phi_2 \quad (22)$$

where ϕ_1 represents original $k - \omega$ model and ϕ_2 shows Menter's modified $k - \varepsilon$ model.

Additional functions are defined as

$$\begin{aligned} F_1 &= \tanh(\arg_1^4), \quad F_2 = \tanh(\arg_2^2) \\ \arg_1 &= \min \left[\max \left(\frac{\sqrt{k}}{\beta^*\omega d}, \frac{500\nu}{d^2\omega} \right), \frac{4\rho\sigma_{\omega_2}k}{CD_{k\omega}d^2} \right], \\ \arg_2 &= \max \left(2 \frac{\sqrt{k}}{\beta^*\omega d}, \frac{500\nu}{d^2\omega} \right) \\ CD_{k\omega} &= \max \left(2\rho\sigma_{\omega_2} \frac{1}{\omega} \frac{\partial k}{\partial x_j} \frac{\partial \omega}{\partial x_j}, 10^{-20} \right) \end{aligned} \quad (23)$$

where d is a distance from each point of the flow field to the nearest wall surface and the constants are

$$\begin{aligned} \alpha_1 &= \frac{5}{9}, \alpha_2 = 0.44, \beta_1 = \frac{3}{40}, \beta_2 = 0.0828, \beta^* = 0.09, \\ \alpha_{k_1} &= 0.85, \alpha_{k_2} = 1.00, \alpha_{\omega_1} = 0.5, \alpha_{\omega_2} = 0.856 \end{aligned} \quad (24)$$

1.3.3. Partially-averaged Navier-Stokes (PANS) equations

The Navier-Stokes equations for turbulent incompressible flow are

$$\frac{\partial u_i}{\partial x_i} = 0 \quad (25)$$

$$\frac{\partial u_i}{\partial t} + u_j \frac{\partial u_i}{\partial x_j} = -\frac{1}{\rho} \frac{\partial p}{\partial x_j} + \frac{\partial}{\partial x_j} \left(\nu \frac{\partial u_i}{\partial x_j} - \tau_{ij}(u_i, u_j) \right) \quad (26)$$

where u_i and p are the velocity and pressure.

The velocity (u_i) is decomposed into resolved velocity (U_i) and unresolved velocity (u'_i) as

$$u_i = U_i + u'_i \quad (27)$$

Each velocity satisfies the continuity equation such that

$$\frac{\partial U_i}{\partial x_i} = \frac{\partial u'_i}{\partial x_i} = 0 \quad (28)$$

Applying a partial filter to Eq. (26), the partially-averaged Navier-Stokes equations can be derived without any assumptions as

$$\frac{\partial \bar{u}_i}{\partial x_i} = 0 \quad (29)$$

$$\frac{\partial \bar{u}_i}{\partial t} + \bar{u}_j \frac{\partial \bar{u}_i}{\partial x_j} = -\frac{1}{\rho} \frac{\partial \bar{p}}{\partial x_j} + \frac{\partial}{\partial x_j} \left(\nu \frac{\partial \bar{u}_i}{\partial x_j} - \tau_{ij}(u_i, u_j) \right) \quad (30)$$

where \bar{u}_i and \bar{p} represent the partially-averaged velocity and pressure, respectively. The sub-filter scale (SFS) stress tensor, τ_{ij} , representing the effects of the unresolved motion on the resolved field results from the partial-averaging of the convective term. The closure for the SFS can be obtained by using the Boussinesq approximation as follows

$$\tau_{ij} = 2\nu_u \bar{S}_{ij} - \frac{2}{3} k_u \delta_{ij} \quad (31)$$

where \bar{S}_{ij} is the resolved rate of strain tensor, which can be expressed as

$$\bar{S}_{ij} = \frac{1}{2} \left(\frac{\partial \bar{u}_i}{\partial x_j} + \frac{\partial \bar{u}_j}{\partial x_i} \right) \quad (32)$$

ν_u denotes the eddy viscosity of unresolved scale which can be obtained by using various turbulence closure models. In previous works, the eddy viscosity of unresolved scale was expressed based on the turbulent kinetic energy (k_u) and turbulent dissipation rate (ε_u) of unresolved scale as follows (Girimaji and Abdol-Hamid, 2005; Girimaji, 2006; Frendi *et al.*, 2006; Jeong and Girimaji, 2010).

$$v_u = C_\mu \frac{k_u^2}{\varepsilon_u} \quad (33)$$

f_k is the ratio of unresolved-to-total kinetic energy and can be written as

$$f_k = \frac{k_u}{k} \quad (34)$$

For closure system of the PANS equations, two transport equations for the unresolved turbulent kinetic energy and turbulent dissipation rate were derived by Girimaji (2006). The transport equation for the turbulence kinetic energy can be expressed

$$\begin{aligned} \frac{\partial k_u}{\partial t} + \bar{u}_j \frac{\partial k_u}{\partial x_j} &= f_k \left(\frac{\partial k}{\partial t} + \bar{u}_j \frac{\partial k}{\partial x_j} \right) \\ &= f_k \left(\frac{\partial k}{\partial t} + U_j \frac{\partial k}{\partial x_j} \right) + f_k \bar{u}_j \frac{\partial k}{\partial x_j} - f_k U_j \frac{\partial k}{\partial x_j} \\ &= f_k \left(\frac{\partial k}{\partial t} + U_j \frac{\partial k}{\partial x_j} \right) + (\bar{u}_j - U_j) \frac{\partial k_u}{\partial x_j} \end{aligned} \quad (35)$$

where U_j is the time-averaged velocity, which can be regarded as the same concept used in the RANS equation.

The unresolved turbulent kinetic energy equation is obtained by substituting the two-equation RANS model in Eq. (36).

$$\frac{\partial k}{\partial t} + U_j \frac{\partial k}{\partial x_j} = P - \varepsilon + \frac{\partial}{\partial x_j} \left[\left(\nu + \frac{\nu_t}{\sigma_k} \right) \frac{\partial k}{\partial x_j} \right] \quad (36)$$

$$\frac{\partial k_u}{\partial t} + \bar{u}_j \frac{\partial k_u}{\partial x_j} = f_k \left(P - \varepsilon + \frac{\partial}{\partial x_j} \left[\left(\nu + \frac{\nu_t}{\sigma_k} \right) \frac{\partial k}{\partial x_j} \right] \right) + (\bar{u}_j - U_j) \frac{\partial k_u}{\partial x_j} \quad (37)$$

The averaging-invariant form of the turbulent kinetic energy is shown in Eq. (38).

$$\begin{aligned} \frac{\partial k_u}{\partial t} + \bar{u}_j \frac{\partial k_u}{\partial x_j} &= P_u - \varepsilon_u + T_{k_u} \\ T_{k_u} &= f_k \left(\frac{\partial}{\partial x_j} \left[\left(\nu + \frac{\nu_t}{\sigma_k} \right) \frac{\partial k}{\partial x_j} \right] \right) + (\bar{u}_j - U_j) \frac{\partial k_u}{\partial x_j} \\ &= \frac{\partial}{\partial x_j} \left[\left(\nu + \frac{\nu_t}{\sigma_k} \right) \frac{\partial k}{\partial x_j} \right] \end{aligned} \quad (38)$$

Consequently, the transport equation for turbulent kinetic energy in the PANS model is written as

$$\frac{\partial k_u}{\partial t} + \bar{u}_j \frac{\partial k_u}{\partial x_j} = P_u - \varepsilon_u + \frac{\partial}{\partial x_j} \left[\left(\nu + \frac{\nu_u}{\sigma_{k_u}} \right) \frac{\partial k_u}{\partial x_j} \right] \quad (39)$$

where the P_u is the unresolved scale production term and model coefficient is defined by

$$\sigma_{k_u} = \sigma_k \frac{f_\varepsilon}{f_k} \quad (40)$$

The transport equation for the turbulent dissipation rate (ε_u) of unresolved scales can be also expressed as

$$\frac{\partial \varepsilon_u}{\partial t} + \bar{u}_j \frac{\partial \varepsilon_u}{\partial x_j} = f_\varepsilon \left(\frac{\partial \varepsilon}{\partial t} + U_j \frac{\partial \varepsilon}{\partial x_j} \right) + (\bar{u}_j - U_j) \frac{\partial \varepsilon_u}{\partial x_j} \quad (41)$$

where f_ε is the unresolved-to-total ratio of dissipation rate defined as,

$$f_\varepsilon = \frac{\varepsilon_u}{\varepsilon} \quad (42)$$

The transport equation for the turbulent dissipation is shown in Eq. (43) and the transport equation of unresolved dissipation rate in the PANS model can be expressed in Eq. (44)

$$\frac{\partial \varepsilon}{\partial t} + U_j \frac{\partial \varepsilon}{\partial x_j} = C_{\varepsilon_1} \frac{\varepsilon}{k} P - C_{\varepsilon_2}^* \frac{\varepsilon^2}{k} + \frac{\partial}{\partial x_j} \left[\left(\nu + \frac{\nu_t}{\sigma_\varepsilon} \right) \frac{\partial \varepsilon}{\partial x_j} \right] \quad (43)$$

$$\frac{\partial \varepsilon_u}{\partial t} + \bar{u}_j \frac{\partial \varepsilon_u}{\partial x_j} = C_{\varepsilon_1} \frac{\varepsilon_u}{k_u} P_u - C_{\varepsilon_2}^* \frac{\varepsilon_u^2}{k_u} + \frac{\partial}{\partial x_j} \left[\left(\nu + \frac{\nu_u}{\sigma_{\varepsilon_u}} \right) \frac{\partial \varepsilon_u}{\partial x_j} \right] \quad (44)$$

where the modified model coefficients are defined by

$$C_{\varepsilon_2}^* = C_{\varepsilon_1} + \frac{f_k}{f_\varepsilon}(C_{\varepsilon_2} - C_{\varepsilon_1}), \quad \sigma_{\varepsilon_u} = \sigma_\varepsilon \frac{f_\varepsilon}{f_k} \quad (45)$$

Later, Lakshmiapaty and Girimaji (2006) proposed the turbulence closure model based on $k - \omega$ SST. The transport equation for the turbulent frequency (ω_u) and the eddy viscosity of unresolved scale are

$$\frac{\partial k_u}{\partial t} + \bar{u}_j \frac{\partial k_u}{\partial x_j} = P_u - \beta^* k_u \omega_u + \frac{\partial}{\partial x_j} \left[(v + \sigma_{\omega_u} \nu_u) \frac{\partial k_u}{\partial x_j} \right] \quad (46)$$

$$\frac{\partial \omega_u}{\partial t} + \bar{u}_j \frac{\partial \omega_u}{\partial x_j} = \alpha \frac{\omega_u}{k_u} P_u - \beta' \omega_u^2 + \frac{\partial}{\partial x_j} \left[(v + \sigma_{\omega_u} \nu_u) \frac{\partial \omega_u}{\partial x_j} \right] \quad (47)$$

$$\nu_u = \frac{k_u}{\omega_u} \quad (48)$$

The model constants are given by

$$\sigma_{\omega_u} = \sigma_\omega \frac{f_\omega}{f_k}, \quad \beta' = \alpha \beta^* - \frac{\alpha \beta^*}{f_\omega} + \frac{\beta}{f_\omega} \quad (49)$$

where $\beta^* = 0.09$, $\alpha = 5/9$, $\beta = 0.075$, $\sigma_k = 2.0$, $\sigma_\varepsilon = 2.0$ and $\sigma_\omega = 2.0$.

1.3.4. Reynolds stress model (RSM)

Linear eddy viscosity models based on the Boussinesq approximation for the estimation of the Reynolds stresses are unacceptable for strongly anisotropic flow. Strong turbulent anisotropy is usually identified near a solid wall since the blocking effect decreases the velocity fluctuations normal to the solid surface, leading to the increment of the lateral and streamwise components of velocity. (Hunt and Graham, 1978). For the linear eddy viscosity models, C_μ is usually used as a scalar value of 0.09. However, C_μ should decrease when there are high strain rates near the wall. Therefore, the linear eddy viscosity models fail to accurately predict the anisotropy of the Reynolds stress in all flow fields.

The exact Reynolds stress transport equations can account for the directional effects of the Reynolds stress. Launder *et al.* (1975) introduced the exact equations governing the transport of Reynold stress for incompressible turbulent flow. The transport equations for the Reynolds stress can be derived by multiplying the Navier-Stokes equations for a fluctuating velocity component and time averaging the equations. If N represents the Navier-Stokes equations, the Reynolds stress transport equation can be obtained from

$$\begin{aligned} & \overline{u'_j N(u_i) + u'_i N(u_j)} \\ &= \overline{u'_j \frac{\partial u_i}{\partial t}} + \overline{u'_i \frac{\partial u_j}{\partial t}} + \overline{u'_j \frac{\partial}{\partial x_k} (u_i u_k)} + \overline{u'_i \frac{\partial}{\partial x_k} (u_j u_k)} \quad (50) \\ & \quad - \overline{u'_j \frac{\partial}{\partial x_k} \sigma_{ik}} - \overline{u'_i \frac{\partial}{\partial x_k} \sigma_{jk}} \end{aligned}$$

where time and convective derivative terms can be expressed as

$$\begin{aligned} \overline{u'_j \frac{\partial}{\partial t} (\bar{u}_i + u'_i)} + \overline{u'_i \frac{\partial}{\partial t} (\bar{u}_j + u'_j)} &= \overline{u'_j \frac{\partial}{\partial t} (\bar{u}'_i)} + \overline{u'_i \frac{\partial}{\partial t} (\bar{u}'_j)} \\ &= \frac{\partial}{\partial t} (\overline{u'_i u'_j}) \end{aligned} \quad (51)$$

$$\begin{aligned} \overline{u'_j \frac{\partial}{\partial x_k} (\bar{u}_k \bar{u}_i + u'_k \bar{u}_i + u'_i \bar{u}_k + u'_i u'_k)} \\ + \overline{u'_i \frac{\partial}{\partial x_k} (\bar{u}_k \bar{u}_j + u'_k \bar{u}_j + u'_j \bar{u}_k + u'_j u'_k)} \\ = \overline{u'_j u'_k} \frac{\partial}{\partial x_k} \bar{u}_i + \overline{u'_i u'_k} \frac{\partial}{\partial x_k} \bar{u}_j + \frac{\partial}{\partial x_k} (\overline{u_k u'_i u'_j}) \\ + \frac{\partial}{\partial x_k} (\overline{u_k u'_k u'_j}) \end{aligned} \quad (52)$$

in which the continuity equation, $\frac{\partial}{\partial x_k} (\bar{u}_k) = 0$, is used.

The stress term is written as

$$\begin{aligned} \overline{u'_j \frac{\partial}{\partial x_k} \sigma_{ik}} + \overline{u'_i \frac{\partial}{\partial x_k} \sigma_{jk}} \\ = \overline{u'_j \frac{\partial}{\partial x_k} \left[-p \delta_{ik} + \mu \left(\frac{\partial u_i}{\partial x_k} + \frac{\partial u_k}{\partial x_i} \right) \right]} \\ + \overline{u'_i \frac{\partial}{\partial x_k} \left[-p \delta_{jk} + \mu \left(\frac{\partial u_j}{\partial x_k} + \frac{\partial u_k}{\partial x_j} \right) \right]} \end{aligned} \quad (53)$$

In this equation, the pressure and viscous terms are yielded in Eq. (54) and (55), respectively.

$$\begin{aligned}
& -\overline{u'_j \frac{\partial}{\partial x_k} (p \delta_{ik})} - \overline{u'_i \frac{\partial}{\partial x_k} (p \delta_{jk})} \\
& = -\frac{\partial}{\partial x_k} (\overline{p u'_j \delta_{ik}}) + \overline{p \frac{\partial}{\partial x_k} (u'_j \delta_{ik})} - \frac{\partial}{\partial x_k} (\overline{p u'_i \delta_{jk}}) \\
& \quad + \overline{p \frac{\partial}{\partial x_k} (u'_i \delta_{jk})}
\end{aligned} \tag{54}$$

$$\begin{aligned}
& = -\frac{\partial}{\partial x_k} (\overline{p u'_j \delta_{ik}} + \overline{p u'_i \delta_{jk}}) + \overline{p \left(\frac{\partial}{\partial x_i} u'_j + \frac{\partial}{\partial x_j} u'_i \right)} \\
& \overline{\mu u'_j \frac{\partial^2}{\partial x_k \partial x_k} u'_i} + \overline{\mu u'_i \frac{\partial^2}{\partial x_k \partial x_k} u'_j} = \mu \left[\frac{\partial^2}{\partial x_k \partial x_k} (\overline{u'_i u'_j}) - 2 \frac{\partial u'_j}{\partial x_k} \frac{\partial u'_i}{\partial x_k} \right]
\end{aligned} \tag{55}$$

So, the stress term is arranged as follows

$$\begin{aligned}
& -\frac{\partial}{\partial x_k} (\overline{p u'_j \delta_{ik}} + \overline{p u'_i \delta_{jk}}) + \overline{p \left(\frac{\partial}{\partial x_i} u'_j + \frac{\partial}{\partial x_j} u'_i \right)} + \frac{\partial^2}{\partial x_k \partial x_k} (\overline{\mu u'_i u'_j}) \\
& \quad - 2\mu \frac{\partial u'_j}{\partial x_k} \frac{\partial u'_i}{\partial x_k}
\end{aligned} \tag{56}$$

Combining all the terms in Eq. (51) - (56), the transport equations for the Reynolds stress are written as

$$\frac{\partial}{\partial t} (\overline{\rho u'_i u'_j}) + \frac{\partial}{\partial x_k} (\overline{u_k u'_i u'_j}) = P_{ij} + D_{ij} + \Pi_{ij} - \varepsilon_{ij} + \Omega_{ij} \tag{57}$$

where P_{ij} is the term of Reynolds stress production, D_{ij} equals the turbulent diffusion, Π_{ij} is for the pressure-strain correlation term, ε_{ij} stands for the

dissipation and Ω_{ij} is the rotational term. D_{ij} , Π_{ij} , ε_{ij} and Ω_{ij} have to be modeled for closing the transport equations. The fidelity of the Reynolds stress model depends on the accuracy of the modeling for the pressure-strain, diffusion and dissipation terms.

The RSM calculates the individual Reynolds stresses, $\overline{\rho u'_i u'_j}$, using differential transport equations. Six transport equations for the Reynolds stress are solved together with a transport equation for the turbulent dissipation rate (ε). The RSM is quite complex and requires large computational power, unlike the linear eddy viscosity turbulence model, and is therefore not widely used in industrial fields.

1.3.5. Algebraic Reynolds stress model (ARSM)

The algebraic Reynolds stress model (ARSM) represented the earliest attempt to find an economical way of accounting for the anisotropy of Reynolds stress instead of solving the whole transport equation for the Reynolds stress. The high cost of solving the Reynolds stress transport equations is caused by the gradients of the Reynolds stress in the convective and diffusive terms. Rodi (1976) proposed the ARSM, which is assumed that the transport of the turbulent stresses is proportional to the turbulent kinetic energy, and the convective and diffusive effects are negligible. In some cases, it provided sufficiently accurate results (Naot and Rodi, 1982). However, as the ARSM is represented as a nonlinear equation for Reynolds stress, it must be calculated using iterative methods. Therefore, the high computational cost for the numerical simulations was still required.

To reduce the cost, Pope (1975) carried out the attempt for the first time to develop the explicit ARSM. The anisotropic components of Reynolds stress were calculated using coefficients constructed from the equations consisting of strain and rotational tensors. Craft (1997) proposed a new algebraic Reynolds stress model. Besides, the explicit expression of the Reynolds stress tensor ($\overline{\rho u'_i u'_j}$) that constitutes an anisotropic eddy viscosity model can be written as

$$\begin{aligned}
\rho \overline{u'_i u'_j} &= \frac{2}{3} \rho k \delta_{ij} \\
&- 2\mu_T \left[\left(S_{ij} - \frac{1}{3} S_{kk} \delta_{ij} \right) + \alpha_1 T_t (S_{ik} W_{kj} + S_{jk} W_{ki}) \right. \\
&\left. - \alpha_2 T_t \left(S_{ik} S_{kj} - \frac{1}{3} S_{kl} S_{kl} \delta_{ij} \right) \right] \quad (58)
\end{aligned}$$

The eddy viscosity is described as

$$\mu_T = \rho C_\mu \frac{k}{\varepsilon} \quad (59)$$

where the eddy viscosity is defined the same as in the two-equation RANS model.

The strain rate (S_{ij}) and vorticity (W_{ij}) tensors are defined as

$$S_{ij} = \frac{1}{2} \left(\frac{\partial u_i}{\partial x_j} + \frac{\partial u_j}{\partial x_i} \right), \quad W_{ij} = \frac{1}{2} \left(\frac{\partial u_i}{\partial x_j} - \frac{\partial u_j}{\partial x_i} \right) \quad (60)$$

The invariants of mean strain rate and vorticity tensors are expressed by $S = \sqrt{2S_{ij}S_{ij}}$ and $W = \sqrt{2W_{ij}W_{ij}}$, respectively.

In complex flow where several components of $\overline{u'_i u'_j}$ are of importance, the assumption of a scalar eddy viscosity (ν_t) appears to be invalid. Experimental data have shown that ν_t can be strongly sensitive to directions. Rahman and Siikonen (2006) introduced a new algebraic Reynold stress

model to accurately capture the anisotropy and a reasonable formulation for C_μ was devised as

$$C_\mu = \frac{1}{2(1 + T_t \sqrt{S^2 + W^2})} \quad (61)$$

where T_t is the dynamic time scale, such as k/ε . The new model coefficients (α_1, α_2) are described as follows

$$\alpha_1 = \left(1 + \beta + 2 \frac{P_k}{\varepsilon}\right)^{-1}, \quad \alpha_2 = \left(2 + \beta + 2 \frac{P_k}{\varepsilon}\right)^{-1} \quad (62)$$

where $\beta = \sqrt{C_\mu P_k / \varepsilon}$, $P_k = C_\mu \varepsilon \eta^2$ and $\eta = T_t \max(S, W)$.

The explicit ARSM leads to an industrially acceptable overall computational cost and is widely used in simulations of engineering flow.

1.3.6. Budget analysis

Lumley (1964) presented the spectral budget analysis of the energy equations in planes parallel to the wall. Some of the main results were the physical interpretation of the various terms and the energy transfer between wavenumbers. In the Kolmogorov theory, the turbulence would be locally isotropic. So, energy is transferred from the largest eddies of turbulence containing most of the kinetic energy to the smallest eddies, which are responsible for the dissipation of the turbulence kinetic energy. Lumley (1964) identified for the first time that the energy is transferred from small eddies to large eddies, so called inverse energy cascade. Domaradzki *et al.* (1994) performed a spectral analysis of the Reynolds stress transport equations using the DNS in the channel flow at $Re_\tau = 210$ and observed the inverse energy cascade.

The results of the budget analysis can yield the statistical quantification of the turbulence features and some remarkable insight into the interaction between the viscous sublayer and outer layer. Marquillie *et al.* (2011) investigated the budget analysis of the turbulent kinetic energy in the channel and noticed that a streak instability is related to the strong production peak of turbulent kinetic energy near the adverse pressure gradient. They also predicted that the production of strong coherent vortices is concerned with the breakdown of turbulent flow structures.

The resulting budget analysis of the Reynolds stress allows quantification of the mechanisms involved, hence providing information about their relative importance in a particular flow considered (Lee and Moser, 2019). The transport equations for the Reynolds stress were derived from the Navier-Stokes equations by ensemble averaging the equations and can be formulated

as

$$\frac{\bar{D}}{Dt} \overline{u'_i u'_j} = P_{ij} + D_{ij} + \Pi_{ij} - \varepsilon_{ij} + \Omega_{ij} \quad (63)$$

where the right hand side of the transport equation is identified as follows

$$P_{ij} = -\overline{u'_i u'_m} \frac{\partial U_j}{\partial x_m} - \overline{u'_j u'_m} \frac{\partial U_i}{\partial x_m} \quad (64)$$

$$D_{ij} = \frac{\partial}{\partial x_m} \left(\frac{\nu_t}{\sigma_k} \frac{\partial \overline{u'_i u'_j}}{\partial x_m} \right) = \text{div} \left(\frac{\nu_t}{\sigma_k} \nabla (\overline{u'_i u'_j}) \right) \quad (65)$$

$$\Pi_{ij} = -C_1 \frac{\varepsilon}{k} \left(\overline{u'_i u'_j} - \frac{2}{3} k \delta_{ij} \right) - C_2 \left(P_{ij} - \frac{2}{3} P \delta_{ij} \right) \quad (66)$$

$$\varepsilon_{ij} = \frac{2}{3} \varepsilon \delta_{ij} \quad (67)$$

$$\Omega_{ij} = -2\omega_k (\overline{u'_j u'_m} e_{ikm} + \overline{u'_i u'_m} e_{jkm}) \quad (68)$$

Here, the production term (P_{ij}) is mainly affected by the mean velocity gradient. It represents the transfer of the kinetic energy from the mean flow to the turbulent fluctuations. The production term is only the anisotropic part of the Reynolds stress, which does not require modeling for closure in the transport equations for the Reynolds stress. However, all other terms on the right-hand side of Eq. (63) require modeling to close the transport equation.

The diffusion term (D_{ij}) is modeled with the assumption that the rate of transport of Reynolds stress by diffusion is proportional to the gradients of Reynolds stress. It is a molecular diffusion term acting spatial redistribution

of the Reynolds stress due to the fluctuating velocity.

The pressure-strain correlation term (Π_{ij}) plays an important role in the transport equations for the Reynolds stress. It redistributes energy among diagonal terms of the Reynolds stress tensor. If the $\overline{u'^2}$ is larger than $\overline{v'^2}$ and $\overline{w'^2}$, the pressure-strain correlation term transfers energy from $\overline{u'^2}$ to $\overline{v'^2}$ and $\overline{w'^2}$. As a result, it makes them more isotropic and is responsible for the return to isotropy of decaying turbulence, where it redistributes energy to reduce the anisotropy in the Reynolds stress.

The modeling of the dissipations term (ε_{ij}) assumes that the small dissipative eddies are isotropic. It only affects the normal components of the Reynolds stress. Close to the wall, the anisotropy in ε_{ij} is large; but, it is valid for the flows at low Reynolds number (Antonia *et al.*, 1992).

The rotational term (Ω_{ij}) represents the transport of the Reynolds stress due to rotation.

1.3.7. Anisotropy invariant map

Lumley and Newman (1977) found that the state of turbulence can be characterized by the amount of anisotropy. The anisotropy of flow can be expressed as the Reynolds stress tensor ($\tau_{ij} = \overline{u'_i u'_j}$). The Reynolds stress tensor is a symmetric second-order tensor and can be decomposed into a traceless tensor, τ'_{ij} and an isotropic tensor, τ_{ij}° , as follows

$$\tau_{ij} = \tau_{ij}^\circ + \tau'_{ij} \quad (69)$$

The isotropic tensor is defined as

$$\tau_{ij}^\circ = \frac{1}{3} \tau_{kk} \delta_{ij} = \frac{1}{3} q^2 \delta_{ij} \quad (70)$$

where q^2 represents the trace of the Reynolds stress tensor and it is equal to twice the turbulent kinetic energy, $q^2 = 2k$.

The traceless tensor is written as

$$\tau'_{ij} = \tau_{ij} - \frac{1}{3} \tau_{kk} \delta_{ij} = \overline{u_i u_j} - \frac{1}{3} q^2 \delta_{ij} \quad (71)$$

where the traceless tensor (τ'_{ij}) is normalized with the trace of Reynolds stress tensor (q^2).

The anisotropy tensor (a_{ij}) is obtained as follows

$$a_{ij} = \frac{\tau'_{ij}}{q^2} = \frac{\overline{u_i u_j}}{q^2} - \frac{1}{3} \delta_{ij} \quad (72)$$

The anisotropy tensor was introduced to quantify the level of anisotropy of turbulent quantities and has zero trace in the case of isotropy. It can be expressed as a matrix form

$$A = \begin{pmatrix} a_{11} & a_{12} & a_{13} \\ a_{21} & a_{22} & a_{23} \\ a_{31} & a_{32} & a_{33} \end{pmatrix} \quad (73)$$

where λ_i are eigenvalues of anisotropy tensor (A). The symmetric feature of anisotropy tensor makes sure that all three eigenvalues are real. The eigenvalues of anisotropy tensor are determined by solving the characteristic equation as follows

$$|A - \lambda I| = 0 \quad (74)$$

By using the Cayley-Hamilton theorem, the characteristic equation of anisotropy tensor can be written as

$$\lambda^3 - I_1 \lambda^2 + I_2 \lambda - I_3 = 0 \quad (75)$$

where I_1 , I_2 and I_3 are called the first, second and third invariants of A , respectively.

The invariants are related to the tensors according to the relations

$$\begin{aligned}
 I_1 &= \lambda_1 + \lambda_2 + \lambda_3 = a_{kk} \\
 I_2 &= \lambda_1\lambda_2 + \lambda_2\lambda_3 + \lambda_1\lambda_3 = \frac{1}{2}(a_{ii})^2 - \frac{1}{2}a_{ij}a_{ji} \\
 I_3 &= \lambda_1\lambda_2\lambda_3 = \frac{1}{6}(a_{ii})^3 - \frac{1}{2}a_{ii}(a_{jk}a_{kj}) + \frac{1}{3}a_{ij}a_{jk}a_{ki}
 \end{aligned} \tag{76}$$

I_1 is zero and the I_2 and I_3 are expressed as

$$\begin{aligned}
 I_2 &= -\frac{1}{2}a_{ij}a_{ji} \\
 I_3 &= \frac{1}{3}a_{ij}a_{jk}a_{ki}
 \end{aligned} \tag{77}$$

Instead of I_2 and I_3 , Lumley and Newman (1977) proposed the second invariant (II) and third invariant (III), which can characterize the anisotropic properties of a turbulent flow and be defined as follows

$$\begin{aligned}
 II &= -2I_2 = a_{ij}a_{ji} \\
 III &= 3I_3 = a_{ij}a_{jk}a_{ki}
 \end{aligned} \tag{78}$$

To visualize the anisotropy of the turbulence, they introduced an anisotropy invariant map. Lumley (1979) presented that the anisotropy invariant map covers all realistic turbulence. The second invariant is plotted as a function of the third invariant in the anisotropy invariant map where the second invariant represents the degree of anisotropy, and the third invariant expresses the nature of anisotropy (Oyewola *et al.*, 2004).

Characteristic states of turbulence are represented by the boundaries of the anisotropy invariant map, as shown in Figure 1. Two curves extending from the origin describe the axisymmetric turbulence limit. The right curve coincides with axisymmetric expansion, where one diagonal component of the Reynolds stress tensor is larger than the other two components. This is called “prolate” like turbulence. The left curve represents an axisymmetric contraction where one component of the velocity fluctuations is smaller than the other two components. This is referred to as an “oblate” type of turbulence. The remaining boundary line on the top of the anisotropy invariant map connecting the ends of the right and left curves represent the two-component turbulence. It can be found in the vicinity of walls where the wall normal component of the Reynolds stress disappears much faster than the others (Jovanovic, 2013).

Three limiting points at the end of these curves have an important physical meaning. The origin (0,0) indicates the isotropic state of turbulence. The two intersections of the line, which represent the two-component turbulence with an axisymmetric curve, create the two points, $\left(-\frac{1}{36}, \frac{1}{6}\right)$ and $\left(\frac{2}{9}, \frac{2}{3}\right)$ at the anisotropy invariant map, which mean the one-component and isotropic two-component states, respectively. One component describes flow where the Reynolds stress exists only one direction and isotropic two components

account for the flow where the Reynolds stresses appear along two directions with equal magnitude.

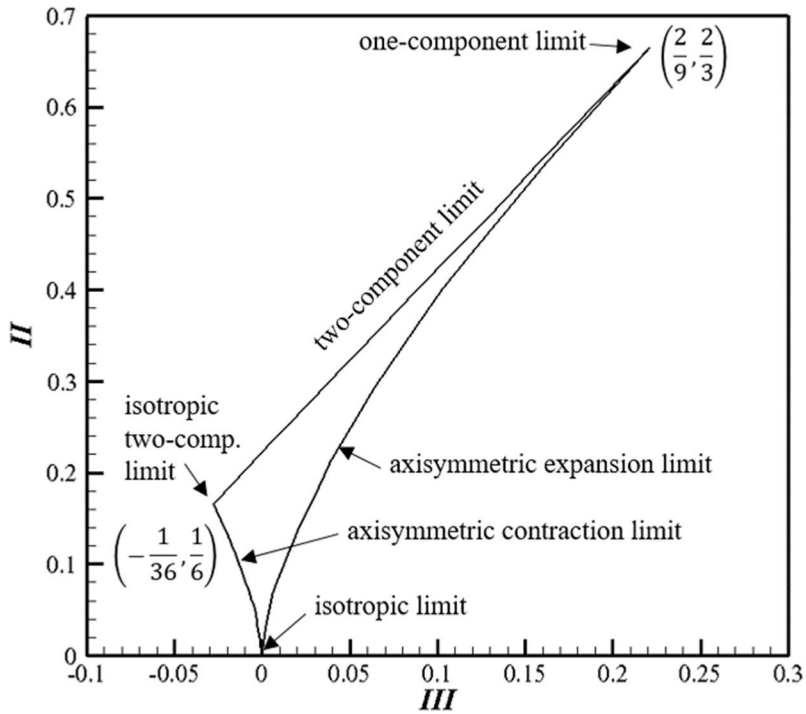


Figure 1 Anisotropy invariant map

1.4. Research objectives and outline of thesis

In the present study, modified formulations of the PANS model are suggested for accurate prediction of the turbulent secondary flow on the propeller plane of the KVLCC2. Throughout the literature review, the isotropic two-equation turbulence models failed to capture the hook shape pattern of low velocity on the propeller plane due to over-predicted eddy viscosity, which results in excessive damping of unsteady motion. In addition, the results obtained by using the anisotropic turbulence models greatly improved the prediction of force, turbulence quantities, and local flow over isotropic turbulence models. Therefore, the wide range of turbulence length scale was resolved by decreasing the f_k value in the region where the anisotropic behavior of turbulence dominates. To procure the information on the region where there is highly anisotropic of turbulence exists, the budget analysis, and the anisotropy invariant map were adopted. The level of how much f_k should be reduced in the highly anisotropic region was determined by the model constants.

The model constants were determined that can resolve the secondary flow in a square duct using the comparatively coarse grid suitable for the RANS simulations. To identify the reliability of the model constants, the modified PANS models were applied to the turbulent flow around a prolate spheroid and the KVLCC2.

The present thesis consists of four parts: computational methods, numerical validation, and application. In the chapter of computational methods, there are detailed descriptions of the modified formulation of the PANS model. Numerical validation presents the wake contours of the KVLCC2 calculated using the original PANS model and the limitation of the

original PANS model to capture the hook shape pattern of low velocity at a given grid resolution. In addition, the original PANS and the modified PANS results are shown for the turbulent flow in a straight square duct by comparing with the DNS, LES, two- and seven-equation RANS models. Model constants are determined for resolving the secondary flow on the coarse grid suitable for RANS simulation and applied to the flow around a prolate spheroid. Finally, wake contours of streamwise component and vortical structures around the KVLCC2 at drift angles of 0° and 12° are identified and analyzed using the original PANS model, modified PANS model, and two-equation RANS model.

Chapter 2. Computational methods

2.1. Modified formulation of the PANS model

In the early stage of the PANS simulation, the level of resolution can be controlled by specifying the value of f_k as a constant value throughout the computational domain. However, the PANS simulation with a lower value of constant f_k do not always provide the improved results for all flow quantities (Luo *et al.*, 2014). To find the optimal value of f_k in a given grid resolution, many PANS simulations should be carried out for various f_k values, requiring high computational costs. So, the PANS simulation with constant f_k is not reasonable and permissible for industrial applications.

Spatially varying and dynamic update of the f_k is reasonable and desirable as the requirement of resolution is variable in different regions depending on the local grid and flow condition. Girimaji and Abdol-Hamid (2005) introduced a variable f_k formulation that depends on the grid size and the turbulence length scale. It assumed that the smallest resolved length scale is determined by the local dissipation and local eddy viscosity, which is equivalent to the Kolmogorov scale. The local eddy viscosity is modeled by unresolved turbulent kinetic energy (k_u) and dissipation rate (ε_u).

In the original PANS model, k_u and either ε_u or ω_u are calculated from the transport equations based on the Boussinesq approximation. However, as the approximation assumes that eddy viscosity is an isotropic scalar quantity, it is invalid in predicting the anisotropic flow structures near the wall. As the PANS simulation is inherently based on the assumption that turbulence is locally isotropic, the original PANS model is limited to resolve

the anisotropy in a turbulent flow.

Many studies have shown that the anisotropic turbulence models significantly improved the local flow prediction, such as hook shape contours of the streamwise component of velocity, over the isotropic turbulence models. Strong anisotropy is observed inside the hook shape pattern of low velocity (Larsson *et al.*, 2010). In addition, Stern *et al.* (2014) and Bhushan *et al.* (2014) presented that the anisotropic turbulence models with a relatively finer grid were found to be sufficient for good prediction of the wake contours and provided better results than the RANS simulation with an isotropic turbulence model. Therefore, the anisotropy was an important factor for accurately resolving the hook shape contours of the streamwise component of velocity on the propeller plane.

In the present study, modified formulations of the PANS model were proposed to resolve the wider range of turbulence length scale around the hull, leading to improved predictions of the hook shape contours of the streamwise component of velocity on the propeller plane. Since the turbulence anisotropy is crucial to capture the hook shape pattern of low velocity, as mentioned in many studies, the directional effects of the Reynolds stress were considered. For the modified PANS models, the f_k value decreases in the regions where anisotropic behavior of Reynolds stress dominates. With decreasing f_k , the modeled eddy viscosity decreases, leading to the more resolved scales of coherent structure motion. The budget analysis and the anisotropy invariant map were used because they can provide information on the region where there is highly anisotropic turbulence exists. The level of how much f_k should be reduced in the highly anisotropic region was determined by the model constants.

As shown in Eq. (5), f_k is calculated from the grid scale and turbulence length scale, The turbulence length scale can be obtained from the solutions of transport equations for the unresolved turbulent kinetic energy and the dissipation rate or frequency. In the present study, the expression of the turbulent length scale (l_u) is given by

$$l_u = \frac{\sqrt{SF_{k,BA} \text{ (or } AM) \times k_u}}{\beta^* \omega_u} \quad (79)$$

where $SF_{k,BA}$ and $SF_{k,AM}$ are scaling factor for k by the budget analysis and the anisotropy invariant map, respectively.

In the modified formulation using the budget analysis, terms related to the anisotropy in the Reynolds stress transport equations were identified. The production term (P_{ij}) acts as a source of energy for the turbulent flow. As the production term increases the normal components of the Reynolds stress near the wall, it only represents the turbulence anisotropy. The pressure-strain correlation term (Π_{ij}) redistributes energy to reduce the anisotropy in the Reynolds stress. Thus, the pressure-strain correlation term represents the negative value in a strong anisotropic region. The production and pressure-strain correlation terms were directly computed using Eq. (64) and (66), respectively. The Reynolds stress tensor was obtained by using the RSM and the explicit ARSM. The RSM relies on the Reynolds stress transport equations and solves the six differential equations for the Reynolds stress components. So, a relatively high computational cost is required. However, the explicit ARSM is the economical way to account for the anisotropy of the Reynolds stresses without solving the transport equations for the Reynolds stress. For

the modified formulation of the PANS using the budget analysis, the absolute values of the production and pressure-strain correlation terms were adopted, which was proposed as follows

$$\gamma = \frac{\max[(|P_{11}| + |\Pi_{11}|), (|P_{22}| + |\Pi_{22}|), (|P_{33}| + |\Pi_{33}|)]}{(|P_{11}| + |\Pi_{11}|) + (|P_{22}| + |\Pi_{22}|) + (|P_{33}| + |\Pi_{33}|)} \quad (80)$$

$\gamma = 1/3$ represents the turbulence isotropy. On the other hand, for $\gamma = 1$, it represents the strong anisotropy of the Reynolds stress. The modified unresolved turbulent kinetic energy was obtained from the product of the $SF_{k,BA}$ and k_u . In an isotropic region, the modified unresolved turbulent kinetic energy was used as the k_u , like $SF_{k,BA} = 1$. While for the flow with highly anisotropic characteristics, $SF_{k,BA}$ was same as a model constant (A), where $SF_{k,BA}$ is a scale factor for k by the budget analysis. The $SF_{k,BA}$ between the isotropic and anisotropic regions can be obtained from a linear equation through two points $(1/3, 1)$ and $(1, A)$. The linear equation in the form of $SF_{k,BA} = by + c$ is shown in Figure 2.

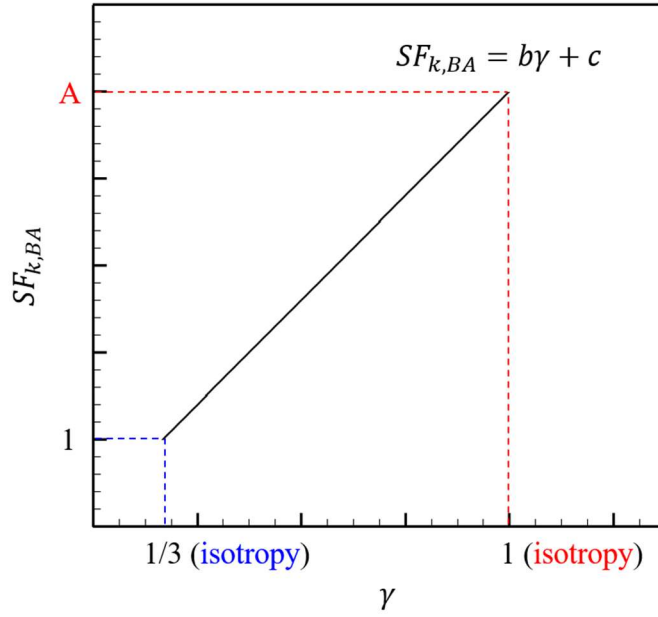


Figure 2 The formulation using the budget analysis

In the formulation using the anisotropy invariant map, the plane equation in three-dimensional space was used and could be written in an algebraic notation as $ax + by + cz + d = 0$. Then the equation of the plane through three points $(0,0,1)$, $(-\frac{1}{36}, \frac{1}{6}, A)$ and $(\frac{2}{9}, \frac{2}{3}, A)$ was expressed as $SF_{k,AM} = aII + bIII + 1$. These points represent that the origin $(0,0)$ indicates the isotropic state of turbulence and two points, $(-\frac{1}{36}, \frac{1}{6})$ and $(\frac{2}{9}, \frac{2}{3})$ are described as a turbulence anisotropic state in the anisotropy invariant map. The second invariant (II) and third invariant (III), which could characterize the anisotropic properties of a turbulent flow, were calculated using the anisotropy tensor. The plane equation is shown in Figure 3.

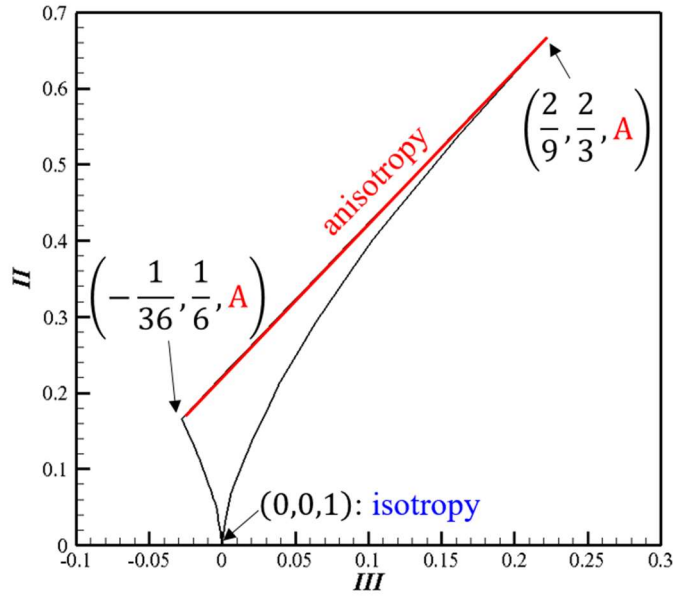


Figure 3 The formulation using the anisotropy invariant map

An appropriate f_k value should be determined for practical and accurate results at a given grid resolution. To find a reasonable constant f_k value, the PANS simulations with different constant f_k values and spatially varying f_k should be carried out. The appropriate model constant is identified by comparing the results of variable f_k with those of constant f_k values. Consequently, the PANS simulation with spatially varying f_k using the selected model constant would provide a more accurate representation of the flow structures, for the so called an explicit approach. On the other hand, the explicit approach is impractical for industrial applications as it requires more computational time. Therefore, spatially varying and dynamic update of f_k during the computational analysis is more attractive and desirable for industrial flow simulations, for the so called an implicit approach.

2.2. Simulation overview

2.2.1. Square duct

The governing equations for the partially-averaged Navier-Stokes simulation are the mass and momentum conservation equations for incompressible turbulent flow. These equations are expressed as follows

$$\frac{\partial \bar{u}_i}{\partial x_i} = 0 \quad (81)$$

$$\frac{\partial \bar{u}_i}{\partial t} + \frac{\partial}{\partial x_j} (\bar{u}_i \bar{u}_j) = -\frac{1}{\rho} \frac{\partial \bar{p}}{\partial x_i} + \nu \frac{\partial^2 \bar{u}_i}{\partial x_i \partial x_j} - \frac{\partial}{\partial x_j} (\overline{u'_i u'_j}) \quad (82)$$

The PANS simulations were conducted for the fully developed turbulent flow through a straight square duct at $Re_\tau = 300$. To verify the present PANS results, they were compared with the DNS results by Gavrilakis (1992) and Zhang *et al.* (2015). Moreover, on account of the effect of turbulence models, the LES and RANS simulations based on RSM and $k - \varepsilon$ model were performed and compared with the PANS results. The bulk velocity in the duct was set at a value of $u_b = 0.2206$ m/s, leading to the Reynolds number of $Re_b = u_b h / \nu = 4412$.

The computational domain size was $6h \times h \times h$ in the x-, y- and z- directions, respectively. The computational domain is displayed in Figure 4.

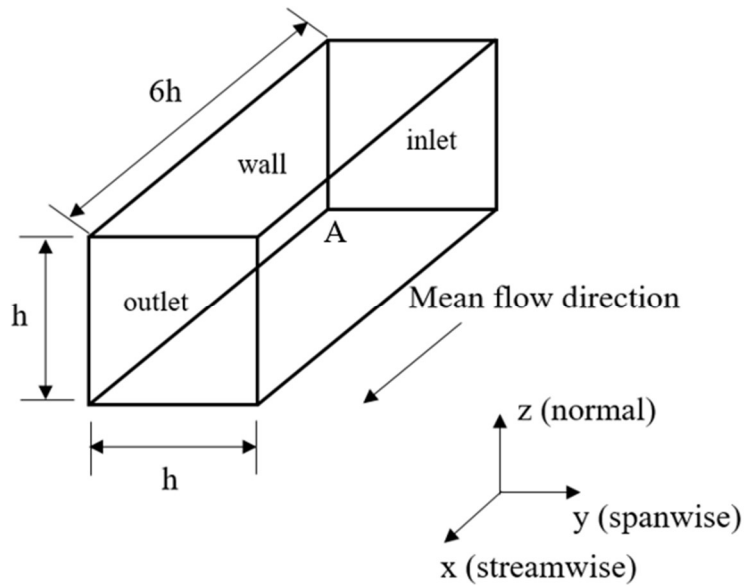


Figure 4 Computational domain for the square duct

The length of the duct was sufficiently long to ensure the fully turbulent flow and was similar to that in Zhang *et al.* (2015). The straight duct has a square cross-section of a width $h = 0.02\text{m}$ and a length of 0.12m . The Cartesian coordinates were x , y , and z , with the origin located at point A and x denotes along the streamwise direction. The direction parallel to the y -axis was defined as spanwise direction and that parallel to the z -axis as the normal direction. Concerning the boundary conditions, the no-slip condition was imposed on the walls without wall functions, and the periodic conditions were specified at the inlet and outlet. In the periodic boundary condition, the velocities of the flows were not changed, and a constant pressure gradient drove the flow adjusted to keep a constant mass flux through the square duct. The initial condition did not influence the accuracy of the final solution,

although it had an influence on the integration time required to reach a statistically stationary state (Madabhushi and Vanka, 1991). In the present simulations, the turbulent flow in the square duct was developed by superimposing the random velocity field to a mean flow velocity field. The magnitude of the random velocity was determined from trial and error tests, and the initial velocity field was generated using setFields OpenFOAM utility.

To investigate the effect of grid resolution on the results of numerical simulations, three different grid sizes were employed, consisting of 24,576, 196,608 and 1,572,864 cells for the coarse, medium and fine grids, respectively. The number of cells in the streamwise, spanwise, and normal directions was subsequently varied by approximately a factor of 2 and 1/2 in each direction, as depicted in Figure 5.

The grid resolution was measured by the $d^+ = du_\tau/\nu$ of the first point away from the wall. The variable with the superscript '+' denotes the wall length unit. In the streamwise direction, the grid spacing was uniform. To better resolve the turbulent structures near wall region, the grid distribution in the wall normal direction was non-uniform using a hyperbolic tangent function and a grid spacing of $\Delta y^+ = \Delta z^+ = 0.15$. Details of the grid system were summarized in Table 1. As seen in Table 1, the spacing of the first grid in the normal and spanwise directions keeps fixed.

Table 1 Grid properties for the square duct simulations

Comment	$L_x \times L_y \times L_z$	$N_x \times N_y \times N_z$	No. cells	Δx^+	y^+
Coarse grid	$6h \times h \times h$	$24 \times 32 \times 32$	24,576	75.00	0.15
Medium grid	$6h \times h \times h$	$48 \times 64 \times 64$	196,608	37.50	0.15
Fine grid	$6h \times h \times h$	$96 \times 128 \times 128$	1,572,864	18.75	0.15

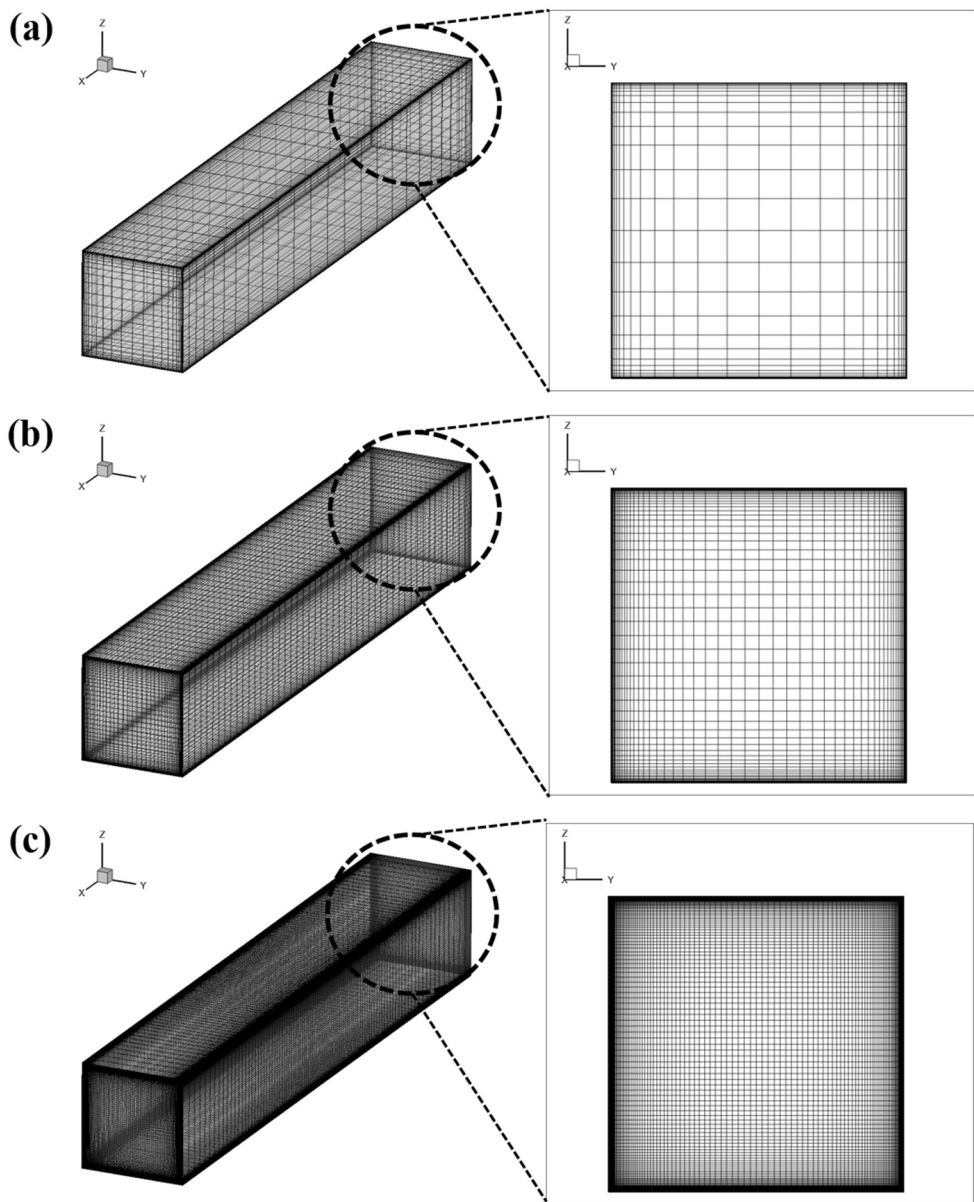


Figure 5 Computational grids: (a) coarse grid; (b) medium grid; (c) fine grid

The temporal discretization was based on the standard three level second order backward difference scheme. For spatial discretization, the ‘Gauss linear’ scheme with second order accuracy in OpenFOAM was used for divergence operators of the convective terms as well as gradient operators. For turbulence quantities, a second order total variation diminishing (TVD) limited linear scheme was used. TVD scheme has been specially formulated to achieve oscillation free solutions and was proved to be useful in CFD. The PIMPLE algorithm was applied for the pressure-velocity coupling, which is a combination of both the semi implicit method for pressure linked equations (SIMPLE) and the pressure implicit with splitting of operators (PISO) algorithm. The PIMPLE algorithm switches to the PISO algorithm when the non-orthogonal correction number is higher than one. The PISO algorithm operates with a further corrector step compared to the SIMPLE algorithm.

In the present simulations, the time step was set to between 0.002 and 0.0001 to satisfy the Courant Friedrich Levy (CFL) number condition restriction below 0.3. After the initial transient period, statistics were averaged over 600 seconds. It is crucial that the time accumulated to compute statistical quantities should be sufficiently long (Gavrilakis 1992).

2.2.2. *Prolate spheroid*

The governing equations for the PANS simulation are the mass and momentum conservation equations for incompressible turbulent flow. These equations are expressed in Eq. (81) and (82). The 6:1 prolate spheroid model used in the present study was 12m long, with a diameter of 2m. The turbulent flow was considered, where Reynolds number, $Re = U_0L/\nu$, was 4.2×10^6 , defined in terms of inlet velocity U_0 , length of the spheroid model L and kinematic viscosity ν . The calculations were performed at a 10° angle of attack. Pressure coefficient, $C_p = p/(\rho U_\infty^2/2)$, and skin friction coefficient, $C_f = \tau_w/(\rho U_\infty^2/2)$, were defined in terms of the pressure (p) and the wall shear stress (τ_w), respectively. These values at $x/L = 0.600$ and 0.772 were presented and compared with the experimental data from Chesnakas and Simpson (1997). In addition, skin friction lines and C_p contours on the whole body were presented. The previous works by Ahn et al. (1989) and McCroskey (1977) showed that the primary separation was well established, and the secondary separation inception was identified at $x/L = 0.600$. At $x/L = 0.772$, the secondary separation was well developed.

Figure 6 illustrates the computational domain and boundary conditions in a Cartesian coordinate system (x , y , and z). The x axis was coincident with the streamwise direction, and the transverse y axis was perpendicular to the symmetry plane ($y = 0$) of the spheroid. The lateral z axis was formed by a right handed system. The inlet and outlet boundaries were located $2.5L$ upstream and $4.5L$ downstream from the mid-point of the spheroid, respectively. The distance between the far-field and spheroid was $2L$. For the inlet boundary, Dirichlet conditions were applied to the velocity, turbulent

kinetic energy, and viscosity, while a Neumann condition was applied to the pressure field. For the outlet boundary, the Neumann condition was used for all variables. At the body surface, the no-slip condition is used for the velocity, whereas for all other variable, Neumann condition was employed. In addition, the wall function was used for near-wall treatment.

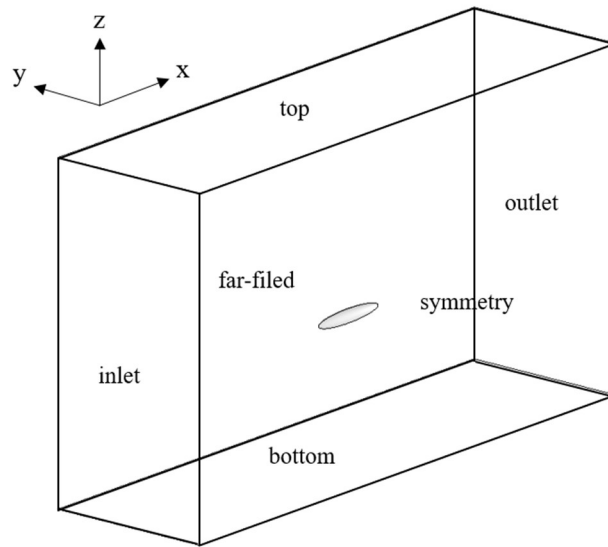


Figure 6 Computational domain for the prolate spheroid

In the streamwise and circumferential directions, the grid was generated with a uniform grid spacing of $\Delta x^+ = 200$ and $\Delta r^+ = 100$. The grid distribution in the wall normal direction was non-uniform, using a hyperbolic tangent function and a grid spacing of $\Delta y^+ = 50$. The hybrid grid generation was used, and the total number of cells was 345,156, which was a combination of structured and unstructured grids in different partitions of the domain. The surface and volume meshes around the nose of the spheroid were generated

using the unstructured grid and the other regions were generated based on the structured grid. The perspective view of the grid system and the zoom-in view near the nose are shown in Figure 7.

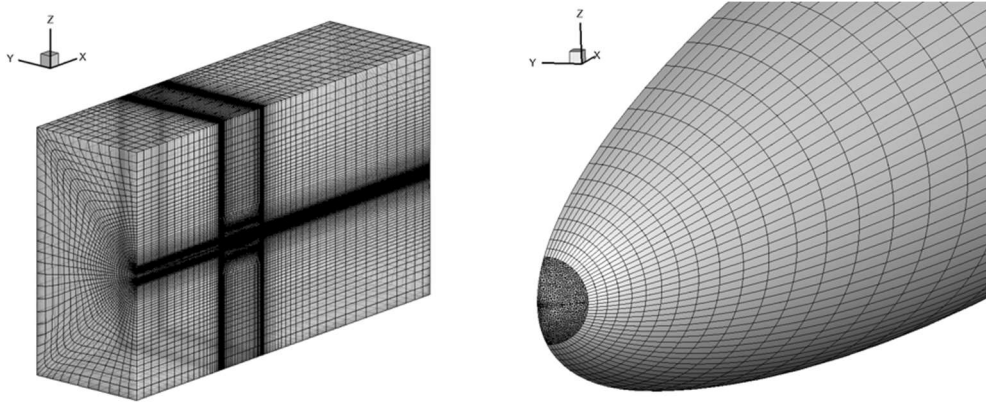


Figure 7 Computational grid. Left: perspective view; Right: zoom in near the nose

2.2.3. KVLCC2

The numerical simulations were carried out on the KVLCC2 model considering the free surface. The continuity and partially-averaged Navier-Stokes equations were used as the governing equations for incompressible two-phase flow. In addition, the volume of fluid (VOF) method was applied to model the free-surface flow. These equations are expressed as follows

$$\frac{\partial \bar{u}_i}{\partial x_i} = 0 \quad (83)$$

$$\frac{\partial \bar{u}_i}{\partial t} + \frac{\partial}{\partial x_j} (\bar{u}_i \bar{u}_j) = -\frac{1}{\rho} \frac{\partial \bar{p}}{\partial x_i} + \nu \frac{\partial^2 \bar{u}_i}{\partial x_j \partial x_j} - \frac{\partial}{\partial x_j} (\overline{u'_i u'_j}) \quad (84)$$

$$\frac{\partial \alpha}{\partial t} + \frac{\partial}{\partial x_j} (\alpha \bar{u}_i) + \frac{\partial}{\partial x_j} [\alpha(1 - \alpha) \bar{u}_r] = 0 \quad (85)$$

where \bar{u}_r is a velocity field for an extra artificial compression term, which improves the resolution of the interface between water and air. α is the volume fraction, indicating the relative proportion of fluid in each cell volume

$$\begin{aligned} \alpha = 0 & \quad \text{air} \\ \alpha = 1 & \quad \text{water} \\ 0 < \alpha < 1 & \quad \text{interface} \end{aligned} \quad (86)$$

The density (ρ) and turbulent dynamic viscosity (μ) of two-phase flow are written, respectively

$$\rho = \alpha\rho_{water} + (1 - \alpha)\rho_{air} \quad (87)$$

$$\mu = \alpha\mu_{water} + (1 - \alpha)\mu_{air} \quad (88)$$

Figure 8 illustrates the computational domain and boundary conditions for the drift angle of 0° in the Cartesian coordinate system (x, y, z) . The x axis was coincident with the keel line, and the transverse y axis was perpendicular to the symmetry plane ($y = 0$) of the ship. The lateral z axis was formed by a right handed system. The inlet and outlet boundaries were located $1.5L_{pp}$ upstream and $1.5L_{pp}$ downstream from the mid-ship, respectively. The distance between the far-field and hull was $1.5L_{pp}$.

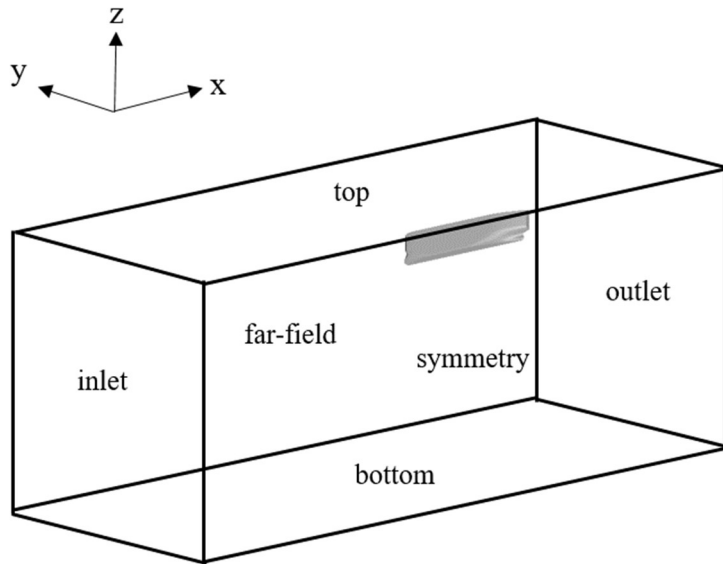


Figure 8 Computational domain for $\beta = 0^\circ$ case: geometry and boundary conditions

As the boundary conditions for velocity, the fixed value was set on the inlet boundary, while zero gradient was applied on the outlet boundary. For the pressure field, the fixed value boundary condition was employed for the outlet boundary, whereas the zero gradient boundary condition was applied to the other boundaries. Top, bottom and far-field boundaries condition was the same as the inlet boundary condition. The symmetry plane was specified with a symmetry boundary condition for the plane at $y = 0$.

The structured grids with hexahedral cells were generated for the half hull simulations, as shown in Figure 9. Before evaluating the CFD results, discretization error should be estimated for the quantification of spatial resolution error through a grid convergence study. To assess the grid convergence of resistance value for the KVLCC2, the grid convergence study was conducted based on a comparison of the results for three grids, namely fine (G1), medium (G2) and coarse (G3), which consisted of 6,035,482; 1,788,288 and 550,080 cells, respectively. The grids were progressively refined with the refinement ratio of $r_G = \sqrt{2}$.

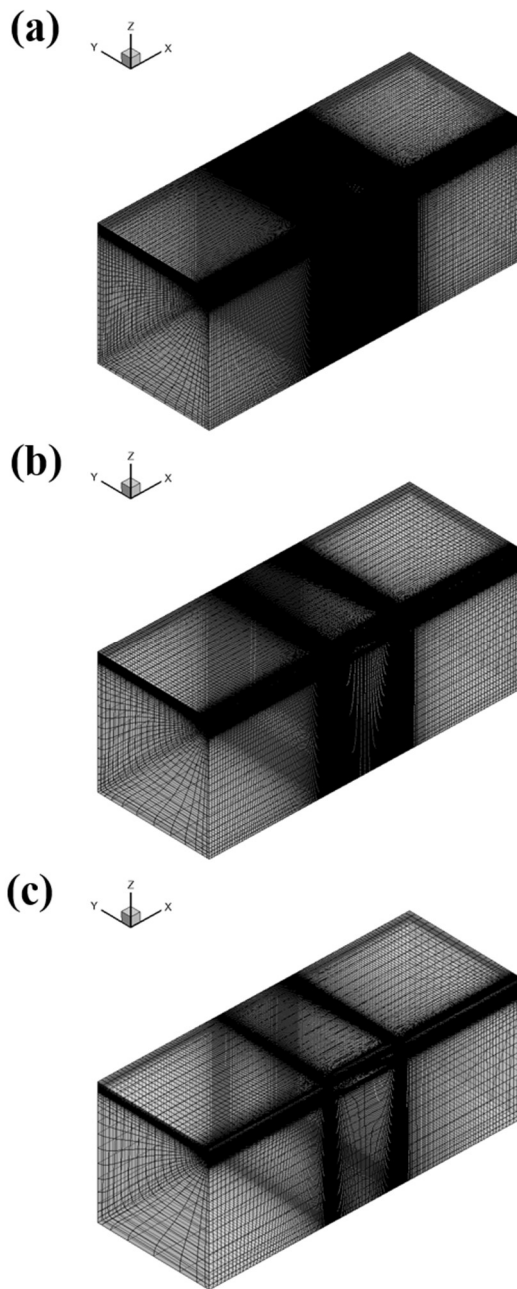


Figure 9 Computational grids for $\beta = 0^\circ$ case: (a) find grid; (b) medium grid; (c) coarse grid

The computational domain with boundary conditions for the drift angle of 12° is shown in Figure 10. The same coordinate system as the drift angle of 0° was used. The inlet, outlet, top, bottom and far-field boundary conditions were the same as those at $\beta = 0^\circ$ case. For the numerical simulation at the drift angle of 12° , the direction of inflow was adjusted without rotating the ship, and the full domain was used. The inletOutlet boundary condition in OpenFOAM was applied to the far-field boundary. The inletOutlet boundary condition was combined with the zero gradient and fixed value conditions, and the flow direction at the boundary determined which boundary condition was applied. For positive flux (out of domain) boundary, zero gradient condition was applied, and for negative flux (into of domain) boundary, the user specified fixed value was applied.

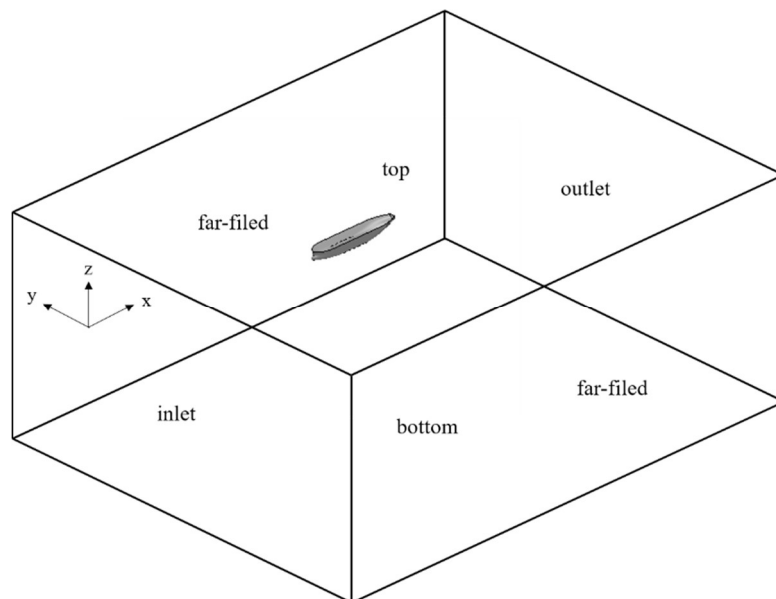


Figure 10 Computational domain for $\beta = 12^\circ$ case: geometry and boundary conditions

The structured grids with hexahedral cells were generated for the numerical simulation at the drift angle of 12° . The numbers of cells in the x-, y- and z-directions were progressively changed by the refinement ratio of $\sqrt{2}$ and $1/\sqrt{2}$, resulting in a fine grid (G1) with 9,570,208; a medium grid (G2) with 2,756,160 and coarse grid (G3) with 841,840, respectively. Figure 11 shows the grid topology of the computational domain for the drift angle of 12° .

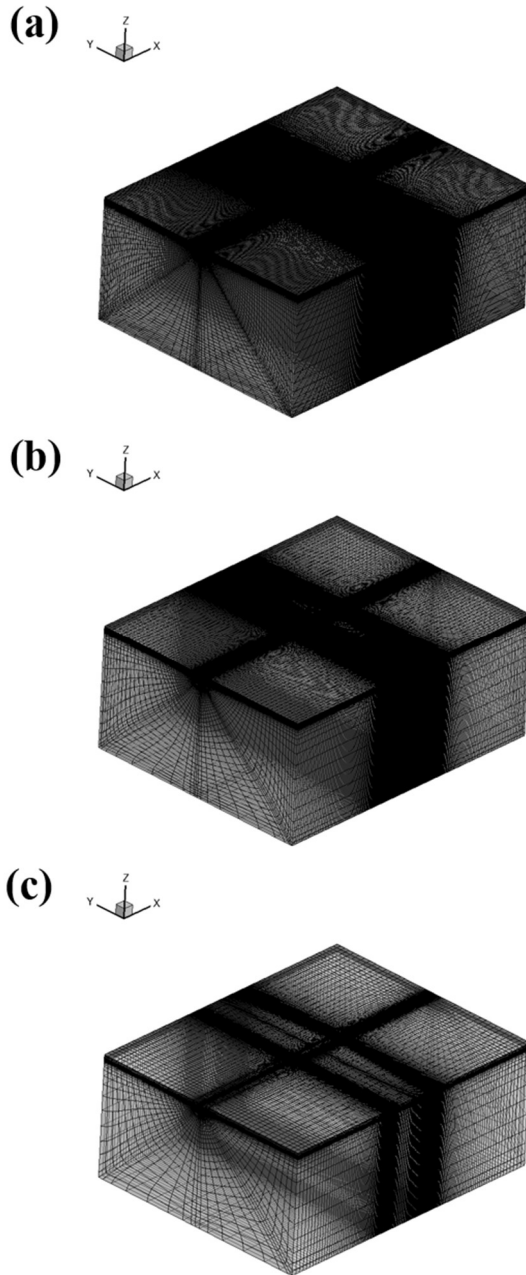


Figure 11 Computational grids for $\beta = 12^\circ$ case: (a) fine grid; (b) medium grid; (c) coarse grid

Chapter 3. Numerical validations

3.1. Preliminary tests

The PANS simulation on the medium grid for the KVLCC2 was performed at the Froude number of 0.142 and model scale Reynolds number of 4.60×10^6 . The contours of the streamwise component of mean velocity on the propeller plane ($x/L_{pp} = 0.4825$) obtained from the original PANS results and experimental measurement were shown in Figure 12 (a) and (b), respectively. The experiment data were measured by Seo *et al.* (2014) at the same Reynolds number using stereoscopic particle image velocimetry (SPIV) in a towing tank. Compared with experimental data, the hook shape vortex on the propeller plane is too weak.

To find out what caused such a discrepancy between the original PANS simulation and experimental measurement, the distribution of f_k around the hull was identified in Figure 13, which is a result of the original PANS simulation with spatially varying f_k in Eq. (5). The f_k value is high in the upstream and far from the hull and is low around the hull and in the wake region. The high value of the f_k means that the flow is modeled rather than resolved, resulting in the RANS simulation. With decreasing f_k , the modeled eddy viscosity decrease, leading to the more resolved scales of motion and improved predictions. Therefore, for an adequate description of hook shape contours of the streamwise component of velocity, the spatial resolution should be fine around the hull.

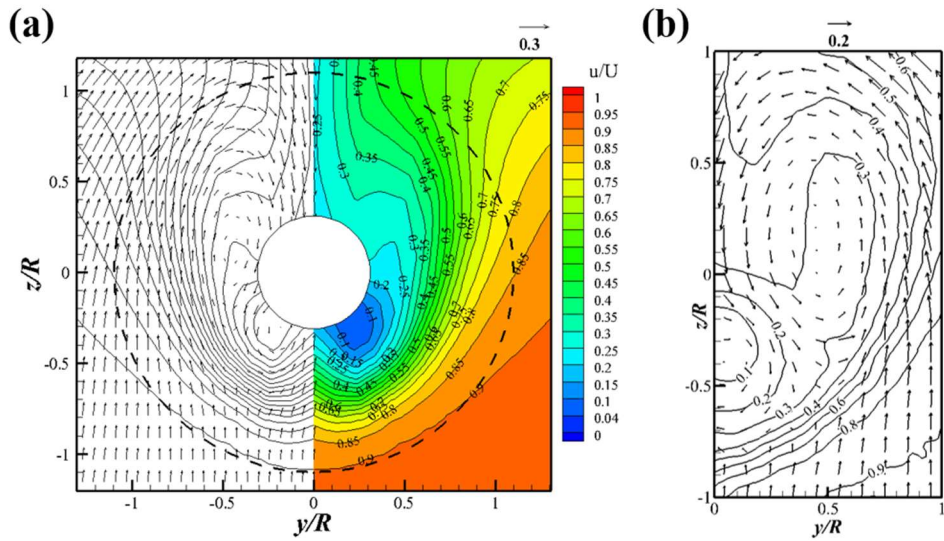


Figure 12 Comparison of the streamwise component of velocity on the propeller plane: (a) original PANS simulation, (b) experimental measurement

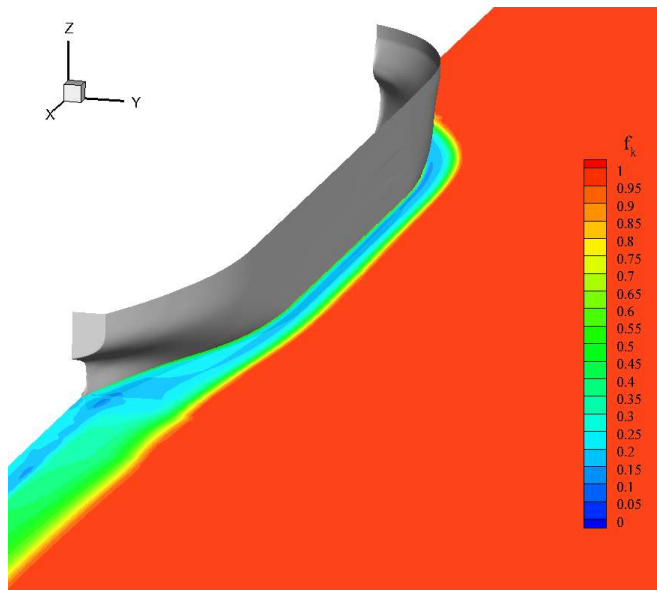


Figure 13 Instantaneous distribution of f_k from the original PANS results

The degree of spatial resolution can be controlled by specifying the value of f_k or by the grid refinement. Although a grid refinement in the PANS simulations reduces the numerical error, it is so computationally demanding. It is appropriate and practical to control the resolution using f_k for industrial applications. As well known, with decreasing f_k , the PANS model resolves the more flow structures and small scale fluctuations, resulting in an improved accuracy relative to the RANS model at a given level of physical resolution. On the other hand, the original PANS model on the given grid showed an unsatisfactory distribution of the wake contours on the propeller plane. To provide the best possible closure at any given level of physical resolution, the modified formulations of the PANS model are required.

3.2 Turbulent square duct flow

3.2.1. Introduction

The studies of the turbulent flow in channels or pipes and the turbulent boundary layer of flat plates or airfoils have been investigated over the last century. Since then, Prandtl (1926) observed four pairs of counter-rotating vortices perpendicular to the streamwise direction near the corners of the square duct, which was called the secondary flow of Prandtl's second kind. The square duct is one of the simplest geometrical configurations that present the secondary flow. The secondary flow convects momentum from the center of the square duct to its corners along the corner bisectors and transport momentum away from the corners to the center along the bounding walls. The velocity of the secondary flow is usually about 1~3% of the streamwise component of bulk velocity in magnitude. The complex flow structures and physics have been both experimentally and numerically investigated for the past few decades.

Nikuradse (1926) experimentally investigated for the first time the fully developed turbulent flow through a square duct and observed secondary flow as a counter-rotating vortex pair symmetrically located at the four corners. Brundrett and Baines (1964) provided quantitative data for the secondary flow and the Reynolds stress tensor by using a hot wire. They showed that gradients in the Reynolds stress gave rise to a source of the streamwise component of vorticity. Melling and Whitelaw (1976) measured the streamwise component of mean velocity and the corresponding normal components of the Reynolds stress in a rectangular duct using a laser Doppler anemometer (LDV). The symmetry of the secondary flow at the corners appeared to be better than one of the previous results (Gessner, 1973; Brundrett and Baines, 1964). Moreover,

the LDV has advantages in the measurement of secondary velocity and preventing probe interface.

Earlier the RANS simulations with conventional closure model based on isotropy assumptions were applied to the turbulent flow in a square duct. Sharma (1974) failed to reveal any secondary flow using turbulence models based on the isotropy of Reynolds stress. Raiesi *et al.* (2011) studied the performance of some of the RANS models for the prediction of separation and turbulence induced secondary motion. The inability of the isotropic eddy viscosity models to capture the turbulence-induced secondary flows was verified due to the excessive momentum transfer.

In addition, the RANS method provided a highly inaccurate prediction for the normal components of the Reynolds stress. Brundrett and Baines (1964) observed that the secondary flow is predominantly produced by the gradient in the normal components of the Reynolds stresses. Demuren and Rodi (1984) identified that the secondary flow is primarily produced by the gradients in the normal components of the Reynolds stresses. Gessner (1973) reported that the secondary motion is affected by the transverse gradients of the shear components of the Reynolds stress in the corner, and the secondary flow requires long distance to attain the fully developed state.

Consequently, the anisotropy of the normal components of the Reynolds stresses is important for resolving the secondary flow and the results using nonlinear turbulence models were found to give the best agreement with the experimental data and the DNS results. Many previous studies have been conducted in an effort to resolve the secondary flow using various turbulence models with anisotropic and nonlinear effects. Launder and Ying (1973) adopted the ARSM for predicting turbulent flow in a straight non-circular duct.

As the turbulence model considered the anisotropy of the Reynolds stress, the cross-stream flow could be predicted accurately. Speziale (1987) used nonlinear $k-l$ and $k-\varepsilon$ models to yield more accurate predictions for secondary flow in a square duct. For resolving the secondary flow in a square duct, the importance of anisotropy in the viscous dissipation rate was emphasized. Nisizima (1990) analyzed the fully developed turbulent flow in a square duct at $Re = 40,806$ using the anisotropic $k-\varepsilon$ model. The results showed fairly good agreement with the experimental data and other numerical results.

The progress of computing power advancement in the 1990s made it possible to perform high fidelity numerical simulations, such as the DNS (Gavrilakis. 1992; Uhlmann *et al.*, 2007; Xu., 2009; Pinelli *et al.*, 2010) and LES (Madabhushi and Vanka., 1991; Kajishima and Miyake., 1992; Xu and Pollard., 2001). Gavrilakis (1992) simulated the fully developed turbulent flow through a straight square duct at $Re_\tau = 300$. The Reynolds number, $Re_\tau = u_\tau h/\nu$, is based on the mean friction velocity (u_τ) and the duct height (h). The mean secondary flow field was in good agreement with experiments, and the Reynolds stress terms demonstrated a maximum value in the viscous sublayer. Particularly, viscous diffusion of the vorticity was noticed to play an important role. Thereafter, the simulation was adopted as a benchmark test. Uhlmann *et al.* (2007) also performed the DNS simulations of turbulent flow in a straight duct $Re_\tau = 80$. Marginal turbulence region was identified by a detailed study. Evidence was provided that buffer layer coherent structures, such as streaks and the streamwise component of vorticity, played an important role in the appearance of secondary flow in the region of marginal Reynolds numbers.

Madabhushi and Vanka (1991) used the LES to simulate the fully

developed turbulent flow in a square duct at $Re_\tau = 360$. The results were in qualitative agreement with the experimental data. The effect of the streamwise turbulence intensity on turbulence kinetic energy was significantly larger than the effect of transverse turbulence intensity on the turbulent kinetic energy. Kajishima and Miyake (1992) found the secondary flow in the fully developed turbulent flow in a straight duct using the LES. It was suggested that the consistency among the Reynolds stresses and an appropriate treatment in the near wall region were needed for the turbulence stress modeling. For these reasons, the anisotropic $k - \varepsilon$ model derived by Yoshizawa (1984) successfully simulated the secondary flow.

3.2.2. Results and discussion

Figure 14 displays the mean contours of the streamwise component of velocity and turbulence-driven secondary flow in the cross-section of the duct, predicted by the LES, original PANS (oPANS), two- and seven-equation RANS models on the medium grid. The streamwise component of mean velocity was obtained by time averaging and spatial averaging of streamwise. It was normalized by the averaged central velocity, $u_c = \bar{u}(h/2, h/2)$, where "-" denotes the time averaged value. The LES, original PANS, and seven-equation RANS models resolved the secondary flow which is distributed near the corners of the square duct. The secondary flow demonstrated four pairs of counter-rotating vortices with a symmetrical distribution. The secondary flow pushed the high velocity area toward the corners as the secondary flows transfer energy from the center to the corners. Compared with the seven-equation RANS model, the high velocity region was widely distributed near the corners predicted by the LES and oPANS model. They resolve the high strength of the secondary flow, which transfers more energy from the center to the corners. Therefore, the LES and oPANS model predicted the strong secondary vortices better than the RSM. On the other hand, in the two-equation RANS model, a different form of secondary flow was identified. The mean secondary velocity vectors rotated around the center of the duct. Thus, the two-equation RANS model failed to capture a similar secondary flow to those predicted by the LES and oPANS model. It has been known that the anisotropy and inhomogeneity of the Reynolds stress are crucial to reproduce the secondary flow near the corners of the square duct (Madabhushi and Vanka, 1991). These results showed that the turbulence models based on the isotropy of Reynolds stress offer the limited capability for resolving any secondary flow.

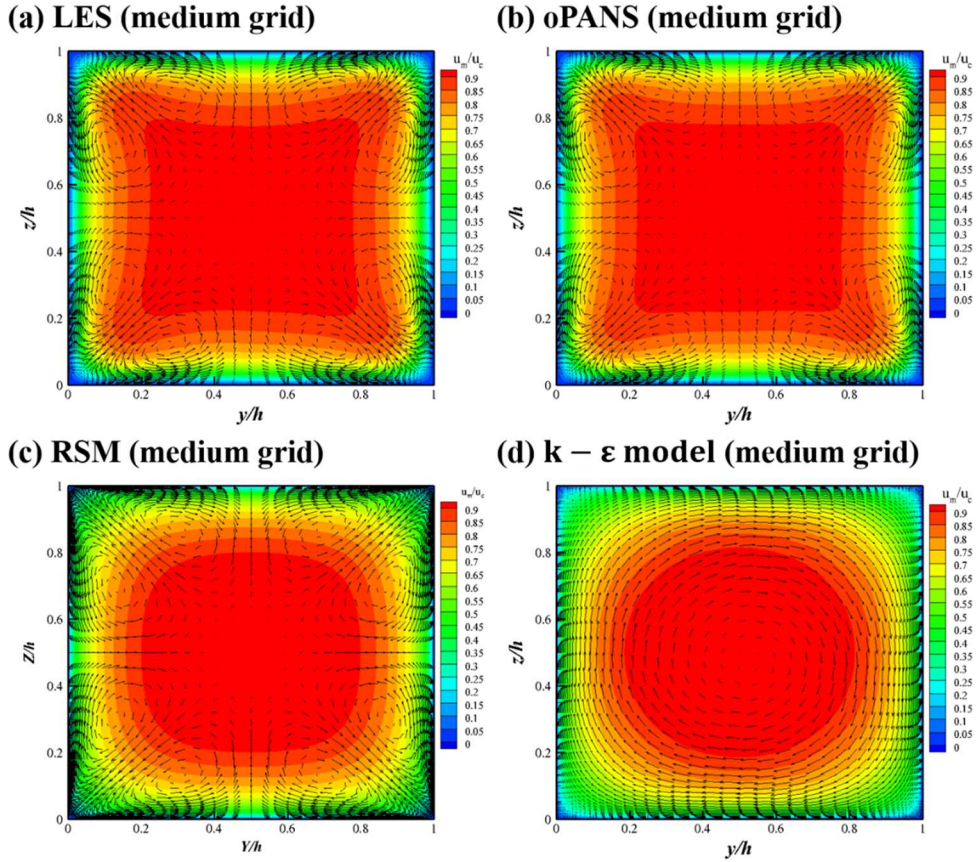
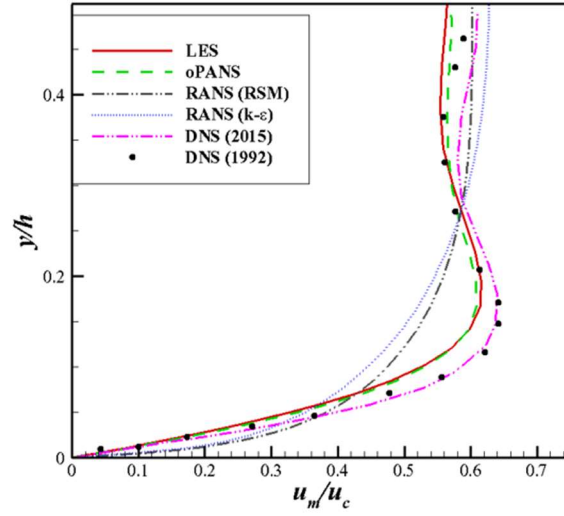


Figure 14 Contours of the streamwise component of mean velocity with the secondary flow on the medium grid

To quantitatively assess the influence of the turbulence models, Figures 15 and 16 presents a comparison of the numerical simulation results obtained by using the LES, oPANS model, RANS with RSM and $k - \epsilon$ model. Additionally, the present results were compared with the previous numerical results (Gavrillakis 1992; Zhang *et al.*, 2015) for the profiles of the streamwise and lateral components of mean velocity normalized by the averaged central velocity, u_c , respectively. As shown in Figure 15 (a), the gradient of the streamwise component of mean velocity is high near the wall, and the local

peak value is observed at $y/h = 0.13$ due to the high velocity area at the corner of the duct pushed by the secondary flow. The LES and oPANS simulations provided similar results for the profile of the streamwise component of mean velocity. Besides, they produced closer agreement with the DNS results than the RANS simulations near the wall ($z/h = 0.05$). Although the RSM resolved the secondary flow near the corners of the square duct, the secondary flow was relatively weak, resulting in the profile of the streamwise component of mean velocity similar to the $k - \varepsilon$ RANS model. The local peak velocity and secondary vortex did not appear close to the wall in the RANS simulations based on the RSM and two-equation model, which indicate that the local peak velocity was affected by the magnitude of secondary flow. Figure 15 (b) displays the distribution of the streamwise component of mean velocity along the wall bisector ($z/h = 0.05$). Unlike the region near the wall, the results did not seem to be influenced by the turbulence models because the secondary flow did not affect the profiles of the streamwise component of mean velocity at the $z/h = 0.05$. Thus, the present results obtained by using the different turbulence models were in good agreement with the DNS results.

(a) $z/h=0.05$ (medium grid)



(b) $z/h=0.5$ (medium grid)

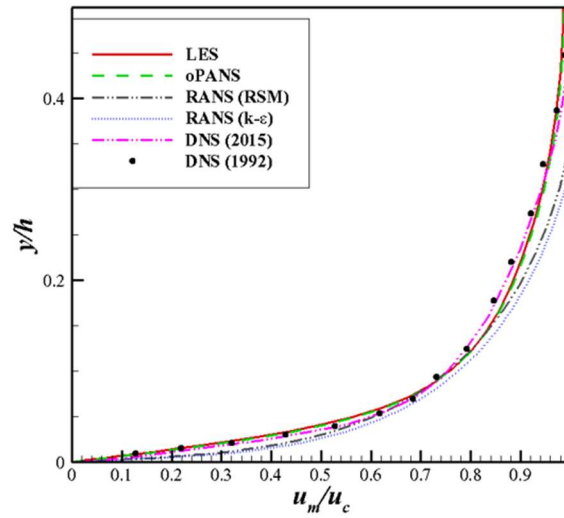


Figure 15 Profiles of the streamwise component of mean velocity on the medium grid

The profiles of the lateral component of mean velocity from the LES and oPANS model agreed well with those reported by the DNS in Figure 16 (a). They presented the positive lateral component of velocity close to the wall ($0 < y/h < 0.05$, $z/h = 0.08$) as the clockwise secondary vortex existed, as shown in Figure 16 (a) and (b). In addition, the negative lateral component of velocity was obtained at the region far from the wall ($0.05 < y/h < 0.25$, $z/h = 0.08$). Although the results from the RSM showed a similar tendency to those of the LES and oPANS model, the RSM over-predicted the w_m/u_c near the wall. The disagreement was probably due to the modeling accuracy of the various terms in the Reynolds stress transport equations, notably the pressure-strain correlation term. The effect of the pressure-strain correlation term was to decrease the anisotropy of the Reynolds stresses. In the above mentioned studies, it was important to consider the anisotropic characteristics and resolve the secondary vortex. Since the RSM depended on the accuracy of the modeling for the pressure-strain correlation term, this term should be modeled carefully. The two-equation RANS prediction showed that the mean lateral velocity was significantly small as the lateral strength of the secondary flow along the wall was significantly weak. This was because the isotropic turbulence model over-predicts the eddy viscosity, leading to the excessive damping of unsteady motion. In addition, excessive production of the turbulent kinetic energy was resolved in the two-equation RANS simulations. Therefore, the eddy viscosity models attained an unphysically small lateral velocity in the square duct. As shown in Figure 16 (a), the lateral component of velocity at $z/h = 0.4$ obtained by using the eddy viscosity model was little changed in Figure 16 (b). The profiles of the lateral component of velocity obtained from the LES and oPANS results deviated slightly from the DNS results. The RSM results were in good agreement with the LES and original

PANS results except near the wall ($y/h < 0.2$), and the RANS simulation with $k - \varepsilon$ model predicted the considerably small lateral component of velocity.

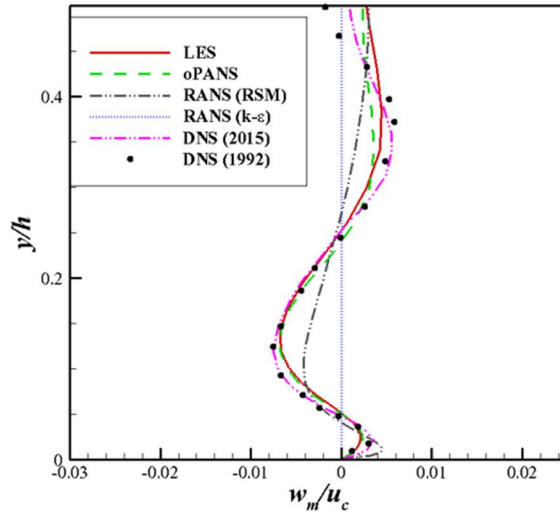
The assessment of the grid refinement in the PANS model is crucial to ensure the reliability of the results. Therefore, two different grids, such as fine and coarse grids were used, as shown in Figure 5. Figure 17 shows the profiles of the streamwise component of mean velocity predicted by the LES, oPANS model and RANS simulations with RSM and $k - \varepsilon$ model on the fine grid. As the grid was refined to fine, the velocity profile predicted by oPANS model becomes similar to those predicted by the LES. In addition, the LES and oPANS model results got closer to the DNS results shown in Figure 17 (a). In the LES, only the large scales of turbulence were directly resolved, and the smaller scales were modeled. The large scale represented the anisotropic part of the energy spectrum and contained most of the energy. The small scale (sub-grid scale) is believed to be locally isotropic in nature and relatively independent from the resolved part of the spectrum. If the grid size is small enough that the sub-grid scale did not contain much energy, the LES results could be quite accurate. Thus, the LES simulation showed more accurate results when grid resolution was sufficient to resolve most of the unsteadiness of this complex flow field. In oPANS model, the bridge parameter, f_k , decreased when the grid was refined according to the spatially varying function of f_k in Eq. (5). With decreasing f_k , the turbulent viscosity decreased, leading to the more resolved scales of turbulent structure motion, resulting in improved predictions. Therefore, the oPANS simulations presented similar trends to those predicted by the LES. Even though the results from the RSM and $k - \varepsilon$ model slightly were improved with grid refinement, it still showed a large discrepancy from the DNS results. As turbulence models

in RANS approach modeled not only small scale turbulent motions but also fluctuating scales of motion, it was less affected by the grid system. Figure 17 (b) shows that the streamwise component of mean velocity did not seem to be influenced by the turbulence models as the effect of the secondary flow was significantly weak, as shown in Figure 15 (b). As a result, Figures 15 (b) and 17 (b) presented quite similar velocity profiles regardless of the turbulence model.

With grid refinement, the LES and oPANS simulations produced closer agreement with the DNS results for the profile of lateral component of mean velocity than the RSM and $k - \epsilon$ model results, as shown in Figure 18 (a) and (b). The resolution was sufficient to resolve the large energy containing eddies in the flow.

It has been known that hybrid RANS/LES offers an improved predictive capability when the grid resolution is sufficient. However, two- and seven-equation RANS models on the fine grid provided still a significant difference for the lateral component of velocity from the DNS results, although their results were slightly changed compared to those on the medium grid. Unlike the LES and oPANS model, the RANS simulations were not affected by grid resolution, so it was difficult to guarantee higher accuracy with increasing grid density.

(a) $z/h=0.08$ (medium grid)



(b) $z/h=0.4$ (medium grid)

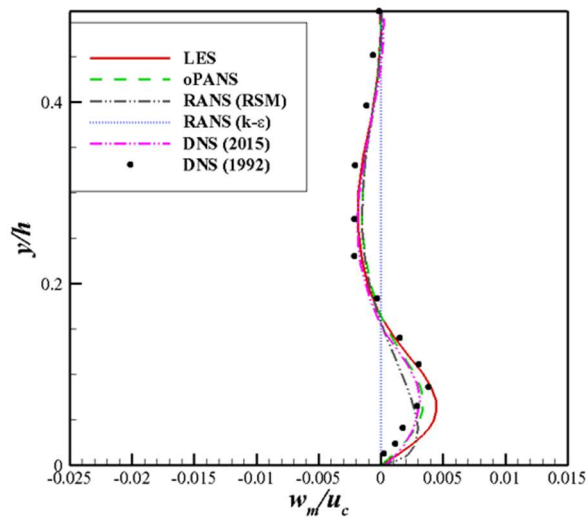
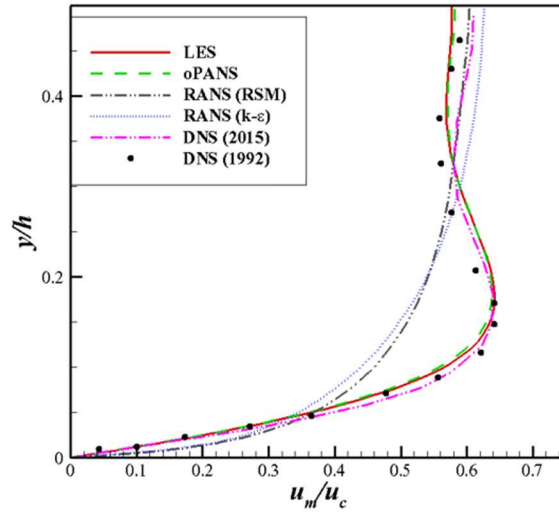


Figure 16 Profiles of the lateral component of mean velocity on the medium grid

(a) $z/h=0.05$ (fine grid)



(b) $z/h=0.5$ (fine grid)

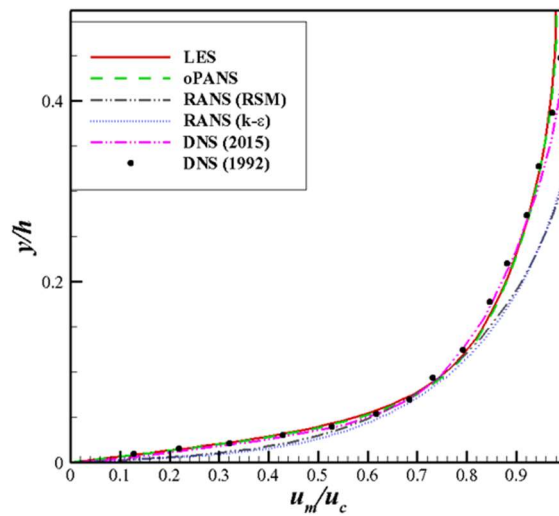
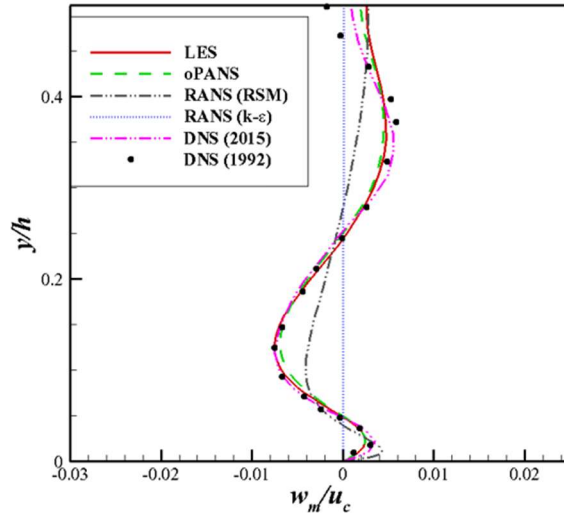


Figure 17 Profiles of the streamwise component of mean velocity on the fine grid

(a) $z/h=0.08$ (fine grid)



(b) $z/h=0.4$ (fine grid)

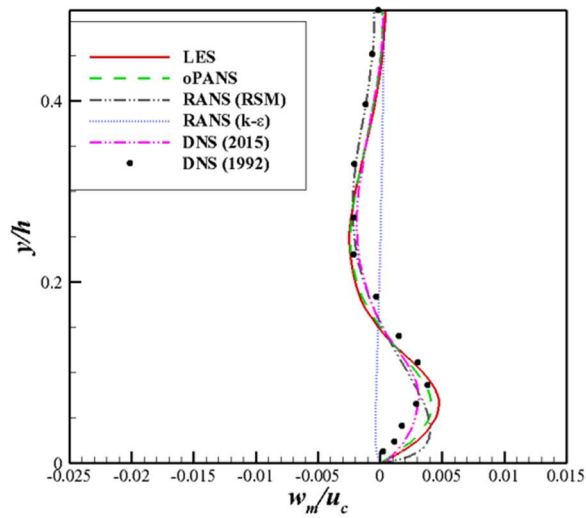


Figure 18 Profiles of the lateral component of mean velocity on the fine grid

Figure 19 shows the contours of the streamwise component of mean velocity with the secondary velocity vectors obtained from various numerical simulations on the fine grid. As previously stated, the secondary flow convected mean flow momentum from the central region to the corner region. It resulted in bulging of the contours of the streamwise component of velocity towards the corners. The LES and oPANS simulation on the fine grid led to an increasing high velocity region near the corners compared to those on the medium grid. The same distribution of the streamwise component of mean velocity was observed when the Reynolds number decreased (Zhang *et al.*, 2015). At high Reynolds number, the contours were almost flat as the center of the vortices moved from the corners to center. The RSM on the fine grid resolved the secondary flow near the corner of the square duct like the results on the medium grid. However, the simulation results were less affected by the grid system as the most turbulence length scales were modeled. So, the high velocity region in the contours of the streamwise component of the mean velocity was hardly changed even if the grid density increased. The eddy viscosity model predicted different types of secondary flow depending on the grid resolution. Unlike two-equation RANS results on the medium grid, the two-equation RANS model on the fine grid showed two large secondary flow regions symmetrically. These secondary flow shapes were similar to those found in a curved pipe.

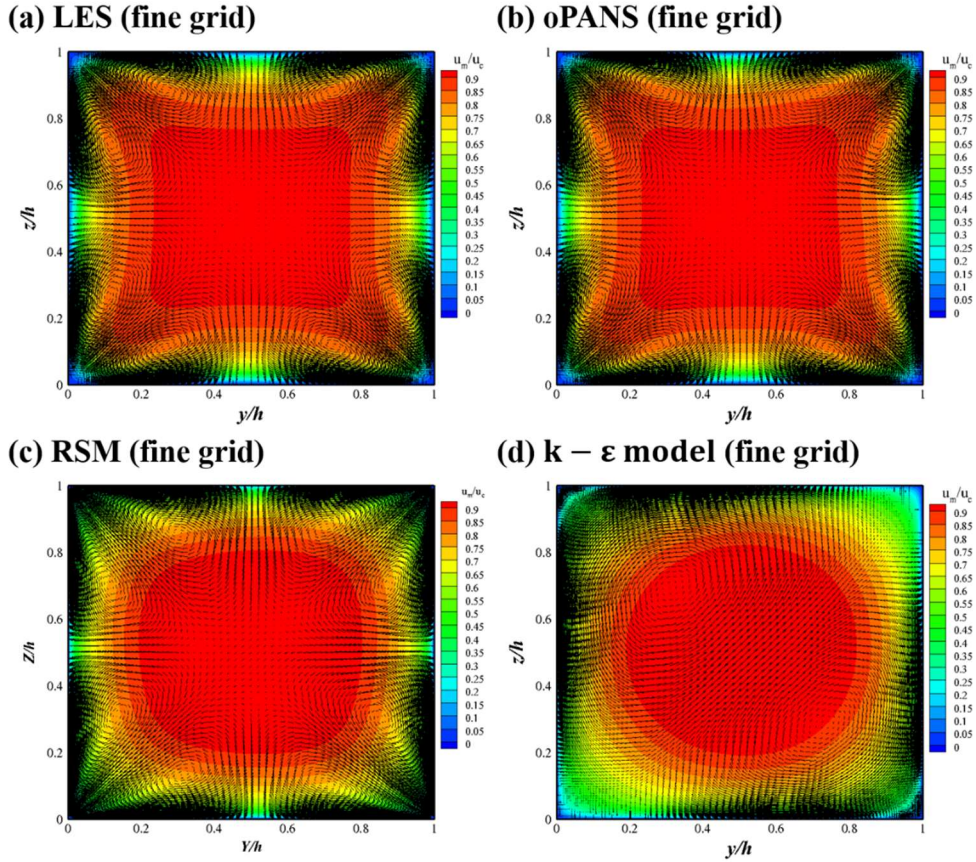


Figure 19 Contours of the streamwise component of mean velocity with the secondary flow on the fine grid

Figure 20 presents a comparison of the profile of the streamwise component of mean velocity on the coarse grid. The general observation was that the oPANS simulations produced similar trends to those predicted by the LES on the fine and medium grids. However, a large discrepancy is observed between the LES and oPANS model on the coarse grid. In Figure 20 (a), the LES and oPANS model failed to resolve the local peak values of the streamwise component of mean velocity induced by the secondary flow at $z/h = 0.13$. Although the oPANS result showed a similar velocity profile to

those of the LES, it produced closer agreement with the DNS results than the LES. The LES on the coarse grid gives the worst prediction since it failed to resolve large scale turbulent fluctuations at an insufficient grid resolution.

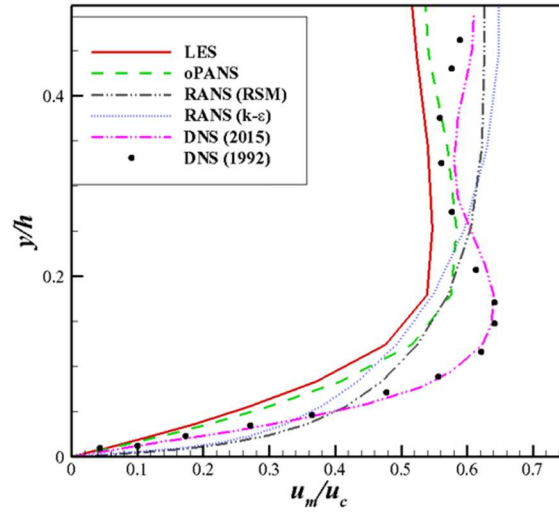
Moreover, when a larger grid cell size was used for the LES, turbulent viscosity was significantly large, resulting in over-predicted velocity distribution near the wall (Davidson and Peng, 2003). Figure 20 (b) shows no significant change in profiles of the streamwise component of mean velocity at $z/h = 0.5$, regardless of the grid density.

Figure 21 shows the comparison of the oPANS model with results of the LES, two- and seven-equation RANS models on the coarse grid for the profiles of the lateral component of mean velocity at $z/h = 0.08$ and 0.4 . The lateral component of mean velocity at $z/h = 0.08$ from the LES and oPANS simulations was under-predicted. In addition, the large deviation compared to the DNS results was observed at $y/h = 0.17$ and 0.35 , as shown in Figure 21 (a). Although the RSM simulation showed the discrepancy near the wall, it produced a similar velocity profile to the LES and oPANS results. The RSM results on the coarse grid showed little change compared to the results on medium and fine grids, which means that the RSM results were less affected by the grid density. As the RANS simulation with the $k - \varepsilon$ model led to excessive damping of unsteady motion due to over-predicted eddy viscosity, the lateral component of the mean velocity was severely under-estimated. There was almost no change in the results regardless of the grid resolution. Figure 21 (b) also presents that the LES and oPANS model provided an incorrect flow prediction compared to the DNS results. They were more sensitive to the grid resolution than the RANS models. The RANS simulations with RSM and the $k - \varepsilon$ model provided similar results to those on the medium and fine grids since the turbulence models heavily relied on the

turbulence modeling rather than grid density. Figure 21 (a) and (b) show that the RANS results were no changed despite the reduced grid resolution.

All simulations on the coarse grid predicted the inaccurate results while refining the grid converged to the correct solution in the LES and oPANS model. Even for the coarse grid, the RANS results with RSM were more similar to the DNS results than the LES results. Therefore, the oPANS results were in good agreement with the DNS results better than the LES results when a grid of insufficient resolution was used. These similar results were found in other studies (Krajnovic *et al.*, 2012; Krajnovic *et al.*, 2015; Zhang *et al.*, 2018).

(a) $z/h=0.05$ (coarse grid)



(b) $z/h=0.5$ (coarse grid)

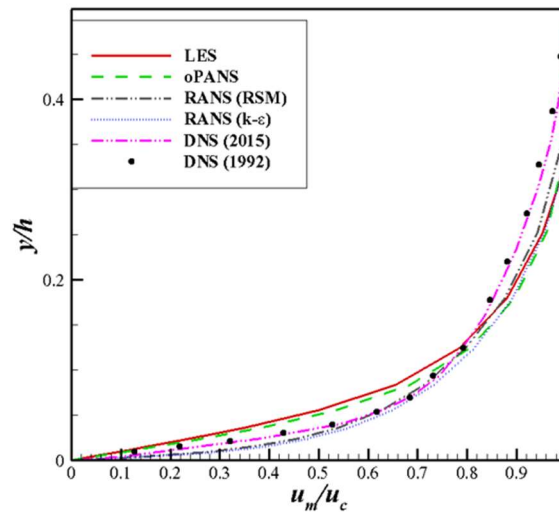
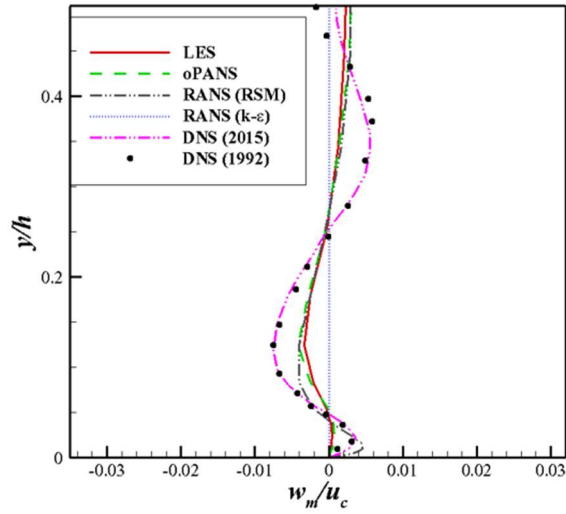


Figure 20 Profiles of the streamwise component of mean velocity on the coarse grid

(a) $z/h=0.08$ (coarse grid)



(b) $z/h=0.4$ (coarse grid)

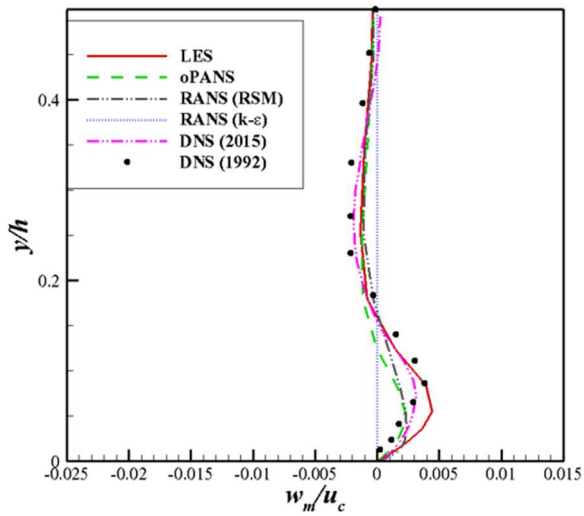


Figure 21 Profiles of the lateral component of mean velocity on the coarse grid

Figure 22 presents the contours of the streamwise component of mean velocity with secondary velocity vectors obtained by using the LES, oPANS model, RSM, and eddy viscosity model on the coarse grid. The coarse grid resolution decreased high velocity contour region near the corner compared to the medium grid. It means that the secondary velocity convected less momentum from the center to corners of the duct along the corner bisectors. In the RSM, the time-mean portion of the secondary velocity still existed, and the contours of the streamwise component of mean velocity looked similar to the RSM results on the medium grid. On the other hand, unlike the eddy viscosity model results on the fine grid, the secondary flow was shown at the centers of the square duct symmetrically with respect to the bisectors of the walls.

The LES, oPANS, and seven-equation RANS simulations could capture the secondary flow, while the two-equation RANS model failed to resolve the secondary velocity vectors. As the two-equation RANS model could not account for the directional effects of the Reynolds stress, the RANS simulation with $k - \epsilon$ model could not resolve turbulent flows with a high degree of accuracy. So, the turbulence model based on the isotropic assumption of the Reynolds stress could not capture the secondary flow in a square duct. This secondary flow was generated due to the anisotropy and inhomogeneity of the Reynolds stress (Madabhushi and Vanka, 1991). Brundrett and Baines (1964) observed that the secondary flow was predominantly produced by the gradient in the normal components of the Reynolds stress.

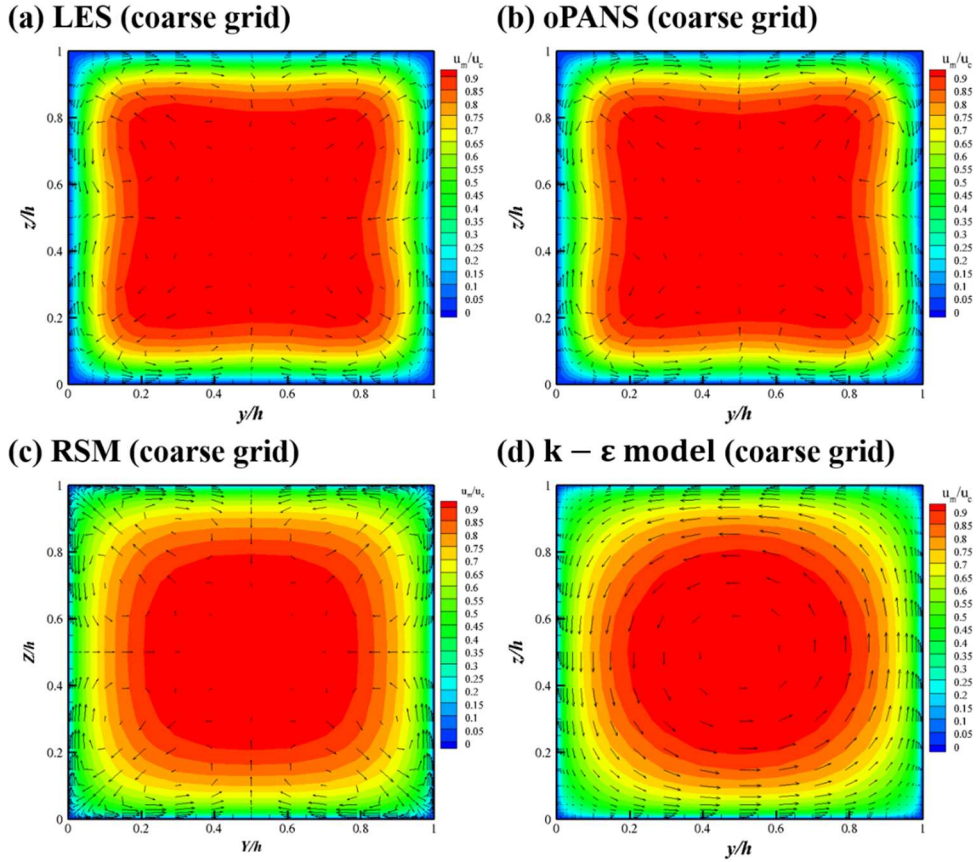


Figure 22 Contours of streamwise component of mean velocity with the secondary flow on the coarse grid

Unlike the mean velocity, the velocity fluctuations in a turbulent flow were much more complexed. Secondary motions of the second kind were mean flow induced by turbulence fluctuations (Pinelli *et al.*, 2010). In addition, the fluctuating velocity sharply increased the transport and mixing effects in a turbulent flow compared with a laminar flow. An increase in the intensity of the fluctuating velocity component was a good measure for detecting the turbulence transition in the square duct. Therefore, turbulent statistics of the fluctuating velocity field were fundamental to analyze the turbulent flow. The

root mean square (RMS) of velocity fluctuations is estimated from deviations of velocity $(q(x, y, z))$ from the mean velocity $(\bar{q}(x, y, z))$, i.e.,

$$q' = \sqrt{q'^2} = \sqrt{\frac{1}{n} \sum [q(x, y, z) - \bar{q}(x, y, z)]^2} \quad (89)$$

where $q' = u', v'$ and w' .

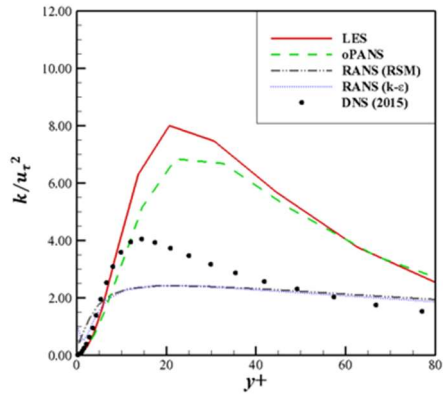
However, seven- and two-equation RANS models were not able to obtain the fluctuating velocity components since the time average of the fluctuating velocity components was zero. So, the turbulent kinetic energy was used to compare fluctuating velocity components according to the turbulence models. The turbulent kinetic energy was characterized by the measured RMS velocity fluctuations. Generally, the turbulent kinetic energy (k) is defined to be half the sum of the variances of the velocity components as follows

$$k = \frac{1}{2} (\overline{(u')^2} + \overline{(v')^2} + \overline{(w')^2}) \quad (90)$$

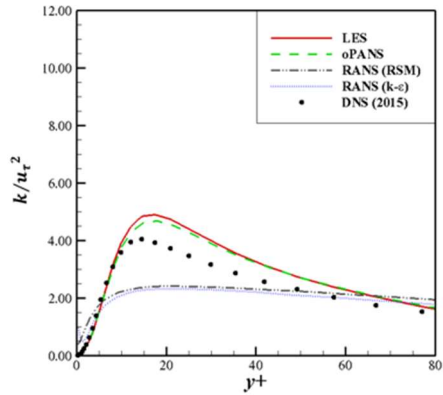
Therefore, the turbulent kinetic energy was calculated from the LES, oPANS model, two- and seven-equation RANS models depending on the grid resolution, and the results were compared with the DNS result. Figure 23 shows the distribution of non-dimensional turbulent kinetic energy (k/u_τ^2) along the wall bisector $(z/h = 0.5)$. The turbulent kinetic energy was normalized with friction velocity, $u_\tau = \sqrt{\tau/\rho}$. The LES, oPANS, and RANS

simulations with seven- and two-equation models showed a large discrepancy in the range of $y^+ = 0 - 80$. The LES and oPANS results on the coarse grid predicted lower turbulent kinetic energy than the DNS results in the viscous sublayer ($y^+ < 10$), whereas the LES and oPANS simulations predicted significantly higher turbulent kinetic energy in the rest of the region. The RANS with the RSM and $k - \varepsilon$ model significantly over-estimated the turbulent kinetic energy when compared to the DNS, LES and oPANS models. With grid refinement, the LES and oPANS results were in perfect line with the DNS results in the viscous sublayer. In the rest of the region, these results were similar to and higher than the DNS results. The RANS simulations showed a little change in the turbulent kinetic energy. The LES and oPANS model using the fine grid predicted the same turbulent kinetic energy profile as on the medium grid. For $y^+ > 10$, the results of the LES and oPANS models were consistent with grid refinement. However, the RANS results still showed similar results regardless of the grid resolution.

(a) $z/h=0.5$ (coarse grid)



(b) $z/h=0.5$ (medium grid)



(c) $z/h=0.5$ (fine grid)

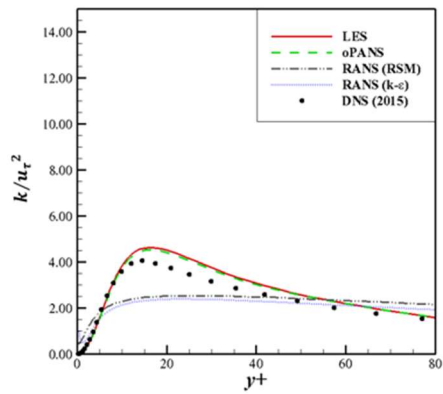


Figure 23 Profiles of the turbulence kinetic energy along the lower wall bisector

Many studies showed that flow predictions of the original PANS model were in good agreement with the experimental data and often better than the LES when the grid was relatively coarse. It has been known that the LES requires a comparatively fine grid for accurate prediction, and the LES results are varied significantly with grid refinement. Grid resolution should be fine enough to capture the critical flow of information accurately by the LES. The RANS approach assumes that most of the energy is modeled by the turbulence models, the RANS results are hardly changed depending on the grid refinement. Furthermore, the RANS simulation fails to predict complex flow structures as it suppresses most temporal and spatial fluctuations. However, the oPANS simulations resolved a wider range of scales than the RANS simulations and closely reproduced the DNS results at a higher degree of fidelity on a coarse grid.

To assess the bridging capability of the PANS model, a high resolution grid was employed, and the PANS results were compared with the LES and DNS results. However, a fine grid is not able to use for the RANS simulation in the industry due to an excessive increase in computational cost. It was necessary to make sure that the PANS model could capture the secondary flow on a comparatively coarse grid even for the RANS simulation. The size of the computational domain of the square cross-section was the same as that described in Figure 4. Grid spacing in the x-, y- and z- directions were uniform and consisted of $8 \times 8 \times 18$ cells in the three directions, respectively. The perspective view and front view of the grid system are shown in Figure 24 (a) and (b), respectively.

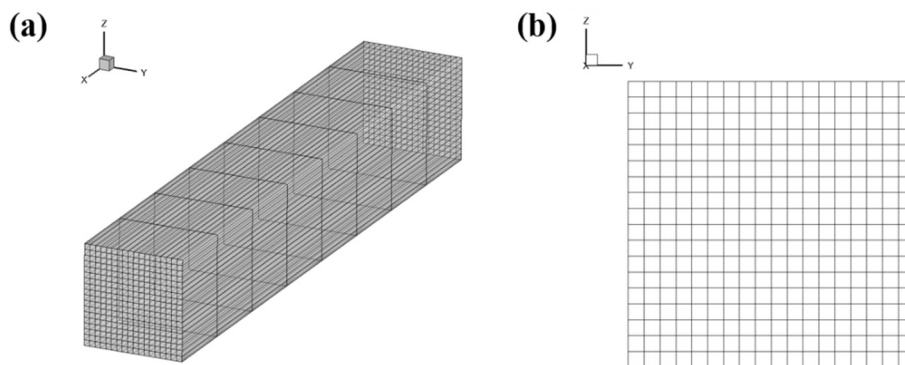


Figure 24 Computational grid for the RANS simulation: (a) Perspective view; (b) Front view

The PANS simulation on the comparatively coarse grid was conducted at the same Reynolds number, $Re_\tau = 300$, and used the same boundary conditions when comparing to the DNS, LES, and RANS models. Figure 25 shows that the oPANS simulation did not reveal any secondary flow and led it to act as the RANS model. As a result, the high velocity region was not observed near the corner of the square duct. Sharma (1974) and Raiesi *et al.* (2011) failed to capture any secondary flow using the eddy viscosity model. Therefore, the anisotropy is crucial for resolving the secondary flows. In addition, the previous studies showed the secondary flow when using turbulence models with anisotropic and nonlinear effects (Launder and Ying, 1973; Speziale, 1987; Nisizima, 1990). By reducing f_k in an anisotropic region, the eddy viscosity decreased, leading to the more resolved scales of motion and improved prediction of the secondary flow.

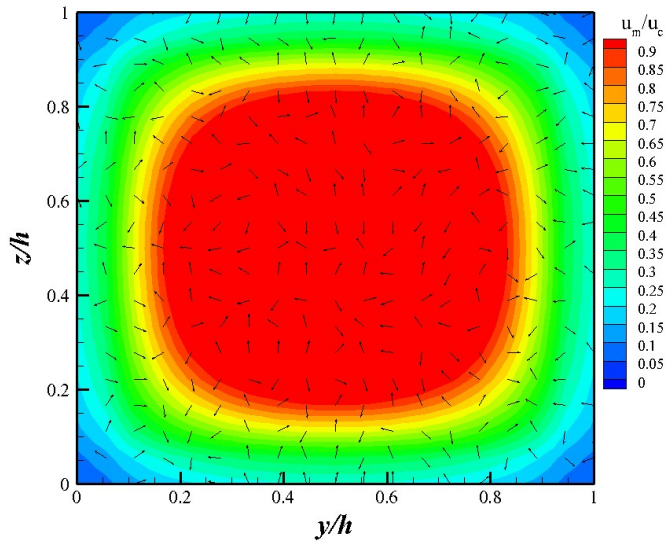


Figure 25 Contours of the streamwise component of velocity with the secondary flow from the oPANS results on the comparatively coarse grid

To apply the modified PANS (mPANS) model to the straight square duct on the comparatively coarse grid where no secondary flow appears, the model constants must be determined that can resolve the secondary flow near the corners of the square duct. From many numerical simulations, model constants 70 and 30 were determined when using the RSM and the explicit ARSM to calculate the Reynolds stress, respectively. The mPANS simulations were conducted using the budget analysis with the RSM (mPANS-BR) and the explicit ARSM (mPANS-BA) and the anisotropy invariant map with the RSM (mPANS-AR) and the explicit ARSM (mPANS-AA) at any given level of physical resolution. Figure 26 (a)-(d) shows the contours of the streamwise component of mean velocity with the secondary velocity vectors obtained by using mPANS-BR, mPANS-BA, mPANS-AR, and mPANS-AA models. These results present that the mPANS simulations captured the secondary flow

features on the comparatively coarse grid.

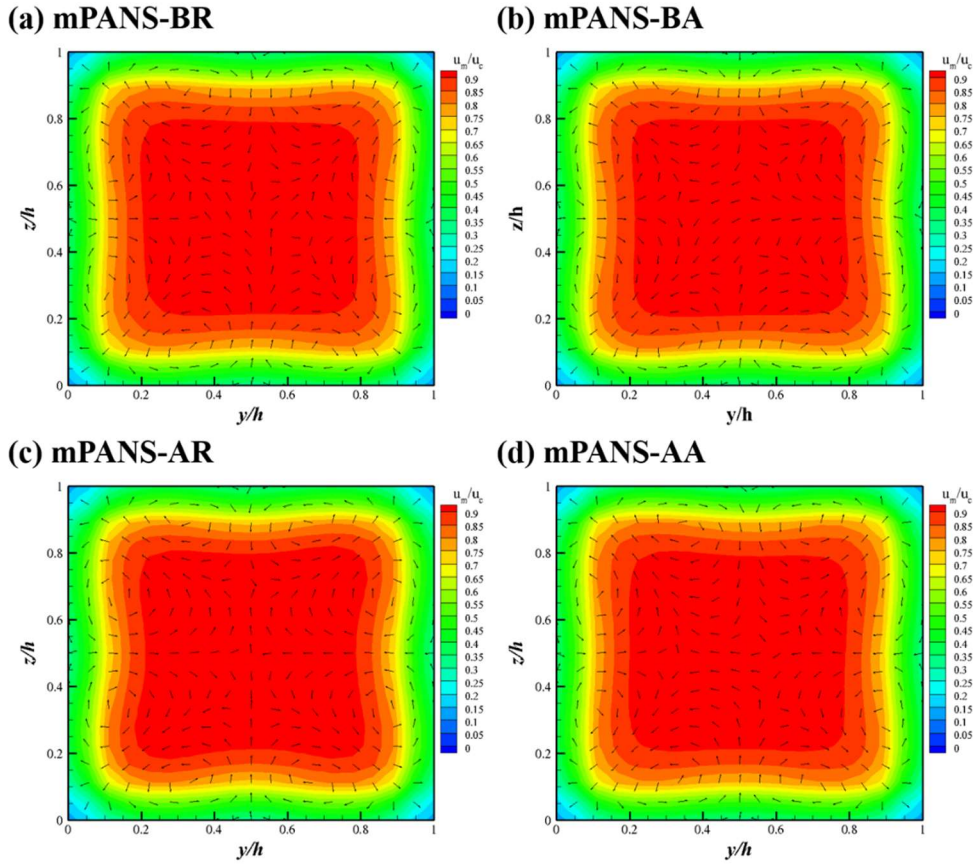


Figure 26 Contours of the streamwise component of velocity with the secondary flow from the mPANS results on the comparatively coarse grid

The selected model constants could be expressed as the linear equation for mPANS-BR, mPANS-BA, mPANS-AR and mPANS-AA models, respectively, as follows

$$\begin{aligned}
\text{mPANS-BR: } SF_{k,BA} &= 103.5\alpha - 33.5, & A &= 70 \\
\text{mPANS-BA: } SF_{k,BA} &= 43.5\alpha - 13.5, & A &= 30 \\
\text{mPANS-AR: } SF_{k,AM} &= 311\text{II} - 621\text{III} + 1, & A &= 70 \\
\text{mPANS-AA: } SF_{k,AM} &= 131\text{II} - 261\text{III} + 1, & A &= 30
\end{aligned}
\tag{91}$$

3.3. Turbulent flow around a prolate spheroid

3.3.1. *Introduction*

The 6:1 prolate spheroid has a quite simple configuration; However, the flow around the spheroid presents almost all the fundamental transition and separation phenomena of three-dimensional flow. The flow separating from the leeward side of the spheroid rolls up into a strong vortex on each side of the spheroid and reattaches on the plane of symmetry.

The turbulent flow past the prolate spheroid was studied both experimentally and computationally. Hoang *et al.* (1994) presented time histories of surface pressure measurements for the flow over a 6:1 prolate spheroid in the wind tunnel. For the prolate spheroid performing a turning maneuver, a high degree of flow unsteadiness and dynamic lift were observed as compared to steady flow cases for 10° angle of attack. For a plunge-down motion with a considerably low angle of attack, the unsteady motion has an effect on surface pressure only at some isolated regions, namely at the front and rear ends. The surface pressure and skin friction coefficients were compared with the computational results in the present study as a validation benchmark. Chesnakas and Simpson (1997) investigated the separating flow field for an inclined 6:1 prolate spheroid using fiber-optic laser Doppler velocimetry. The measurements revealed the separation and reattachment points on the model surface. Besides, the turbulent kinetic energy, wall pressure, and helicity were shown according to the inclined angle. Wetzel and Simpson (1998) studied the crossflow separation of a 6:1 prolate spheroid and measured unsteady and steady lags using hot film sensors. The lags in the development of the flow field could lead to the different flow configuration for an unsteady case as compared with the steady case at the same angle of

attack.

Tsai and Whitney (1999) performed numerical simulations of high Reynolds flow over a 6:1 spheroid at high incidence using the $k - \epsilon$ RANS model. The numerical results showed a quite good comparison of the pressure and skin friction with the LDV data. Furthermore, primary and secondary flow separation and reattachment lines also were resolved. However, the turbulence model failed to account for the tripped boundary layer. Rhee and Hino (2000) investigated laminar and turbulent separated flows around a 6:1 prolate spheroid using the Spalart-Allmaras one equation turbulence model. The comparison with the experimental data showed good agreement, and it was confirmed that the S-A model predicted the three-dimensional turbulent separated flows around the spheroid. It is suggested that more refined turbulence modeling is required to resolve the accurate three-dimensional separated vortical flow. Scott and Duque (2005) presented the DES results of turbulent flow around a 6:1 prolate spheroid at 20° angle of attack. The results were not improved when compared to those of other turbulence models for both surface pressure and skin friction. On the other hand, the DES had a positive effect on predicting the velocity profiles farther away from the surface. Xiao *et al.* (2006) used the hybrid RANS/LES method to predict high Reynolds flow fields around a prolate spheroid with a high angle of attack. The hybrid RANS/LES method presented more reasonable results than the RANS method. They suggested that more advanced turbulence models be used to improve accuracy. Karlsson and Fureby (2009) performed the RANS, DES, and LES simulations over the flow around a 6:1 prolate spheroid at 20° angle of attack. The DES predictions agreed well with the experimental data with respect to vortex locations, velocity profiles, and friction velocity profiles. Although the LES predictions using the sub-grid scale model presented a large

scatter in the results, the one equation eddy viscosity model showed good agreement with the experimental data.

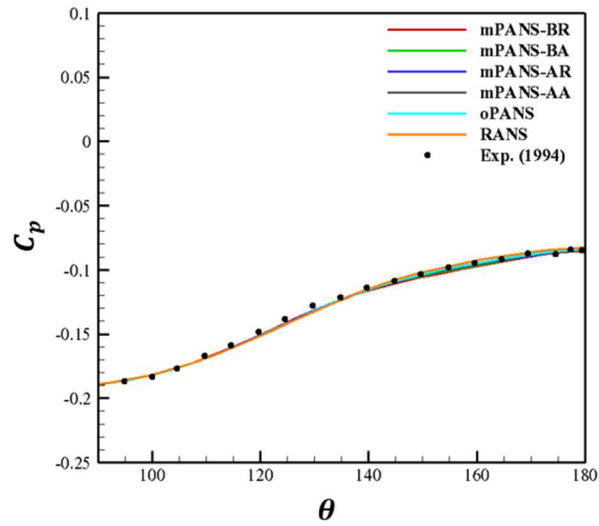
3.3.2. *Results and discussion*

Figure 27 shows the contours of the streamwise component of velocity with the secondary flow on cross-plane at $x/L = 0.9$ obtained by using the RANS, oPANS, and mPANS models. The oPANS model produced slightly stronger separation in the velocity contours than those predicted by the RANS model. However, the flow separation was more clearly identified in the mPANS results than that in oPANS results. Karlsson and Fureby (2009) presented that the high fidelity turbulence model captured the essential flow features accurately. Therefore, the mPANS models well predicted the three-dimensional turbulent separated flow behind the prolate spheroid compared with the oPANS model at a given grid resolution.

The pressure coefficient at $x/L = 0.600$ and 0.772 was compared with the experimental data (Hoang et al., 1994) and shown in Figure 28. All numerical results at $x/L = 0.600$ were agreed well according to the circumferential locations from $\theta = 90^\circ$ to 180° . However, at $x/L = 0.772$, the mPANS models could only capture the separation location ($\theta = 145^\circ$) compared with the other turbulence models.

Figure 29 presents the skin friction coefficient at $x/L = 0.600$ and 0.772 and the comparison with the experimental data. The minima in skin friction did not occur exactly at the separation location, but rather occur some distance downstream. The oPANS and mPANS results at $x/L = 0.600$ were qualitatively more accurate than the RANS results, despite the quantitative difference in the skin friction coefficient. The oPANS and mPANS models accurately detected the location ($\theta = 135^\circ$) of local minimum skin friction coefficient at $x/L = 0.772$. In addition, the mPANS models were more quantitatively consistent with experimental data than the oPANS results.

(a) $x/L=0.6$



(b) $x/L=0.772$

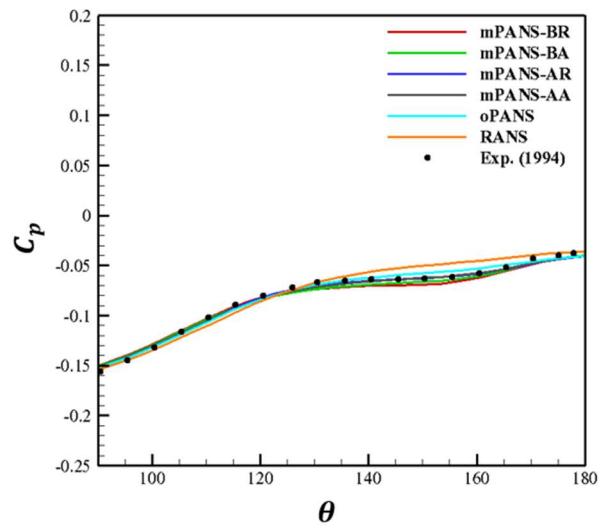
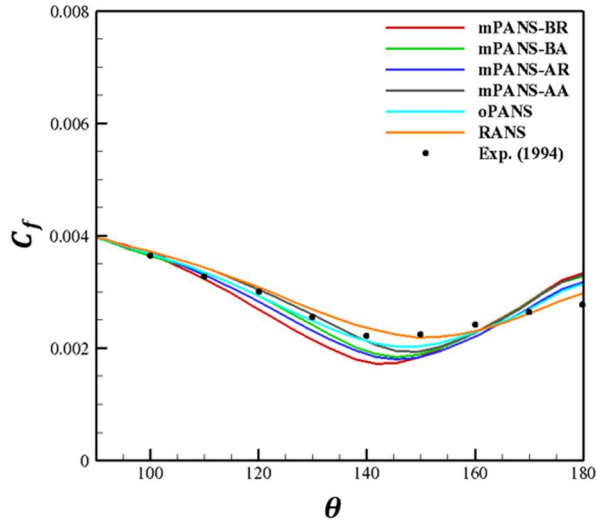


Figure 28 Comparison of pressure coefficient on the prolate spheroid

(a) $x/L=0.6$



(b) $x/L=0.772$

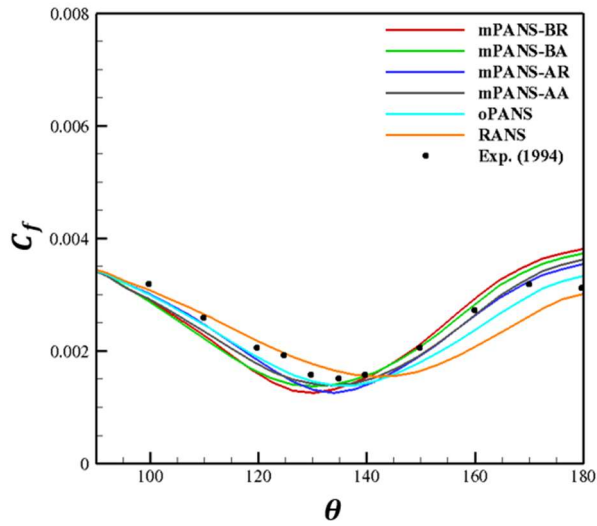


Figure 29 Comparison of skin friction coefficient on the prolate spheroid

Chapter 4. Applications

4.1. Test model

The very large crude oil carrier (VLCC) designed by the Korean Research Institute of Ships and Ocean engineering (KRISO) has been used as a representative of the benchmark model since 1997 and extensively investigated both experimentally and numerically. Although two KVLCC hull forms were provided in Kim *et al.* (2001), which were named the KVLCC and KVLCC2, comprehensive sets of experimental data for the KVLCC2 are available by both towing tank measurements (Kim *et al.*, 2001; Kume *et al.*, 2006) and wind tunnel experiments (Lee *et al.*, 2003).

Kim *et al.* (2001) measured global force, wave pattern, and wake distribution around the KVLCC2 to provide benchmark databases for CFD validation. The 1:58 scaled ship model was used, and numerical simulations were performed for straight ahead condition at $Re = 4.6 \times 10^6$. Kume *et al.* (2006) offered the contours of the streamwise component of velocity on the propeller plane and pressure distribution on the hull surface as well as a global force for the KVLCC2M at static drift angles of 0° , 6° and 12° , respectively. Lee *et al.* (2003) carried out the flow field measurements around the KVLCC in a wind tunnel using a 1:116 scale double body model for a straight ahead condition at $Re = 4.6 \times 10^6$.

There are also a number of computational studies (Kim *et al.*, 2003; Larsson *et al.*, 2003; Xing *et al.*, 2012) on the KVLCC2 using different CFD simulations. In addition, the KVLCC2 was selected as one of the benchmark cases in the ship hydrodynamics workshops in Gothenburg in 2000 (Larsson

et al., 2003) and 2010 (Larsson *et al.*, 2010; Larsson *et al.*, 2013) and in Tokyo in 2005 (Hino, 2005) as well as in the SIMMAN 2008 workshop (Stern *et al.*, 2011). Most of the numerical simulations for the KVLCC2 were on a 1:58 scaled model at $Re = 4.6 \times 10^6$. The KVLCC2 hull form with the main particulars is shown in Figure 30, and its main particulars at full and model scale are listed in Table 2.

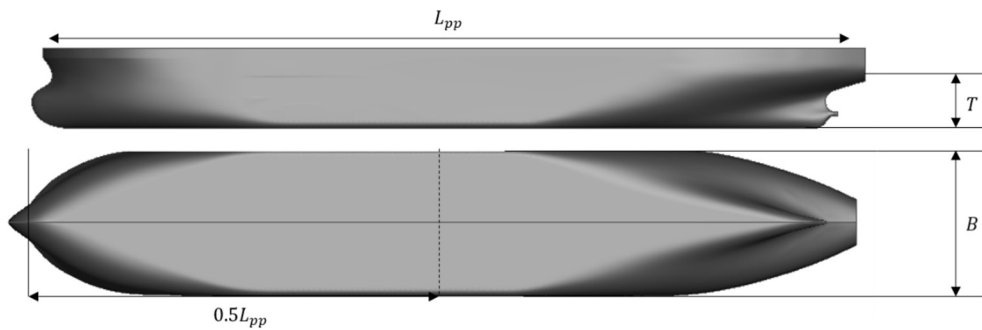


Figure 30 The KVLCC2 hull form with the main particulars

Table 2 Main particulars of the KVLCC2

Description	Symbol	Unit	Full scale	Model scale
Length between perpendiculars	L_{pp}	m	320.0	5.517
Breadth	B	m	58.0	1.000
Draft	T	m	20.8	0.359
Displacement volume	Δ	m^3	312,622	1.602
Wetted surface area	S	m^2	27,194	8.084
Center of buoyancy forward of mid-ship	LCB	$\%L_{pp}$	3.480	
Block coefficient	C_B	-	0.810	
Mid-ship coefficient	C_M	-	0.998	
Scale ratio	λ	-	58.000	

Measurement results of streamwise component of mean velocity on the propeller plane ($x/L_{pp} = 0.4825$) were obtained by using five hole pitot tubes (Kim *et al.*, 2001), hot wire anemometers (Lee *et al.*, 2003), stereoscopic particle image velocimetry (Seo., 2014), two-dimensional particle image velocimetry (Seo *et al.*, 2016) and one-dimensional pitot static tube (Seo *et al.*, 2013). They are presented in Figure 31.

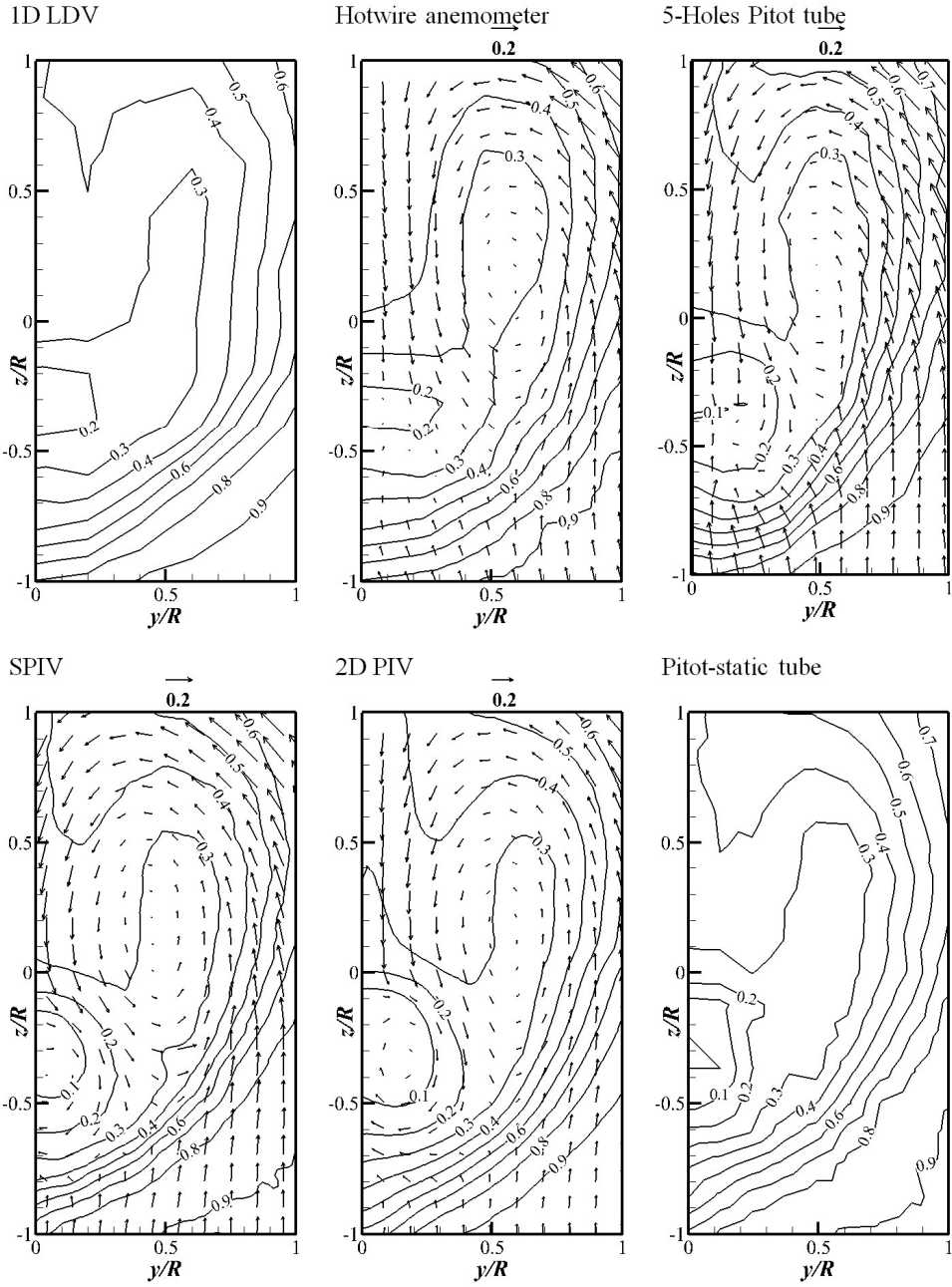


Figure 31 Measured mean velocity fields on the propeller plane of the KVLCC2

4.2. Results and discussion for the case of $\beta = 0^\circ$

The experimental data were used for validation of the present numerical simulations, which was performed at Froude number of 0.142 and model scale Reynolds number of 4.60×10^6 . The Froude number, $Fr = U_\infty/\sqrt{gL_{pp}}$, and Reynolds number, $Re = U_\infty L_{pp}/\nu$, were based on the inlet velocity, U_∞ and the length between perpendiculars, L_{pp} . All numerical simulations were performed under the same experimental conditions.

To evaluate the amount of discretization error based on the grid convergence of the solution, the grid convergence index (GCI) developed by Roache (1998) was used. As the ship resistance was the main parameter for designing ships and evaluating the performance of ships, the total resistance coefficient, C_T , was employed when the ship was in even keel condition. The total resistance coefficient was calculated as $C_T = R/(0.5\rho U_\infty^2 S)$, where S is a wetted surface area of the hull and U_∞ is free stream velocity. The refinement ratio (r_G) was determined by the total number of grid from the medium grid to the fine grid. The refinement ratio ($r_G = h_2/h_1$) was determined from G_2 to G_1 , where h_i is defined as a representative grid size. The convergence ratio ($R_G = \varepsilon_{21}/\varepsilon_{32}$) between the grid systems was acquired using $\varepsilon_{21} = \varphi_2 - \varphi_1$ and $\varepsilon_{32} = \varphi_3 - \varphi_2$, where φ_i denotes the total resistance coefficient on the G_i grid ($i = 1, 2$ and 3). If the ratio was between 0 and 1, the simulation value coincided with a monotonic convergence for grid resolution. Moreover, the ratio below 0 or over 1 represents the oscillatory convergence and divergence for grid refinement, respectively. Since R_G is between 0 or 1, the resistance coefficient corresponded to a monotonic convergence for grid resolution. The apparent accuracy order, P_G , was calculated through $P_G = (1/\ln(r_G))|\ln|\varepsilon_{32}/\varepsilon_{21}||$.

The approximate relative error (e^{21}) is expressed in a dimensioned form of $e^{21} = |\varphi_2 - \varphi_1|/\varphi_1$. As G_2 grid resolution was mainly used in the present study, the medium GCI index was calculated as $GCI_{G_2}^{21} = r_G^{P_G} GCI_{G_2}^{21} = r_G^{P_G} \times F_S e^{21} / (r_G^{P_G} - 1)$, where F_S was a safety factor. Roache (1994) recommended that values of the safety factor are $F_S = 3.0$ when two grids were considered and $F_S = 1.25$ for three or more grids. The medium GCI index for the RANS simulations with the $k - \omega$ SST model, RSM, and the oPANS model was 0.50%, 0.22% and 1.82%, respectively, which were well within the acceptable limits ($\ll 5\%$). They are summarized in Table. 3.

Table 3 Calculation of grid convergence index

		Total resistance coefficient (C_T)		
		k - ω SST model	RSM	oPANS model
Variation	Coarse to medium	1.1%	-0.9%	1.9%
	Medium to fine	0.3%	-0.1%	-0.8%
Convergence ratio (R_G)		0.27	0.17	0.43
Estimated order of accuracy (P_G)		3.26	4.35	2.08
Grid convergence index ($GCI_{G_2}^{21}$)		0.5%	0.22%	1.82%

The computational simulations were conducted for the KVLCC2 with fixed sinkage and trim at the Froude number and Reynolds number corresponding to those of the experimental data of Kim *et al.* (2001). In Table 4, a statistical value of the computed total resistance coefficient, $C_T = R/(0.5\rho U_\infty^2 S)$, and errors are presented. The errors were estimated from the difference between the calculated value and the experimental data. The error for the present results on the medium and fine grids was well below 1%, implying that reasonable agreement with the experimental data was achieved.

Furthermore, reasonable grid convergence was obtained for the total resistance coefficient with only a relatively small change in spite of further refinement. Therefore, the medium grid was adopted for the present numerical simulations considering the computational efficiency.

Table 4 Non-dimensional total resistance coefficient at the drift angle of 0°

	$C_T \times 10^3$ coarse grid	$C_T \times 10^3$ medium grid	$C_T \times 10^3$ fine grid	$C_T \times 10^3$ exp.
RANS (RSM)	4.154 (0.8%)	4.109 (-0.3%)	4.097 (-0.6%)	
RANS (k – ω SST)	4.055 (-1.6%)	4.090 (-0.7%)	4.096 (-0.6%)	4.12
oPANS model	4.188 (1.6%)	4.109 (-0.3%)	4.143 (0.6%)	

The flow around the KVLCC2 with U-shaped stern frame lines is characterized by the gradual development of a bilge vortex, which creates an intense distortion of the streamwise component of velocity in the wake field. The distortion is due to the transport of low momentum fluid from the region close to the hull to the center of the flow field by a longitudinal vortex. The strong longitudinal vortex is related to the formation of the bilge vortex, which leads to the so-called hook shape contours of the streamwise component of velocity in the wake field. One strong vortex is observed just below the shaft, which rotates in the direction opposite to that of the bilge vortex. The vortex is called a secondary vortex, which is generated by the bilge vortex. However, as explained by Larsson *et al.* (2011), the secondary vortex cannot be seen clearly in the experiments due to the limitation of the spatial resolution. Furthermore, in the numerical simulations, the phenomenon was hardly visible where invasive methods were used. Nevertheless, the hook shape pattern of low velocity and the secondary vortex were clearly identified in the towing

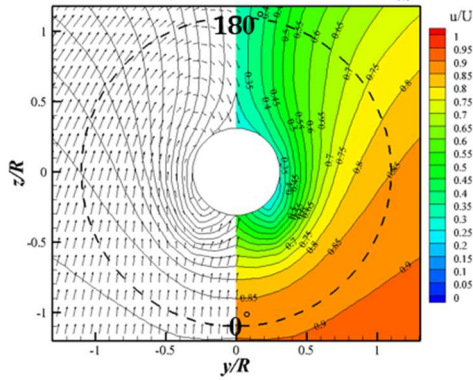
tank and wind tunnel experiments, as shown in Figure 31. Detailed physical phenomena were well described and explained in previous studies (Kim *et al.*, 2001; Lee *et al.*, 2003). In the following, the capability of the mPANS model in predicting accurate wake contours, particularly hook shape contours of the streamwise component of velocity, and the secondary vortex, was assessed and the mPANS results were compared with the RANS and oPANS results.

Figure 32 compares the contours of the streamwise component of velocity with the velocity vectors predicted by the RANS simulation with the $k - \omega$ SST model with three different grids at the drift angle of 0° . The RANS predictions showed a similar resistance value to the experimental data, but Figure 33 (a)-(c) presents no hook shape pattern of low velocity on the propeller plane, regardless of grid resolution. In addition, with grid refinement, the strength of the secondary vortex at $r/R = 0.35$ increases, while the streamwise component of velocity was similar to each other in the region where r/R was higher than 0.8. Although the velocity distributions were little influenced by the grid resolution, the isotropic turbulence model could not reproduce details of the vortex and the accurate hook shape pattern of low velocity (Larsson *et al.*, 2013). Figure 33 (d)-(f) shows that the distribution of the streamwise component of velocity was identical to each other regardless of grid resolution.

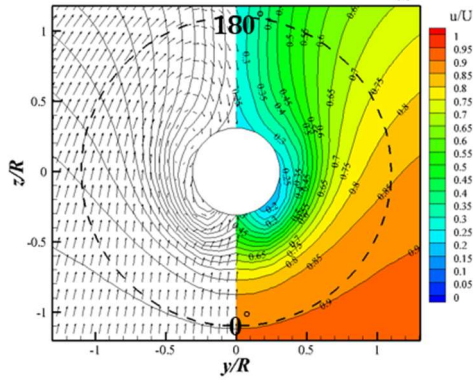
Compared to the two-equation RANS model, the RSM presented the improved prediction of hook shape contours of the streamwise component of velocity when the grid density increased, as shown in Figure 34 (a)-(c). However, the hook shape vortex was still too weak comparing to the experimental data, and the grid refinement had little effects on the accuracy of the RSM results. Furthermore, the large discrepancy for the strength of the secondary vortex is shown in Figure 35 (a) and (b). With grid refinement, the

streamwise component of velocity decreased at $r/R = 0.35$, which was related to the developed secondary vortex. As the radial position on the propeller plane increased, the results on the coarse grid showed relatively smoothly and became close to the others. Figure 35 (c) reveals the improved hook shape pattern of low velocity in the numerical simulation on the fine grid, which could be found from the range $r/R = 0.7$ to 0.9 . Although the low velocity region could be identified from the range $\theta = 110^\circ$ to 150° , the hook shape vortex was relatively weak in Figure 35 (d)-(f). Therefore, two- and seven-equation RANS models depended strongly on the turbulence modeling rather than the grid resolution.

(a) $k - \omega$ SST (coarse grid)_{0.3}



(b) $k - \omega$ SST (medium grid)_{0.3}



(c) $k - \omega$ SST (fine grid)_{0.3}

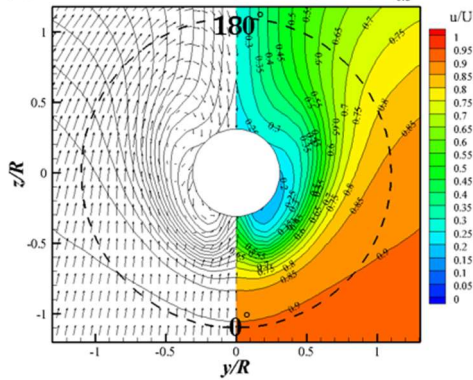


Figure 32 Contours of the streamwise component of velocity and cross-plane vectors on the propeller plane from the $k - \omega$ SST model result

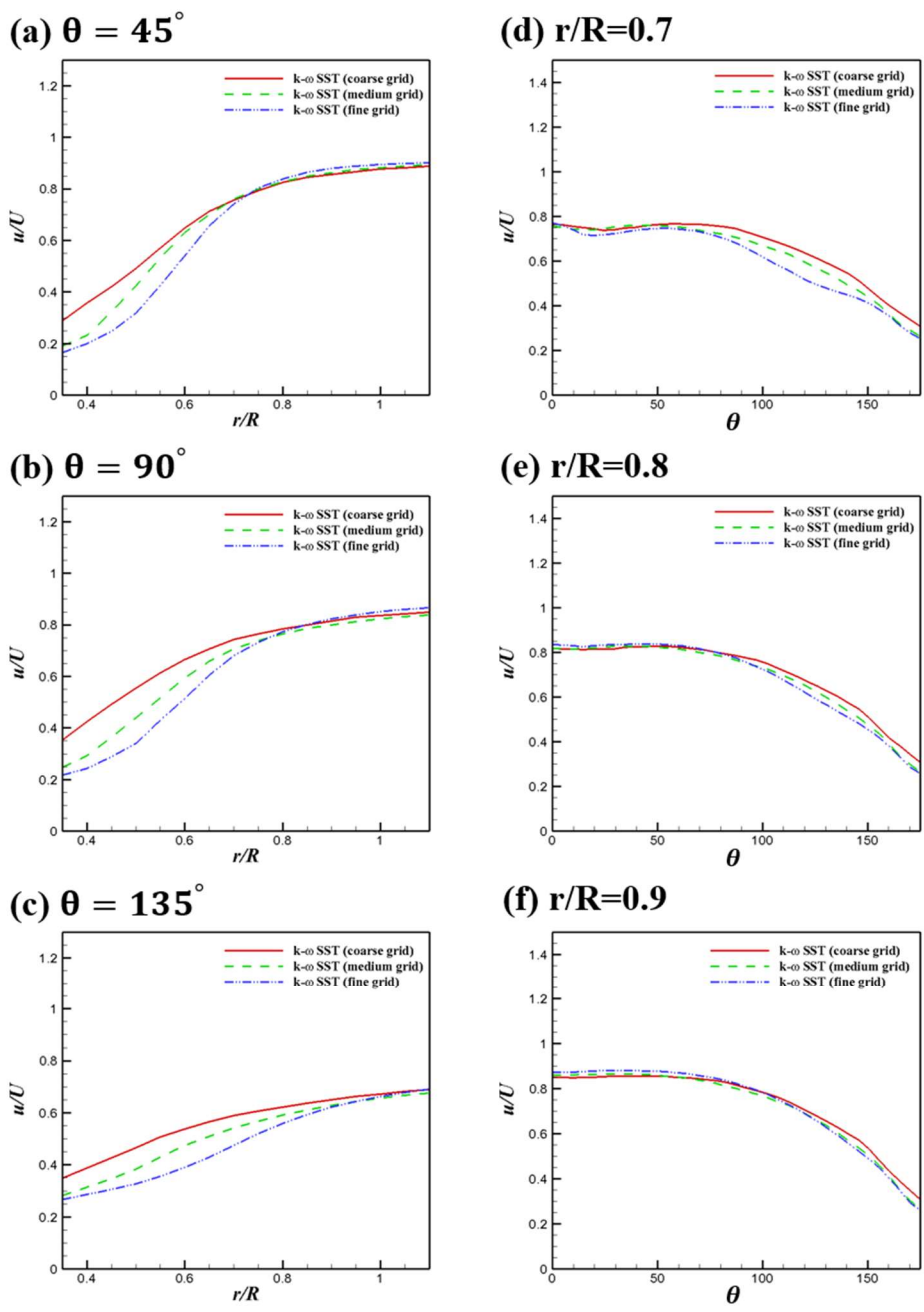


Figure 33 Radial and circumferential distributions of the streamwise component of velocity from the $k - \omega$ SST model results

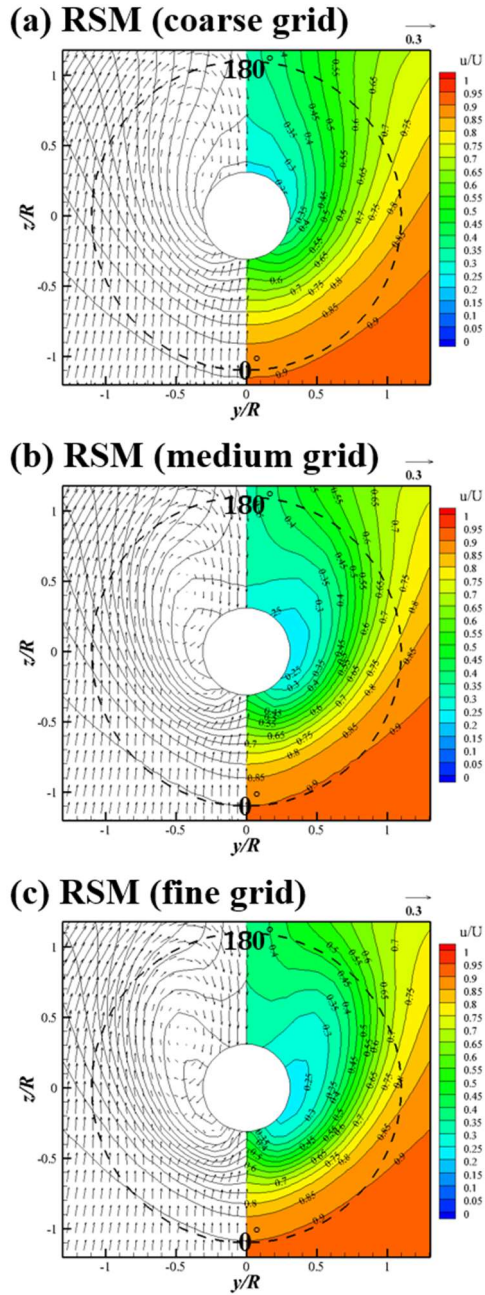


Figure 34 Contours of the streamwise component of velocity and cross-plane vectors on the propeller plane from the RSM results

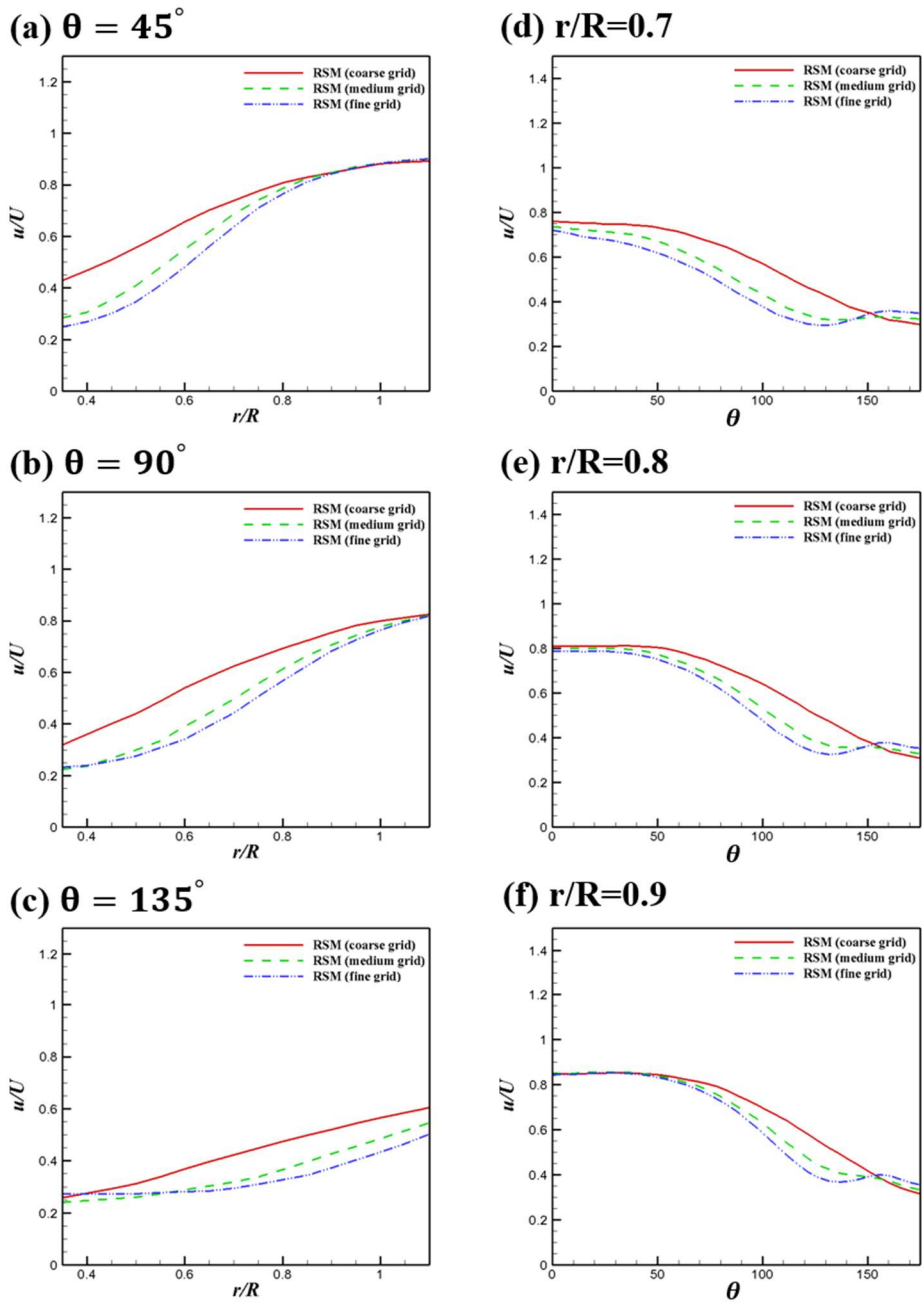


Figure 35 Radial and circumferential distributions of the streamwise component of velocity from the RSM results

Figure 36 (a) presents the wake contours from the oPANS simulation on the coarse grid. The wake contours were similar to the RANS results with $k - \omega$ SST model on the fine grid. With grid refinement, the hook shape contours of the streamwise component of velocity were significantly improved compared with the different turbulence models, as shown in Figure 36 (b) and (c). Figure 37 (a) shows that the oPANS model on the fine grid resolved a much stronger secondary vortex, leading to a large discrepancy depending on the grid resolution at $r/R = 0.35$. The oPANS model results on the medium and fine grids led to a relatively low velocity region from $r/R = 0.4$ to 0.8 , see Figure 37 (b). In addition, the relatively lower velocity region was also captured between $r/R = 0.6$ and 0.9 , as shown in Figure 37 (c). Like the RSM results, the oPANS model presented the hook shape pattern of low velocity from the range $\theta = 110^\circ$ to 150° , whereas its strength was stronger compared to the RSM results as the grid resolution increased in Figure 37 (d)-(f). It indicates that the oPANS model yielded improved hook shape pattern of low velocity compared to the RSM. In PANS simulations, increasing the grid resolution reduced the f_k value, which in turn decreased the turbulent viscosity. So, the oPANS model could resolve the smaller scale structures. Therefore, the hook shape contours of streamwise component of velocity predicted by the oPANS simulation on the fine grid were in good agreement with the experimental data.

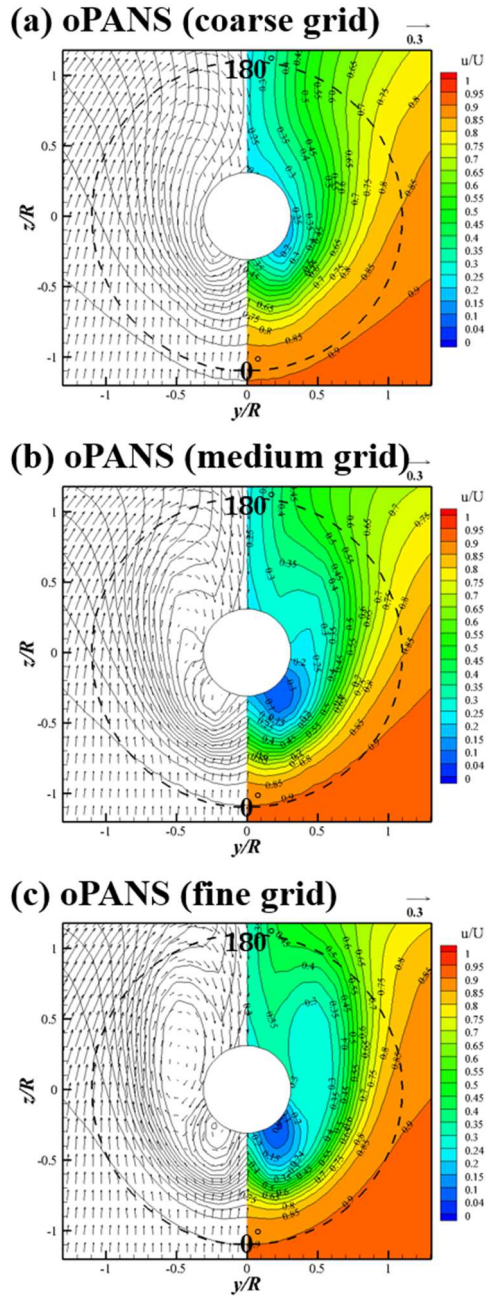


Figure 36 Contours of the streamwise component of velocity and cross-plane vectors on the propeller plane from the oPANS results

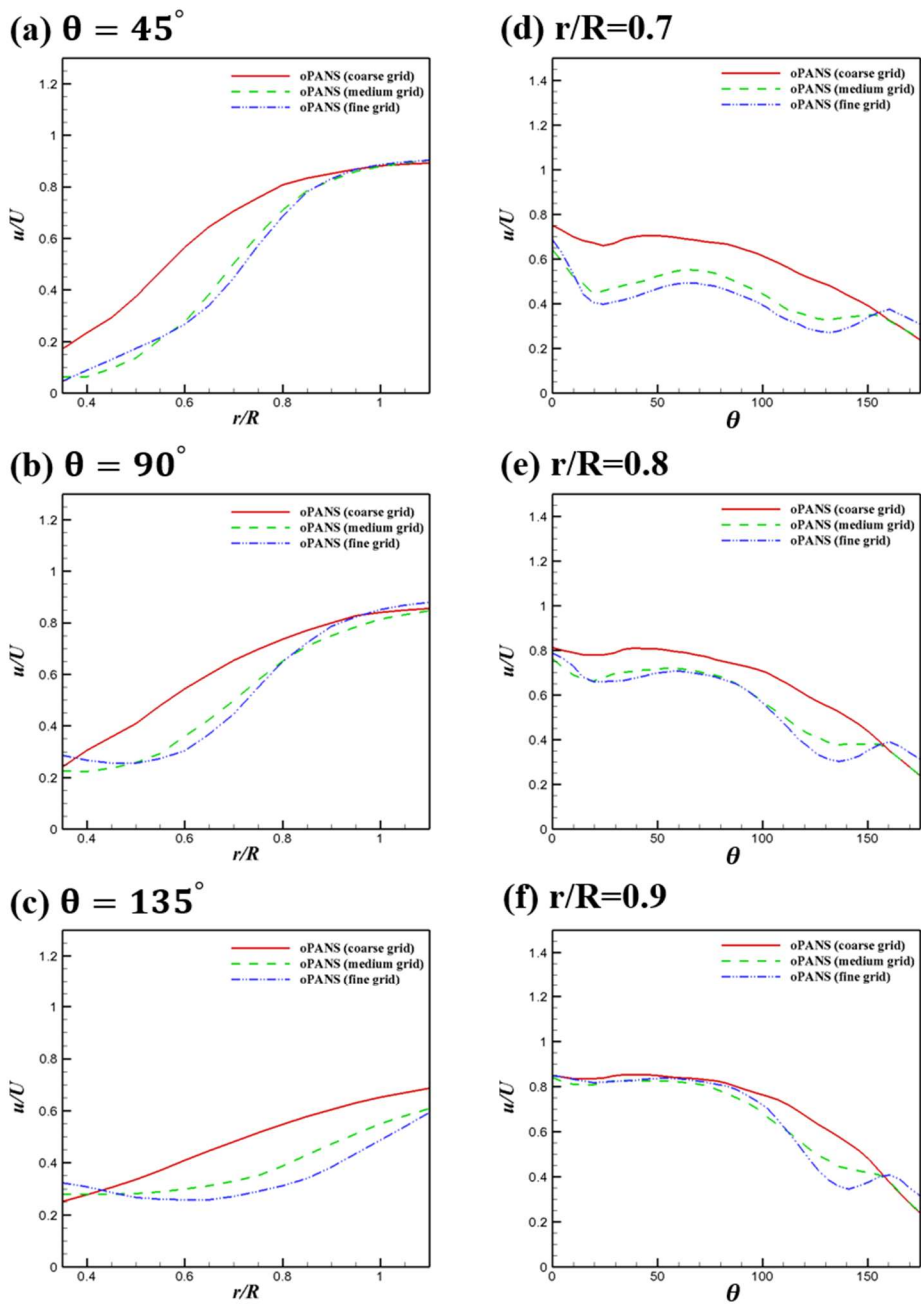


Figure 37 Radial and circumferential distributions of the streamwise component of velocity from the oPANS results

In the PANS model, the level of resolution can be controlled by specifying the value of the bridging parameter, f_k . To assess the effects of the bridging parameter, the PANS simulations with constant f_k throughout the whole domain were performed. Figure 38 shows a qualitative difference of wake contours with different bridging parameter values on the same grid resolution. The medium grid was used and six different values of f_k were selected, $f_k = 0.2, 0.3, 0.4, 0.6, 0.8$ and 1.0 .

In the case of the RANS, that is $f_k = 1.0$, the hook shape contours of the low velocity and secondary vortex were invisible, indicating an unrealistic bilge vortex in Figure 38 (a). The wake contours corresponded to the RANS results on the coarse grid. The size of hook shape pattern of low velocity became larger and got closer to the experimental data with decreasing f_k (Figure 38 (b)-(f)). The PANS simulation using $f_k = 0.2$ showed a reasonably accurate distribution of the streamwise component of velocity, but with too large size of hook shape pattern of low velocity, which means that the strength of the hook shape vortex were highly over-predicted. The PANS simulation with $f_k = 0.3$ predicted hook shape contours of the streamwise component of velocity relatively closer to the experimental data compared to the PANS simulation with $f_k = 0.2$. As a result on the medium grid, an acceptable f_k value is 0.3 . On the other hand, the PANS simulation with the smallest value of f_k does not always provide the best agreement with the experimental data at high Reynolds number (Luo *et al.*, 2014). With decreasing f_k , the lower velocity region was observed from $r/R = 0.4$ to 0.8 or from $\theta = 110^\circ$ to 150° , as shown in Figure 39. Therefore, for a good qualitative and quantitative agreement with the experimental data, an appropriate f_k that the grid can support must be selected.

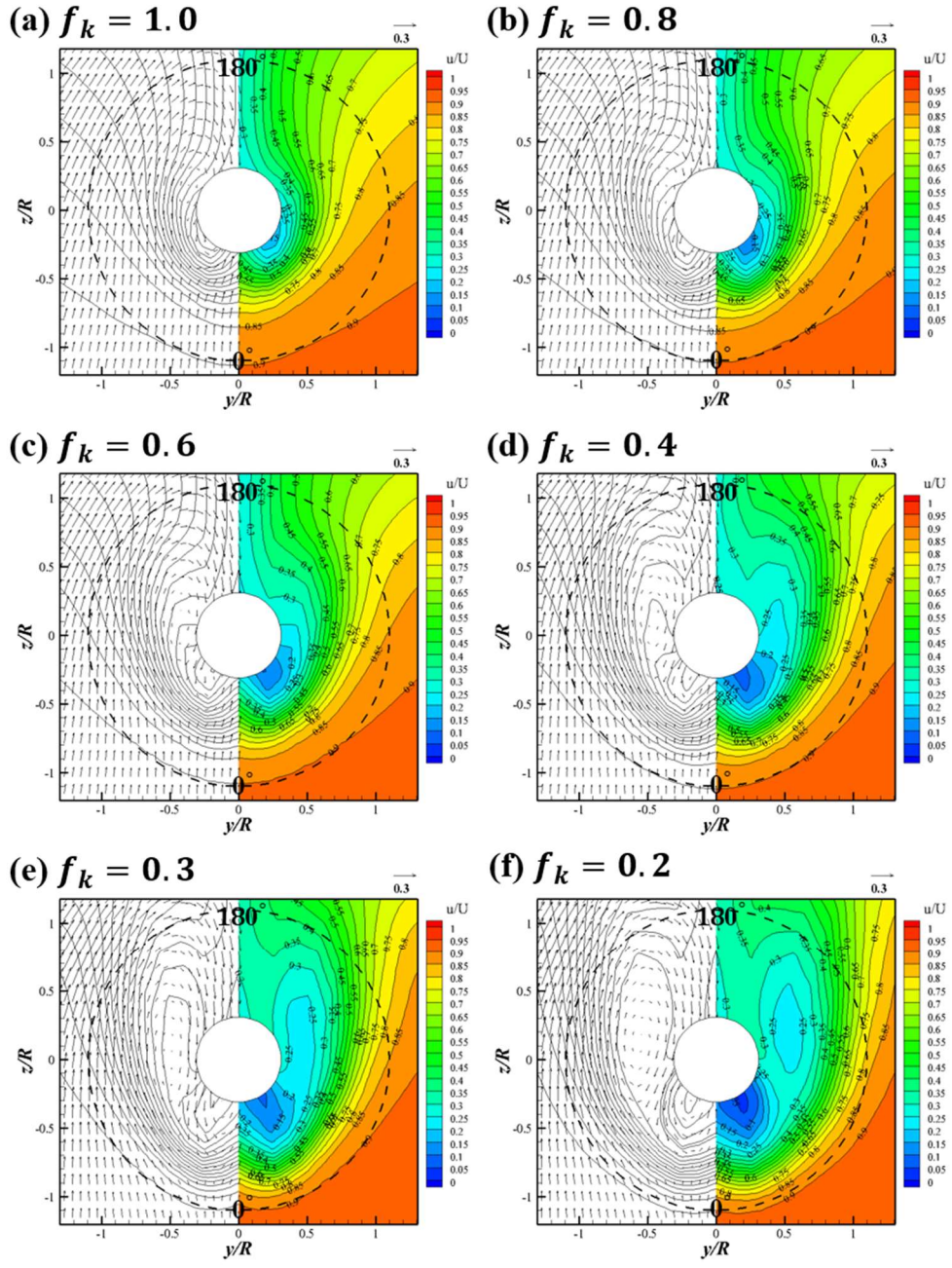


Figure 38 Contours of the streamwise component of velocity and cross-plane vectors on the propeller plane from the PANS results with constant f_k values

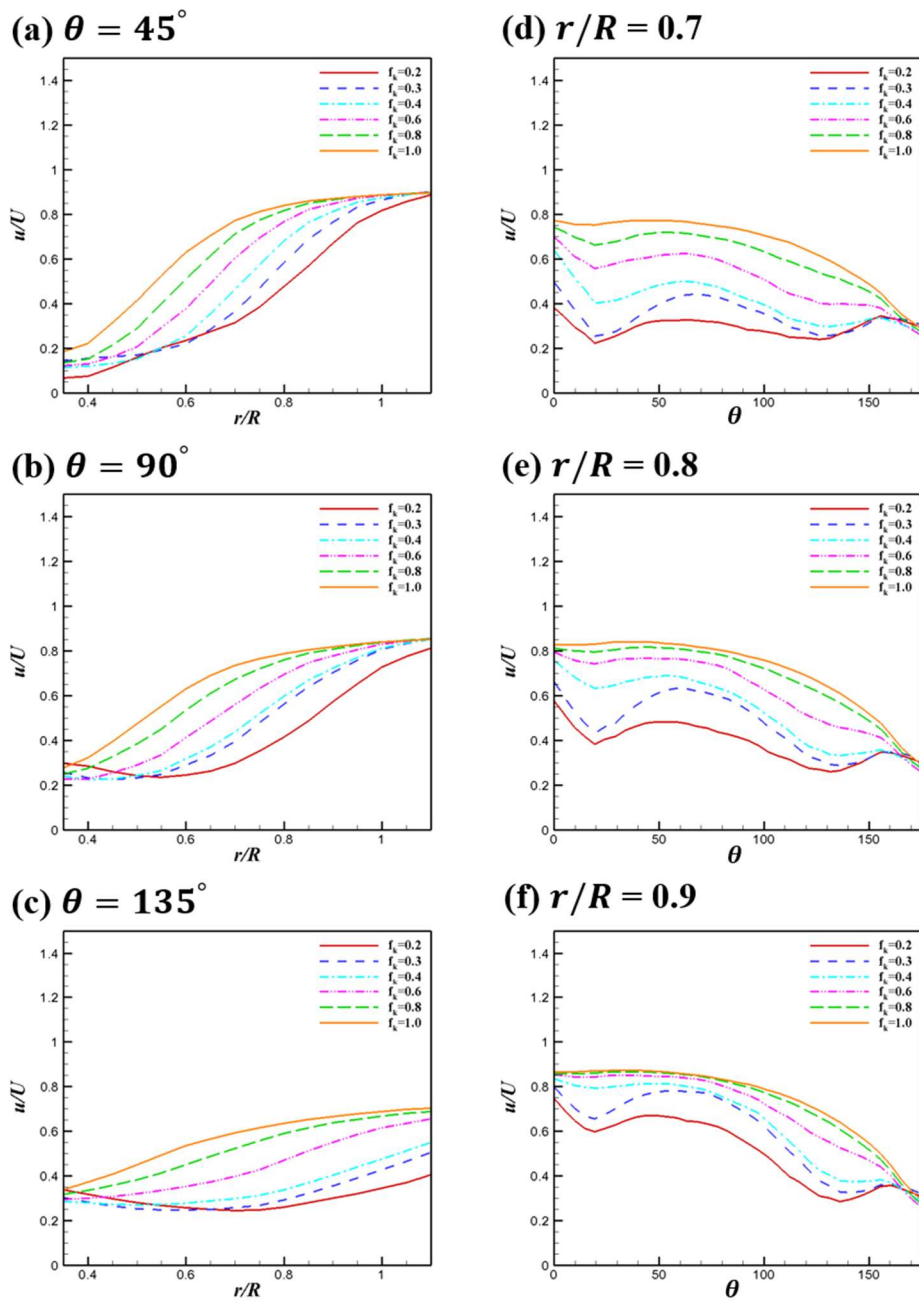


Figure 39 Radial and circumferential distributions of the streamwise component of velocity from the PANS results with constant f_k values

On the other hand, it is impossible to determine f_k value in advance, without performing numerical simulations with the various f_k values. The f_k value suggested in the previous studies did not always provide the best results, and the smallest value of f_k did not always give the considerably improved results. In the early stages of the PANS applications, the PANS simulations with constant $f_k = 0.7$ and 0.4 provided accurate results, while the PANS simulation with constant $f_k = 0.3$ showed the best agreement of the wake contours in the present study. Therefore, the mPANS models with spatially varying f_k value, which is defined by the grid spacing and integral length scale of turbulence, were used to resolve the accurate hook shape contours of the streamwise component of velocity. To resolve the anisotropy of the Reynolds stress, the turbulent kinetic energy in an integral length scale was calculated using the RSM and the ARSM, named mPANS-R and mPANS-A, respectively. Both the RSM and the ARSM can account for the directional effects of the Reynolds stress and complex interaction in the turbulent flow.

Figure 40 shows the contours of the streamwise component of velocity with velocity vectors and unresolved turbulent kinetic energy distribution on the propeller plane obtained by using the oPANS, mPANS-R and mPANS-A models on the medium grid, respectively. The mPANS simulations revealed better agreement with the experimental data comparing to the oPANS, but they still under-estimated the hook shape pattern of low velocity. Although the modeled turbulent kinetic energy was reduced by considering the anisotropy of the Reynolds stress in the mPANS-R and mPANS-A models, they still provided large unresolved turbulent kinetic energy, leading to the large modeled eddy viscosity. So, the mPANS-R and mPANS-A models failed to predict the accurate hook shape pattern of low velocity. To provide the best possible closure at the given level of physical resolution, the unresolved

turbulence kinetic energy should be further reduced.

Figure 41 shows radial distributions of the streamwise component of mean velocity at three angles, corresponding to the $\theta = 45^\circ$, 90° and 135° where θ is the circumferential angle, counter-clockwise from 0° (bottom) to 360° (top). In addition, it shows the distributions of the streamwise component of mean velocity at three radial locations ($r/R = 0.7, 0.8$ and 0.9) with respect to θ . These quantities were predicted by the oPANS and mPANS-R and mPANS-A models. Figure 41 (a) - (c) shows that both the mPANS-R and mPANS-A models predicted a slightly lower streamwise component of velocity along the radial direction than the original PANS model, while these numerical simulations presented the similar strength of the secondary vortex at $r/R = 0.35$. Figure 41 (d) - (f) shows that mPANS-R and mPANS-A captured the low velocity region at $\theta = 135^\circ$ and they also provided distribution of the smaller streamwise component of velocity along the circumferential direction. On the other hand, the mPANS-R and mPANS-A models showed little improved results as compared with the oPANS results.

The mPANS-BR, mPANS-BA, mPANS-AR and mPANS-AA models, as mentioned in Chapter 2 were applied to the flow around the KVLCC2. These models reduced the f_k value near the hull surface, where the strong anisotropy of Reynolds stress existed. Many studies showed that the anisotropy of the Reynolds stress is important for capturing the accurate hook shape contours of the streamwise component of velocity (Larsson *et al.*, 2003). With decreasing f_k , more resolved scales of coherent structure motion were resolved, resulting in improving predicted accuracy significantly.

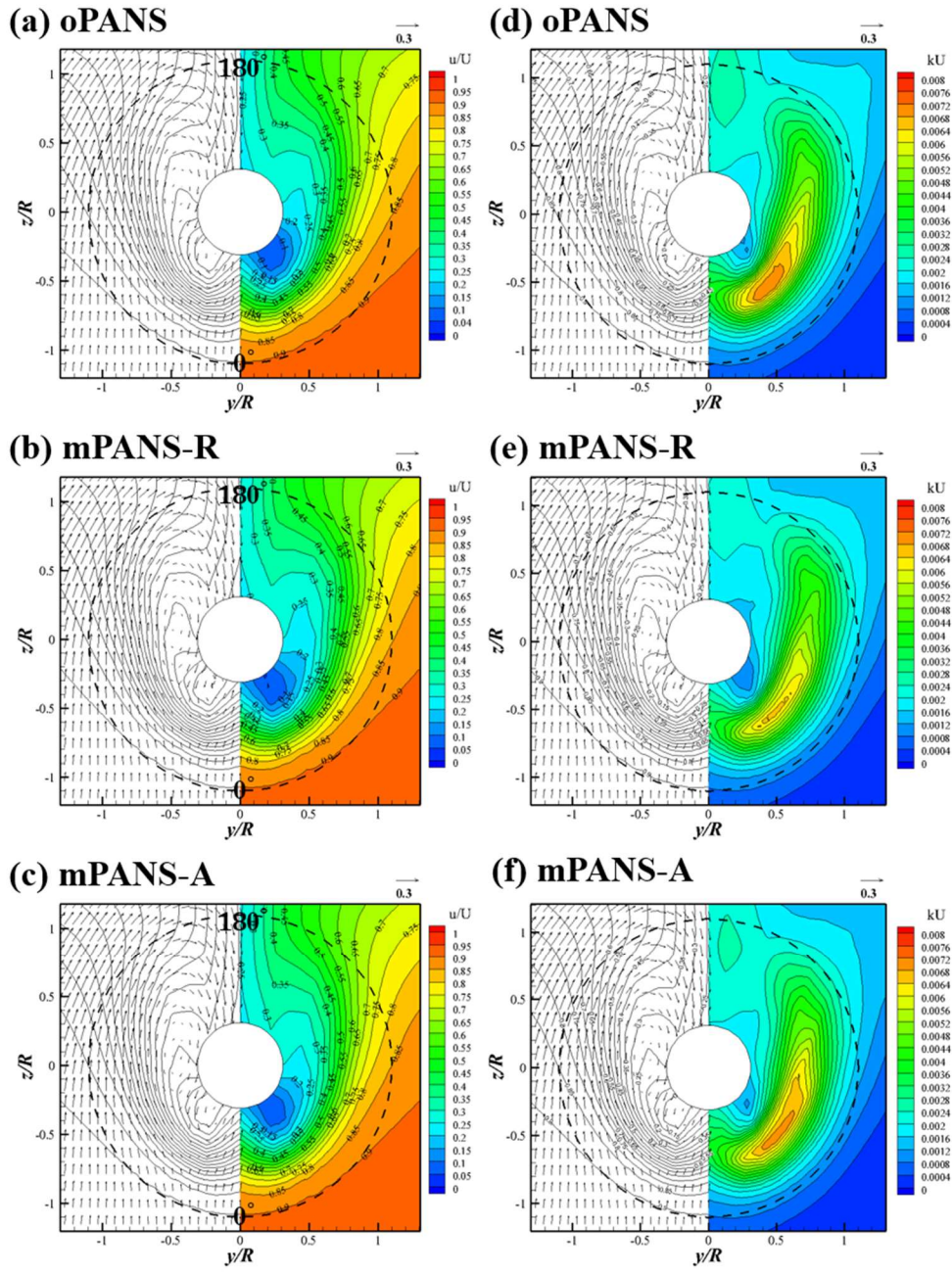


Figure 40 Comparison of the results for the oPANS, mPANS-R and mPANS-A models. Left column: streamwise component of velocity; Right column: unresolved turbulence kinetic energy

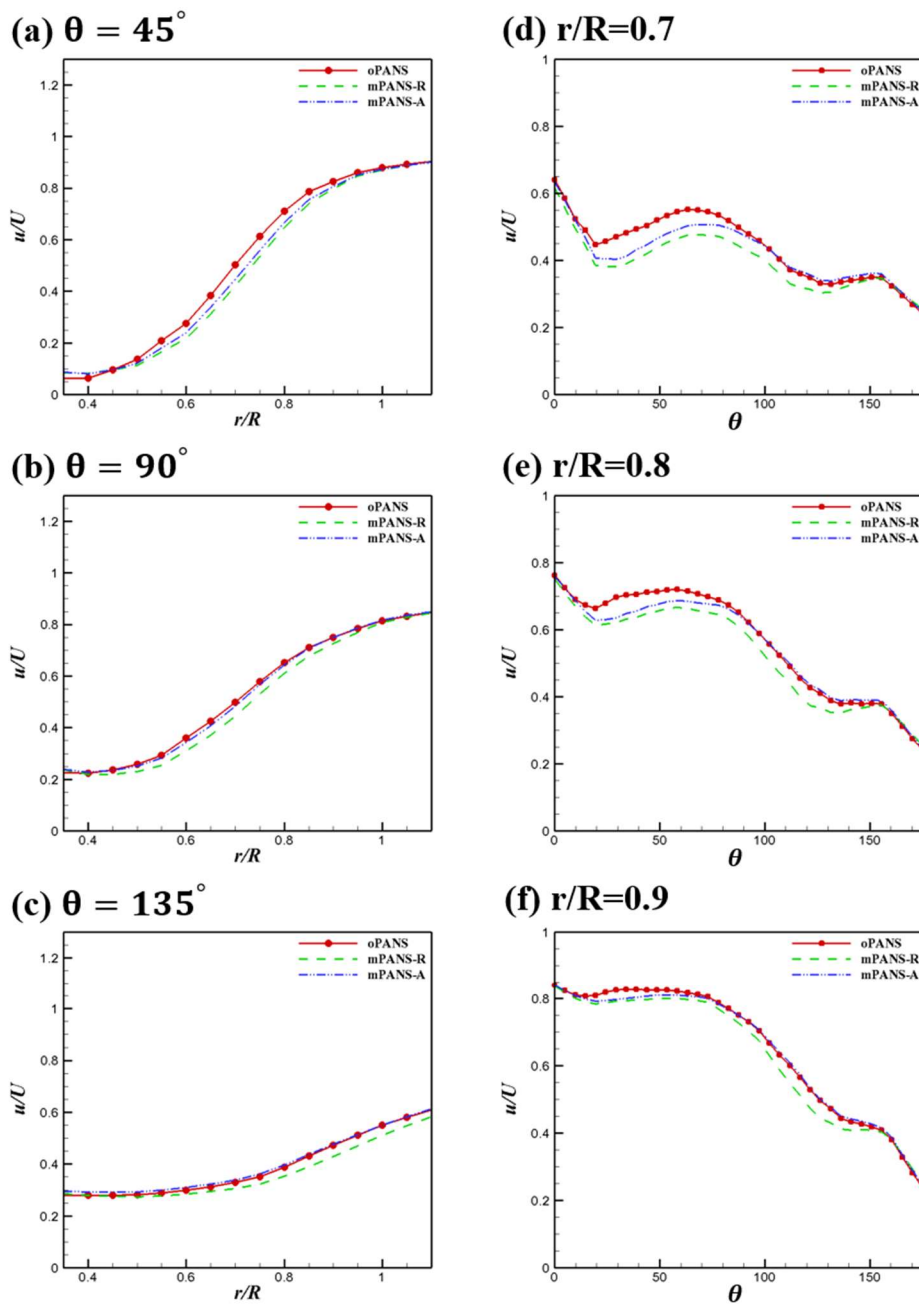


Figure 41 Radial (left column) and circumferential (right column) distributions of the streamwise component of velocity from the oPANS, mPANS-R and mPANS-A results

The predicted contours of the streamwise component of velocity and velocity vectors from the mPANS-BR, mPANS-BA, mPANS-AR, and mPANS-AA models on the medium grid are shown in Figure 42. Although the oPANS model failed to resolve the hook shape contours of the streamwise component of velocity on the propeller plane, the hook shape pattern of low velocity obtained by using the mPANS model was clearly visible. In addition, as the hook shape pattern of low velocity was quite well reproduced when compared to experimental data, it can be predicted that the bilge vortex was accurately captured.

Figure 43 shows radial distributions of the streamwise component of mean velocity at three radial cuts, corresponding to the $\theta = 45^\circ$, 90° and 135° . Moreover, the distributions of the streamwise component of mean velocity at three circumferential cuts ($r/R = 0.7, 0.8$ and 0.9) with respect to θ . These quantities predicted by the oPANS and mPANS models were compared. The mPANS models showed similar radial and circumferential variation of the streamwise component of velocity. They predicted the lower velocity region with respect to r/R and θ compared to the oPANS results in Figure 43 (a)-(c). Particularly, the mPANS results observed the hump at $\theta = 135^\circ$ in the distribution of the streamwise component of velocity in Figure 43 (d)-(f), where the hook shape pattern of low velocity was observed in the experimental data.

Figure 44 shows the unresolved turbulent kinetic energy k_u , obtained by using the mPANS-BR, mPANS-BA, mPANS-AR, and mPANS-AA on the medium grid. For the same grid, a larger amount of the unresolved turbulent kinetic energy was observed for the oPANS model, indicating that the modeled eddy viscosity was large. However, the mPANS-BR, mPANS-BA, mPANS-AR, and mPANS-AA models showed that the unresolved turbulent kinetic

energy was reduced at the core of the hook shape pattern of low velocity and then more turbulence quantities were resolved compared with the oPANS results. Deng *et al.* (1994) also presented that hook shape contours of the streamwise component of velocity on the propeller plane were captured by reducing the eddy viscosity. Therefore, the prediction of the hook shape pattern of the low velocity by the mPANS models generally showed acceptable agreement with the experimental data.

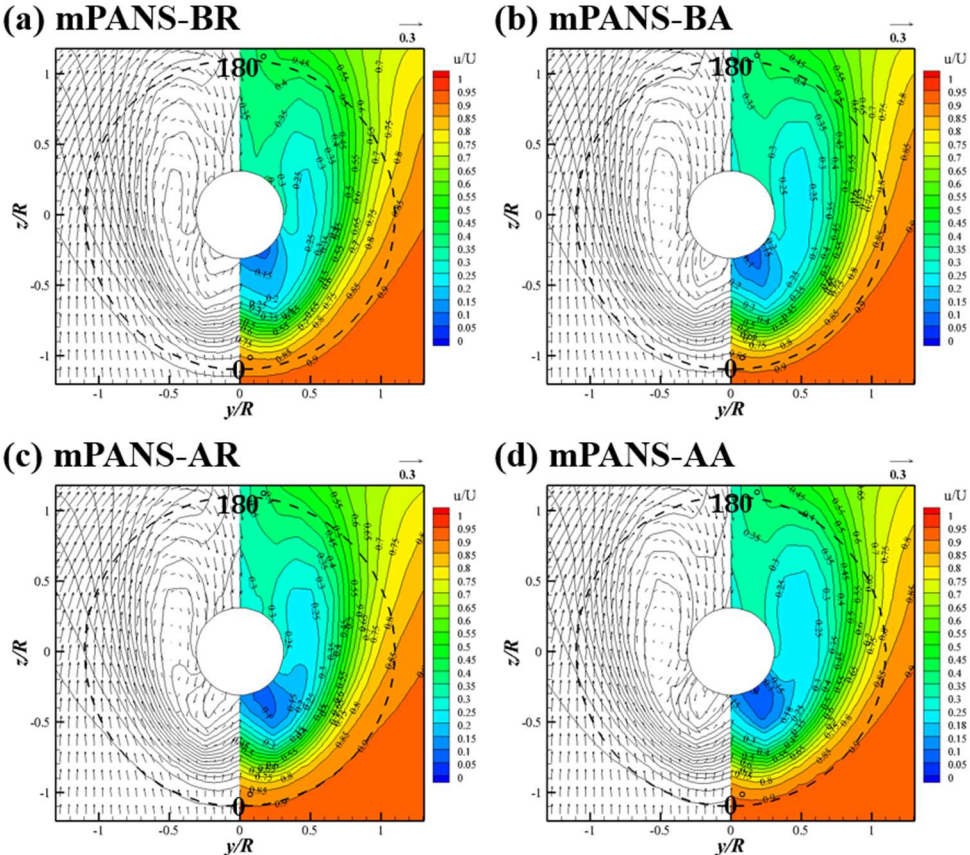


Figure 42 The contours of the streamwise component of velocity and velocity vectors from the mPANS results

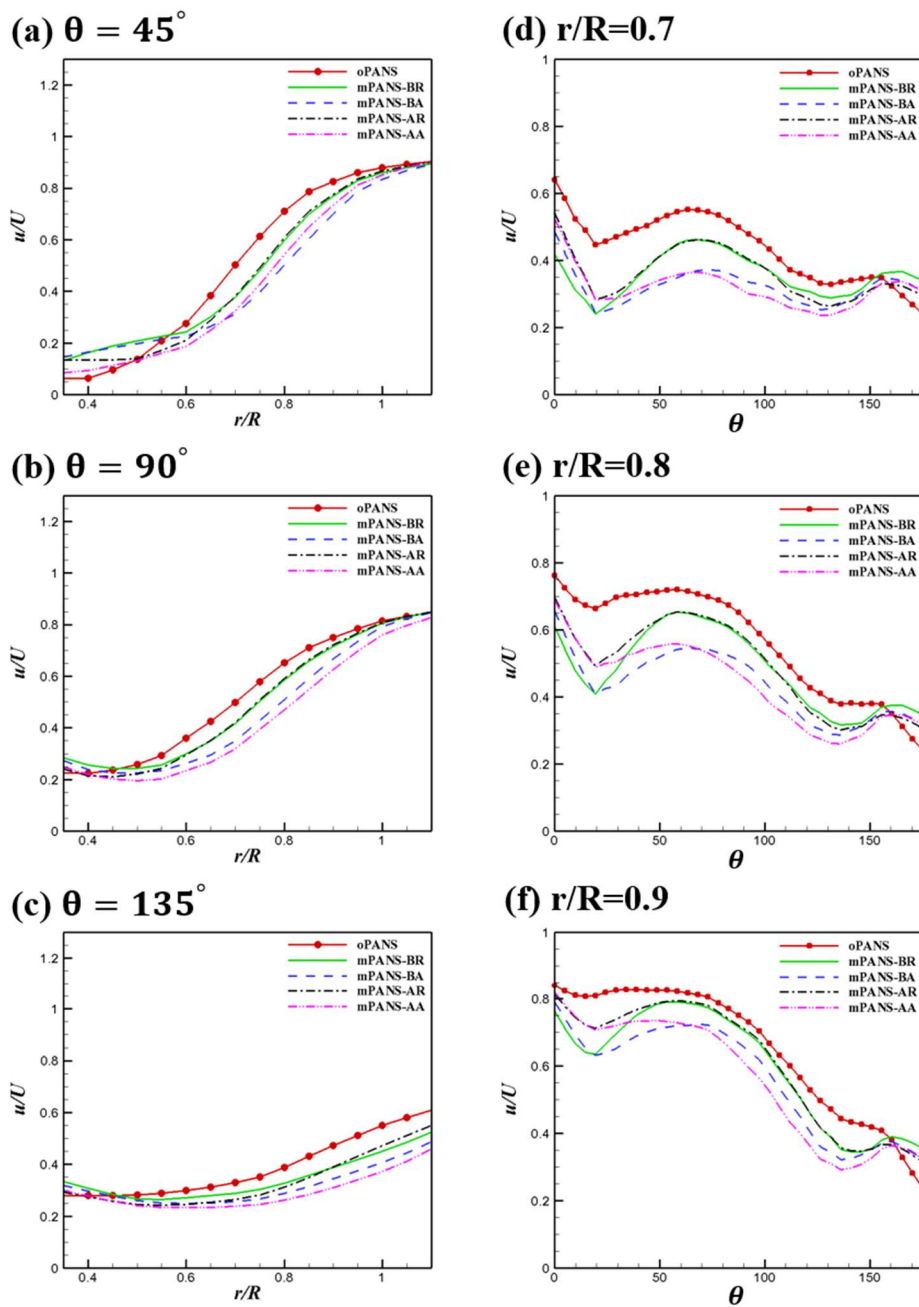


Figure 43 Radial (left column) and circumferential (right column) distributions of the streamwise component of velocity from the oPANS, mPANS results

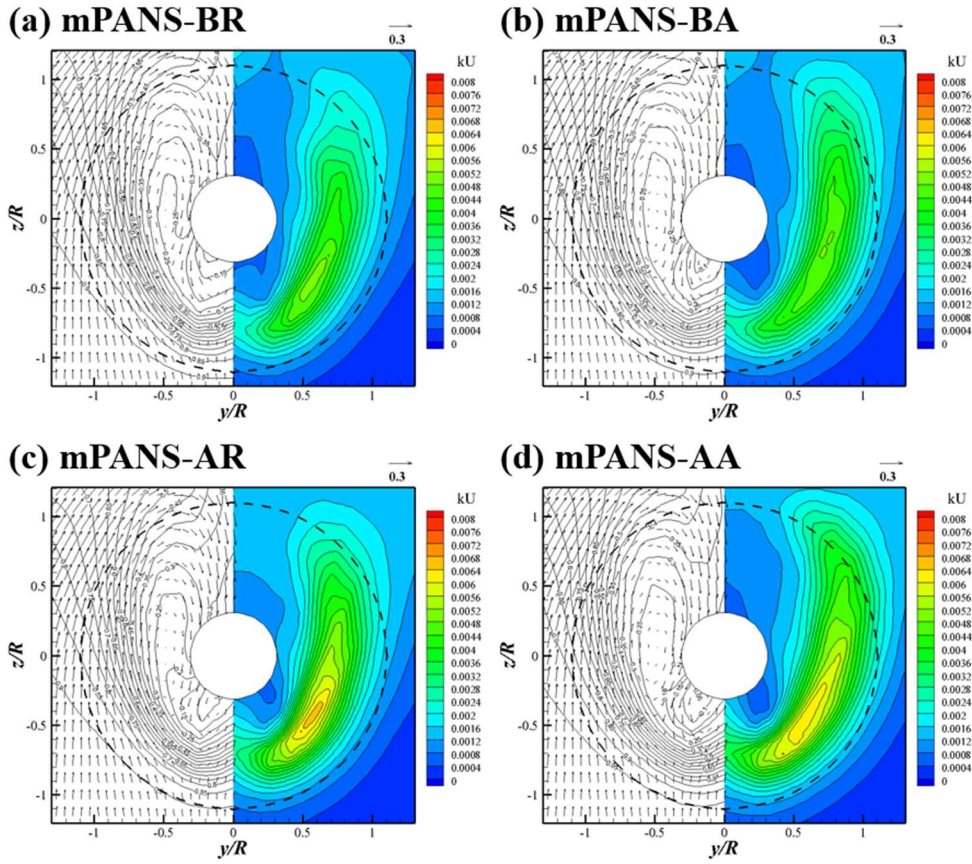


Figure 44 Contours of the unresolved turbulent kinetic energy from the mPANS results

4.3. Results and discussion for the case of $\beta = 12^\circ$

Hook shape contours of the streamwise component of velocity at the drift angle of 12° obtained from the experiment (Kume *et al.*, 2006) are shown in Figure 45. The experiments were performed using a 1:64 scaled model of the KVLCC2M at $Re = 3.935 \times 10^6$ and $Fr = 0.1424$. The wake contours were measured at $x/L_{pp} = 0.48$ using an 8-hole spherical pitot tube. The low velocity region reproduced by the aft-body side vortex was found near the transom on the windward side. On the leeward side, there were two hook shape pattern of low velocity. One was generated from the aft-body bilge vortex and located near the propeller boss. The other region of lower velocity was at a distance far from the hull, which was produced by the fore-body vortex.

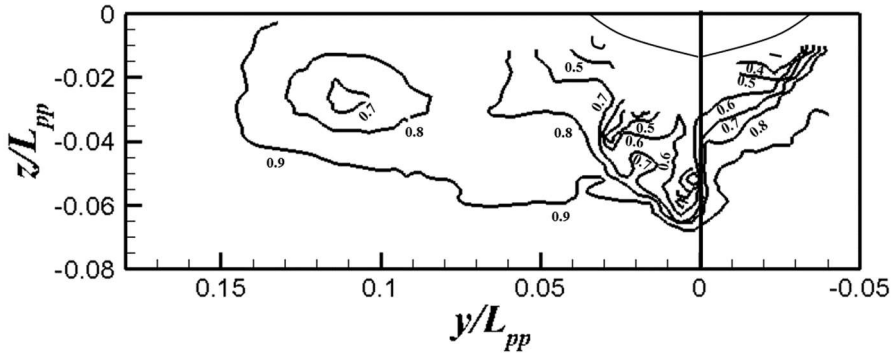


Figure 45 Contours of the streamwise component of velocity on the propeller plane at $x/L_{pp} = 0.48$ from the experimental data

The present numerical simulations were conducted at Froude number corresponding to those of the experimental data of Kume *et al.* (2006), but for different ship model (KVLCC2) and at different $Re (= 4.60 \times 10^6)$. In addition, the scale ratio used in the experiment was different from the present

numerical simulations. Nevertheless, the experimental data were used on reference because there was no experimental study on the same scaled model ship. In Table 5, the hydrodynamic forces and moment obtained from the different numerical simulations and experiments are presented at the drift angle of 12° . The hydrodynamic forces were the x- and y-direction forces C_x and C_y and the moment was the z-axis moment C_N . They were dimensionless values and defined as follows

$$\begin{aligned}
 C_x &= F_x / 0.5 \rho v^2 L_{pp} d \\
 C_y &= F_y / 0.5 \rho v^2 L_{pp} d \\
 C_N &= M_z / 0.5 \rho v^2 L_{pp}^2 d
 \end{aligned} \tag{92}$$

where F_x and F_y are the hydrodynamic forces, M_z is the moment and d is the draft.

For the drift angle of 12° , the non-dimensional forces and moment were compared with various results obtained from the experiments and different numerical simulations in Table 5. Fureby *et al.* (2016) and Xing *et al.* (2012) performed the numerical simulations using a 1:58 scaled model of the KVLCC2. Experimental data and computational results were obtained for a 1:46.43 scaled model of the KVLCC2 by Sung and Park (2015). Although they used different scaled models for the experiments and numerical simulations, these results were included for reference.

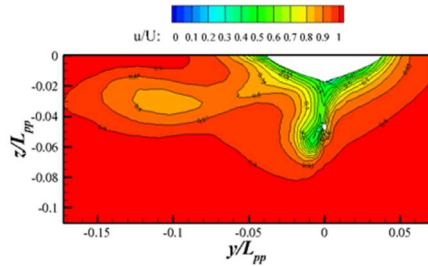
Table 5 Hydrodynamic forces and moments at the drift angle of 12°

		$C_x \times 10^3$	$C_y \times 10^3$	$C_N \times 10^3$
Kume et al., 2006	Exp.	17.5	71.0	25.4
Fureby et al., 2016	RANS	20.7 (18.2%)	71.0 (0.0%)	25.9 (2%)
	Hybrid RANS/LES	19.1 (9.1%)	72.5 (2.1%)	25.0 (-1.6%)
	WM-LES	17.2 (-1.7%)	79.0 (11.2%)	23.2 (-8.7%)
Xing et al., 2012	DES	20.5 (17.1%)	74.0 (4.2%)	25.2 (-0.4%)
Sung and Park, 2015	Exp.	16.64 (-4.9%)	67.4 (-5.0%)	26.5 (4.3%)
	RSM	15.11 (-11.4%)	67.21 (-5.3%)	25.9 (2.0%)
Present study	RANS (coarse grid)	17.8 (1.7%)	73.6 (3.6%)	24.7 (-2.7%)
	RANS (medium grid)	17.0 (-2.8%)	69.0 (-2.9%)	26.3 (3.3%)
	RANS (fine grid)	17.1 (-2.4%)	69.2 (-2.6%)	26.8 (5.2%)
	oPANS (coarse grid)	18.3 (4.5%)	75.3 (5.7%)	24.0 (-6.0%)
	oPANS (medium grid)	17.2 (-1.9%)	69.5 (-2.1%)	25.9 (2.0%)
	oPANS (fine grid)	17.2 (-1.7%)	69.6 (-2.0%)	26.3 (3.5%)

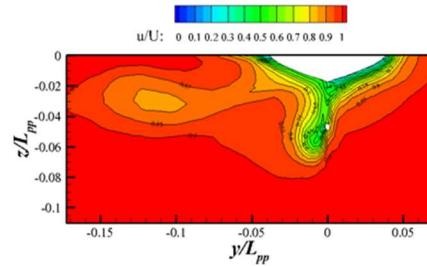
The errors for forces and moment were calculated based on the experimental data in Kume *et al.* (2006). The errors were between -2.8% and 4.5% for the x-direction force, C_x , between -2.9% and 5.7% for the y-direction force, C_y , and between -6.0% and 5.2% for the z-axis moment, C_N . Fureby *et al.* (2016) and Xing *et al.* (2012) showed large errors in the x-direction force, which did not take into account the free surface. As mentioned above, Sung and Park (2015) used the different scaled model ships for numerical simulation and experiments. It is difficult to compare these results quantitatively, but the reliability of the present results can be evaluated. Table 5 shows the sensitivity of the statistics to the grid size. The difference of the values for forces and moment between the medium and fine grids were less than 0.5% and 2%, respectively. The present results were slightly changed as the grid resolution increased, and the errors were small compared to other results.

Figure 46 shows the contours of the non-dimensional streamwise component of velocity, u/U_∞ , and velocity vectors on the propeller plane ($x/L_{pp} = 0.48$) using the two-equation RANS model and oPANS model on the coarse, medium and fine grids at the drift angle of 12° . The RANS prediction based on the $k - \omega$ SST model showed hook shape contours of the streamwise component of velocity on the leeward side, which was generated from the fore-body side vortex and located far from the hull. Moreover, the hook shape pattern of low velocity was significantly extended on the leeward side. On the other hand, the RANS model did not reveal any low velocity regions near the propeller boss on the leeward side and transom on the windward side. With the grid refinement, the low velocity region near the propeller boss was shown on the medium grid, but hook shape vortex was relatively weak. Although the RANS simulation using the fine grid captured the hook shape pattern of low velocity near the propeller boss, it failed to predict the low velocity region below the transom on the windward side. The oPANS simulation on the coarse grid also showed similar results to the RANS simulation on the coarse grid. For the medium grid, the hook shape contours of the streamwise component of velocity was clearly observed for the oPANS model than the RANS model. With grid refinement (decreasing the f_k value), more unsteady and three-dimensional scales of motion were captured, as indicated in the instantaneous velocity contours. The oPANS simulation on the fine grid captured more resolved scales of coherent structure motion, resulting in the accurate prediction of the hook shape pattern of low velocity on the propeller plane. In addition, the low velocity region below the transom on the windward side could be seen more clearly than the one obtained by using the RANS model on the fine grid.

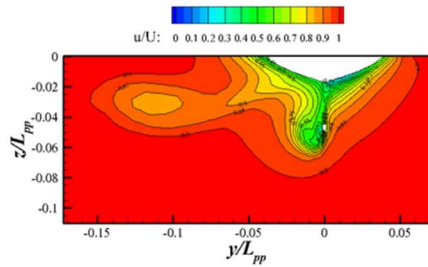
(a) RANS (coarse grid)



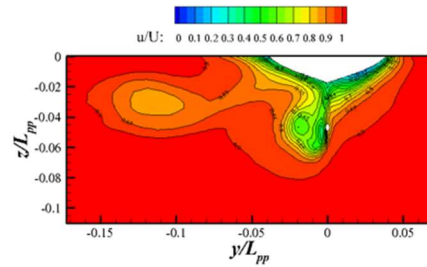
(d) oPANS (coarse grid)



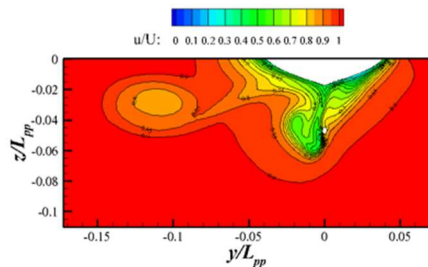
(b) RANS (medium grid)



(e) oPANS (medium grid)



(c) RANS (fine grid)



(f) oPANS (fine grid)

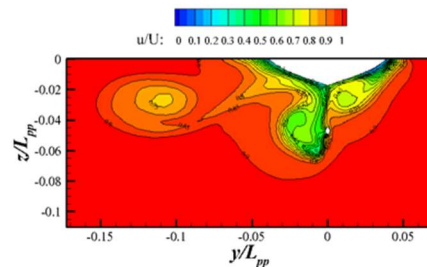
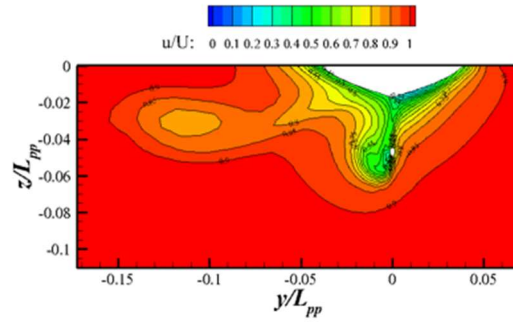


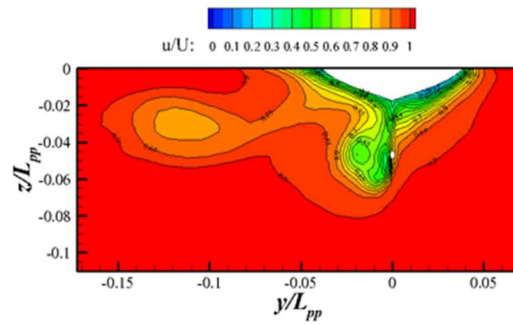
Figure 46 Contours of the streamwise component of velocity on propeller plane from the RANS and oPANS results

Figure 47 shows the comparison with the two-equation RANS, oPANS model and mPANS-BR model for the streamwise component of mean velocity on the propeller plane. On the leeward side, contours of two hook shape contours of the streamwise component of velocity were observed in experimental data. The RANS model failed in predicting the obvious hook shape pattern of low velocity near the propeller boss. Even uniform distributions of the streamwise component of velocity were shown. On the windward side, the low velocity region near the transom was compressed from both the RANS and oPANS predictions. However, in the mPANS-BR model, the region of the low streamwise component of velocity near the transom was captured on the windward side, which was also shown in Xing *et al.* (2012) and Abbas and Kornev (2016). The other results obtained by using the modified PANS-BA, AR, and AA models were similar to the one found in the modified PANS-BR model, as shown in Figure 48. The mPANS models achieved the accurate predictions of hook shape contours of the streamwise component of velocity on the propeller plane at a given grid resolution, as compared to those obtained by using the oPANS model on the same grid.

(a) RANS



(b) oPANS



(c) mPANS-BR

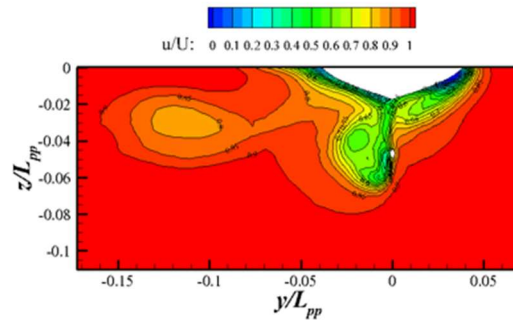
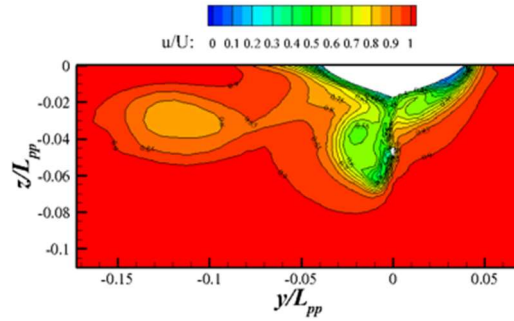
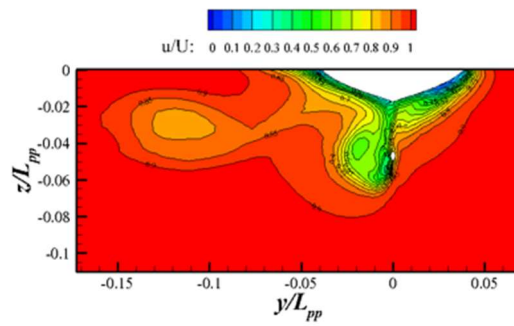


Figure 47 Contours of the streamwise component of velocity on the propeller plane from the RANS, oPANS and mPANS-BR results

(a) mPANS-BA



(b) mPANS_AR



(c) mPANS-AA

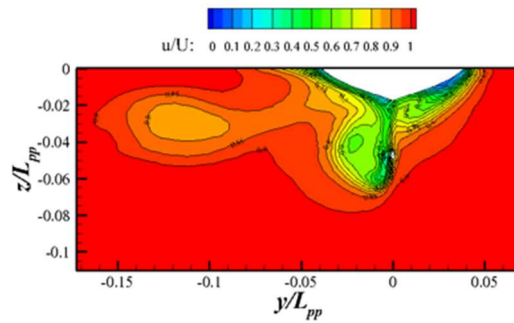


Figure 48 Contours of the streamwise component of velocity on the propeller plane from the mPANS-BA, mPANS-AR and mPANS-AA results

The previous studies focused on an understanding of the complex vortical topology and associated surface flow characteristics at the drift angle of 12° as the flow around the hull was highly complex. Figures 49 and 50 show the instantaneous flow structures around the hull, predicted by the RANS model and oPANS model at the drift angle of 12° . These results were shown for three grids: coarse, medium and fine grids. The vortical structures were represented by iso-surface of the positive value of the second invariant of the velocity gradient tensor, which is Q-criterion. An iso-surface with the positive Q indicates vortical structures (Jeong and Hussain, 1995). The second invariant Q is defined as

$$Q = -\frac{1}{2} \left(\frac{\partial u_i}{\partial x_j} \times \frac{\partial u_j}{\partial x_i} \right) = \frac{1}{2} (\Omega_{ij}^2 - S_{ij}^2) \quad (93)$$

where S_{ij} and Ω_{ij} are the symmetric and antisymmetric components of the velocity gradient, $S_{ij} = (\partial u_i / \partial x_j + \partial u_j / \partial x_i)$ and $\Omega_{ij} = (\partial u_i / \partial x_j - \partial u_j / \partial x_i)$, respectively.

Figures 49 and 50 show visualizations of Q colored by x-directional vorticity, looking up from beneath the hull. Complicated vortex systems, such as fore-body side vortex, fore-body bilge vortex, aft-body bilge vortex, and aft-body hairpin vortex, were observed on the leeward and windward sides. The RANS simulations on the coarse grid captured the complicated vortex systems. On the other hand, the predicted fore-body side vortex was short and the aft-body hairpin vortex was too weak as compared with the previous results (Xing *et al.*, 2012). With the grid refinement, the fore-body side vortex was lengthy, while the RANS results on the fine grid remained unsatisfactory.

The oPANS simulation on the coarse grid showed similar fore-body side vortex to the RANS simulation on the coarse grid. However, for the oPANS simulation, grid refinement led to the appearance of the aft-body side vortex as well as the longer fore-body side vortex and aft-body hairpin vortex. The oPANS model on the medium grid resolved the aft-body side vortex on the leeward side. On the other hand, the original PANS model on the fine grid captured the aft-body side vortex on the windward side as well as on the leeward side. The aft-body side vortex on the windward side was directly related to low velocity regions near the transom on the windward side on the propeller plane. Therefore, the oPANS model resolved more turbulence scale and finer structures, resulting in the accurate representation of the vortical structures.

As shown in Figure 51, it can be seen that the RANS and oPANS models resolved the shorter fore-body side vortex compared with the previous results (Xing *et al.*, 2012). Additionally, the oPANS approach failed to predict the aft-body side vortex on the medium grid, while the oPANS simulation on the fine grid resolved it. The mPANS models were applied to achieve the accurate prediction of the fore-body side vortex as well as aft-body side vortex. Figures 51 and 52 show the bottom view of the instantaneous vortical structures at the drift angle of 12° . Unlike the RANS and oPANS models, which showed weak fore-body side vortex and no existing aft-body side vortex, the mPANS models resolved the longer fore-body side vortex and aft-body side vortex on the medium grid. The mPANS models showed fairly good agreement with the available numerical results (Xing *et al.*, 2012; Fureby *et al.*, 2016).

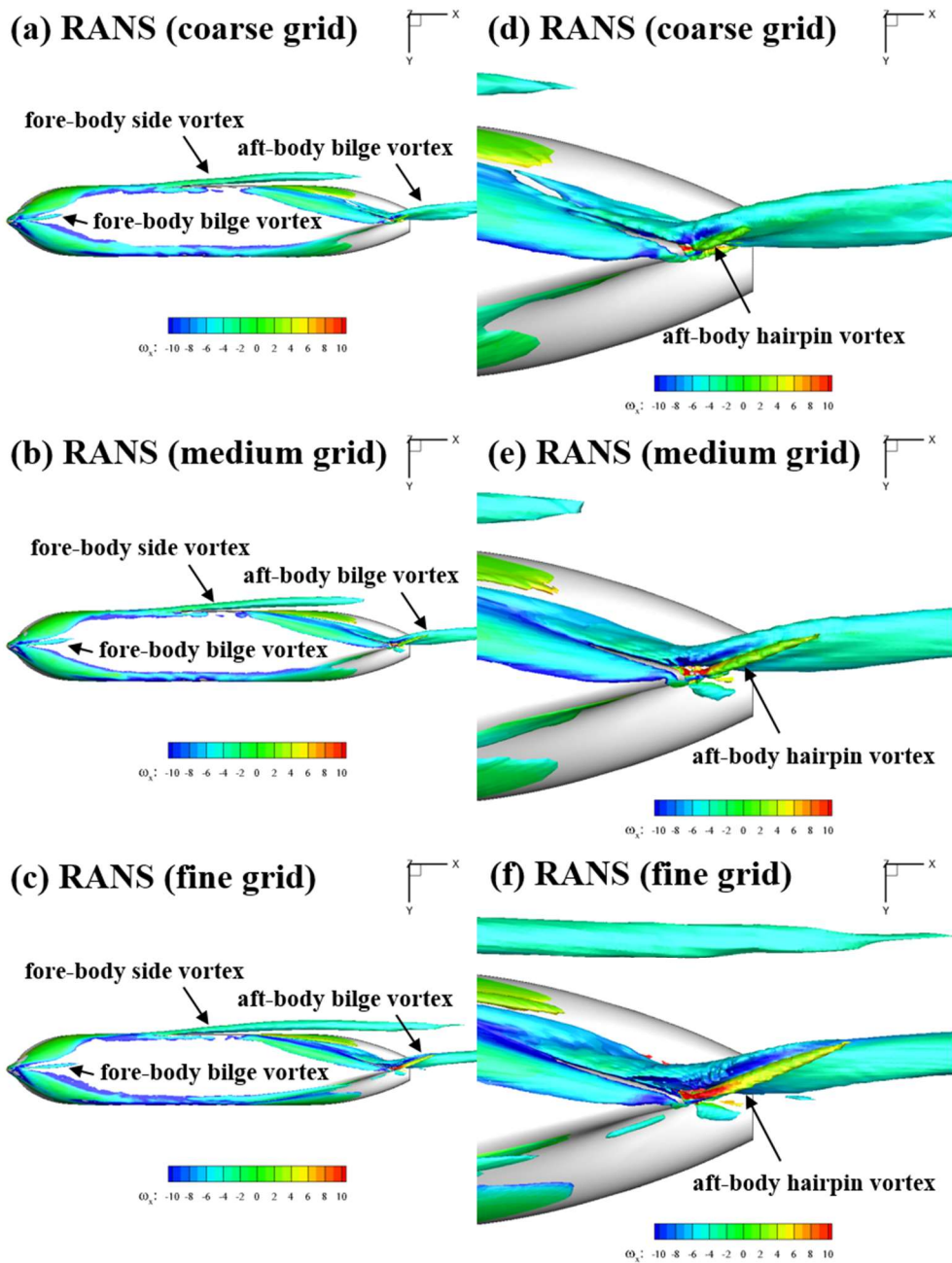


Figure 49 Vortex system around the hull from the RANS results. Left column: bottom view; Right column: zoom in near the stern

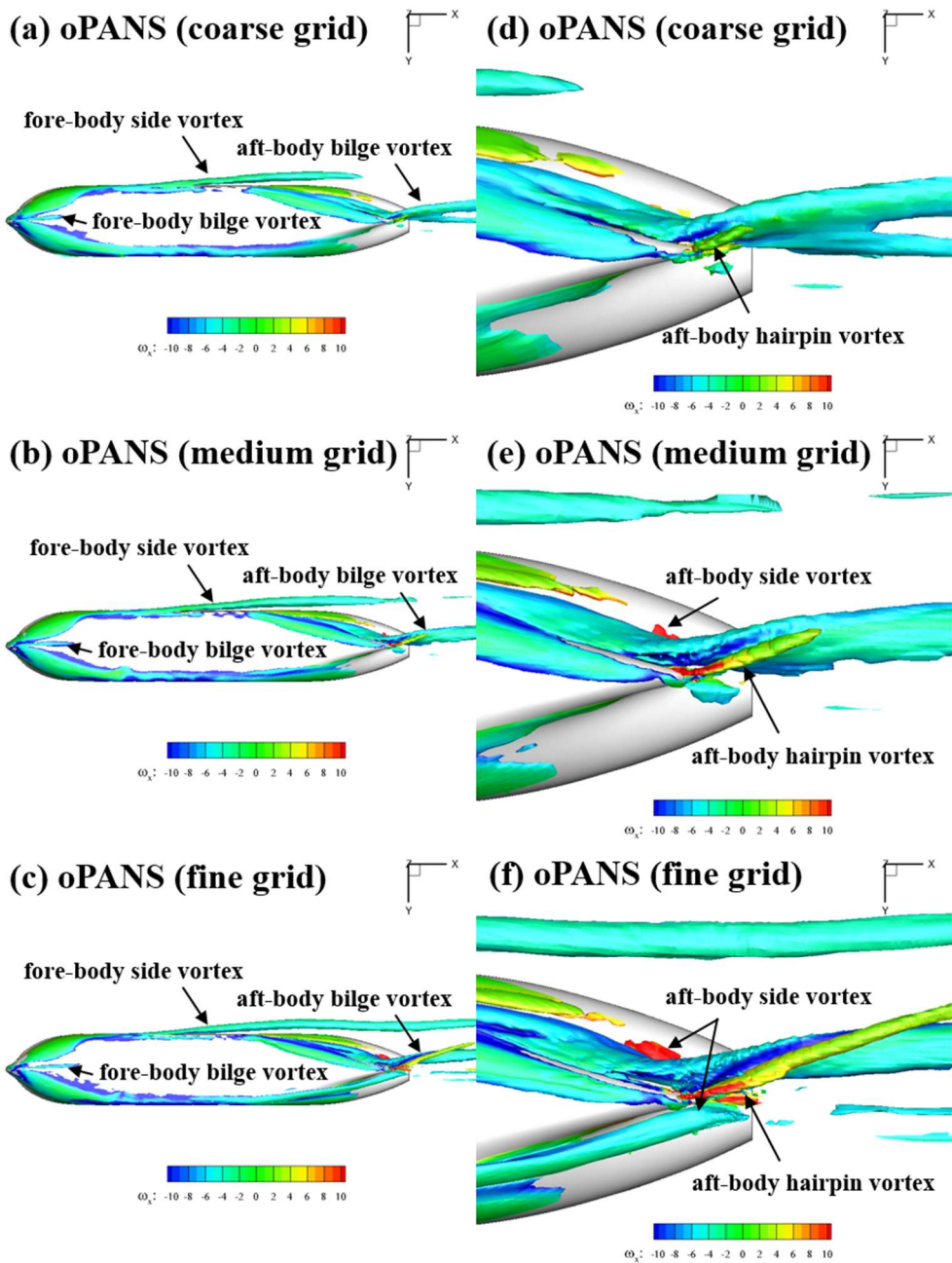


Figure 50 Vortex system around the hull from the oPANS results. Left column: bottom view; Right column: zoom in near the stern

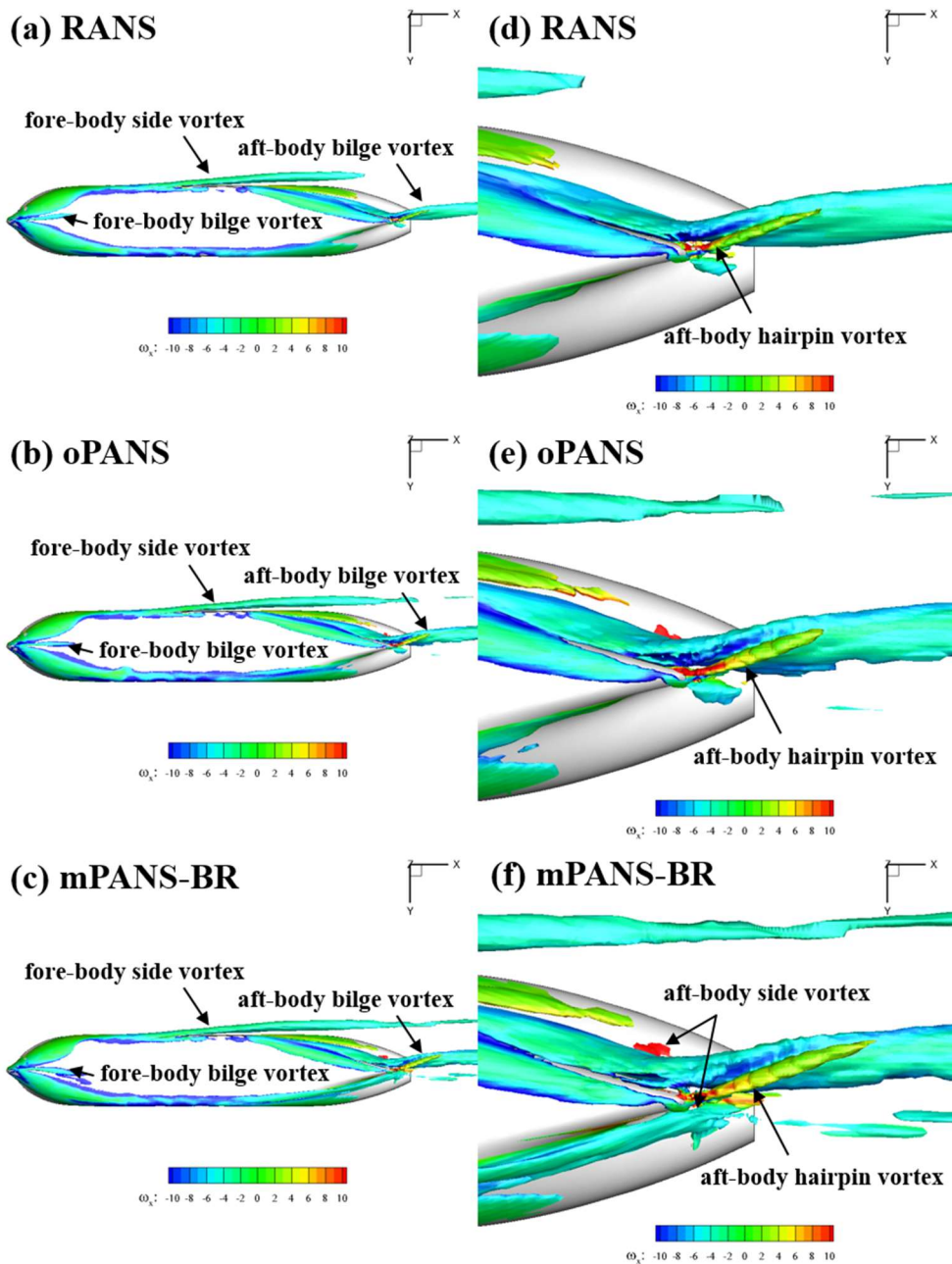


Figure 51 Vortex system around the hull from the RANS, oPANS and mPANS-BR results. Left column: bottom view; Right column: zoom in near the stern

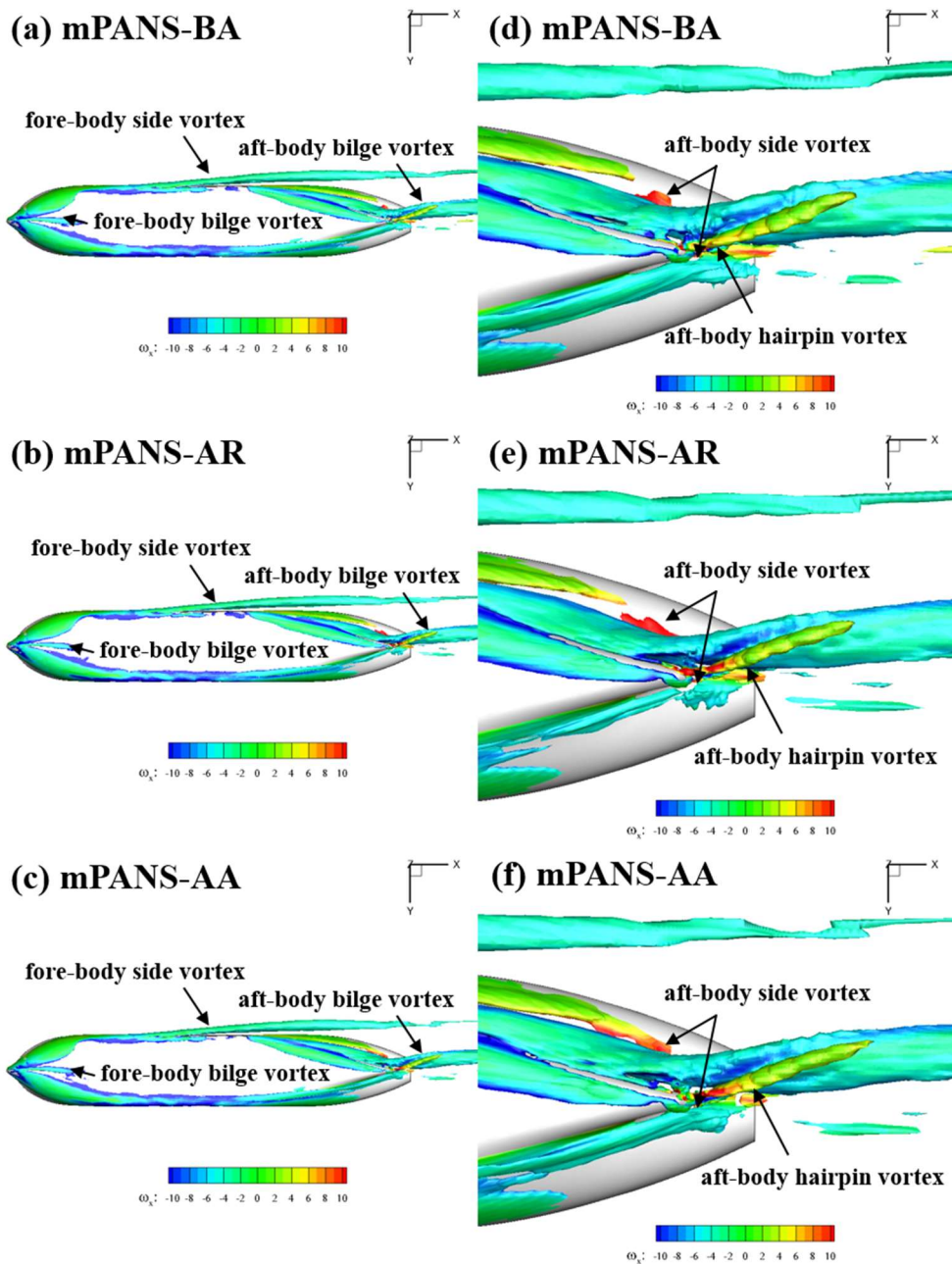
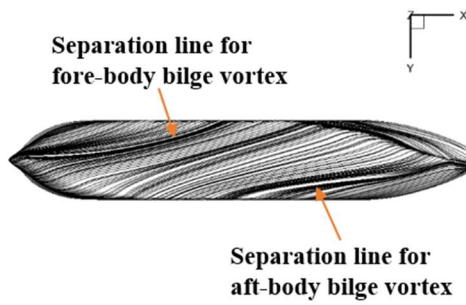


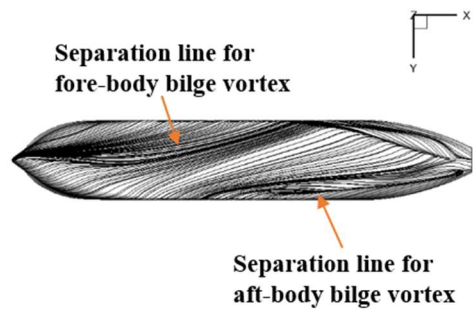
Figure 52 Vortex system around the hull from the mPANS-BA, mPANS-AR and mPANS-AA results. Left column: bottom view; Right column: zoom in near the stern

Figure 53 shows the bottom view of the limiting streamlines at the drift angle of 12° obtained by using the RANS, oPANS models and mPANS-BR, mPANS-BA, mPANS-AR, and mPANS-AA models. They revealed separation lines for the fore-body bilge vortex and aft-body bilge vortex. It can be seen that the results from the mPANS models represented the merge of limiting streamlines toward the windward side. On the other hand, the RANS and oPANS models failed to capture the merge of limiting streamlines. This can be related to the observation that the fore-body bilge vortex was located closer to the hull centerline in the modified PANS predictions. The mPANS models captured the skin friction lines similar to the previous studies (Fureby *et al.*, 2016). Additionally, the instantaneous skin friction lines at the drift angle of 12° are shown in Figures 54 and 55. Although there was a discrepancy in the length of the fore-body side vortex depending on the turbulence model, the separation line for the fore-body side vortex was observed in all numerical simulations, as shown in Figure 55. The mPANS-BR, mPANS-BA, mPANS-AR and mPANS-AA models showed spiral for the aft-body side vortex near the stern in Figure 56, which was observed in Xing *et al.* (2012). These results were related to the observation of aft-body side vortex system, as shown in Figure 53. At a given level of grid resolution., the mPANS models provided an adequate description of aft-body side vortex compared with the oPANS results.

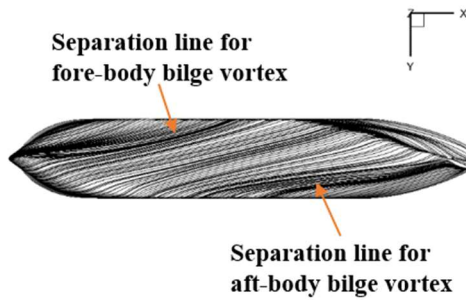
(a) RANS



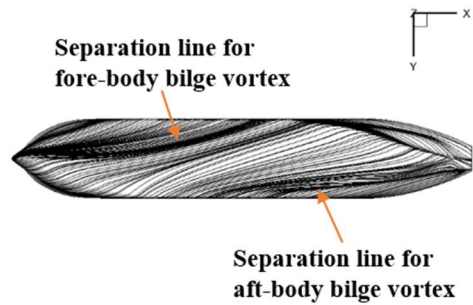
(d) mPANS-BA



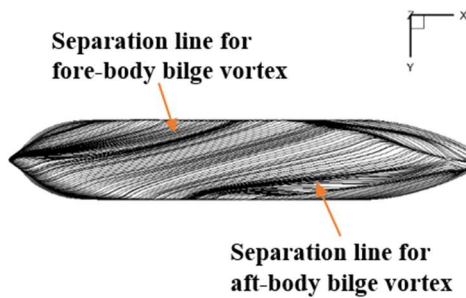
(b) oPANS



(e) mPANS-AR



(c) mPANS-BR



(f) mPANS-AA

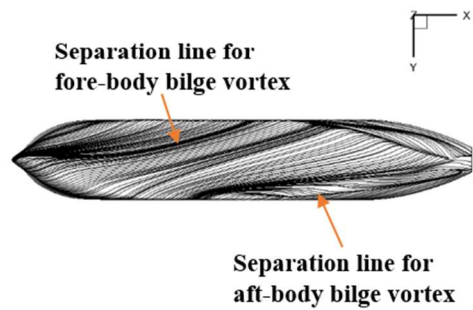


Figure 53 Bottom view of instantaneous skin friction lines from the RANS, oPANS and mPANS-BR, mPANS-BA, mPANS-AR and mPANS-AA results

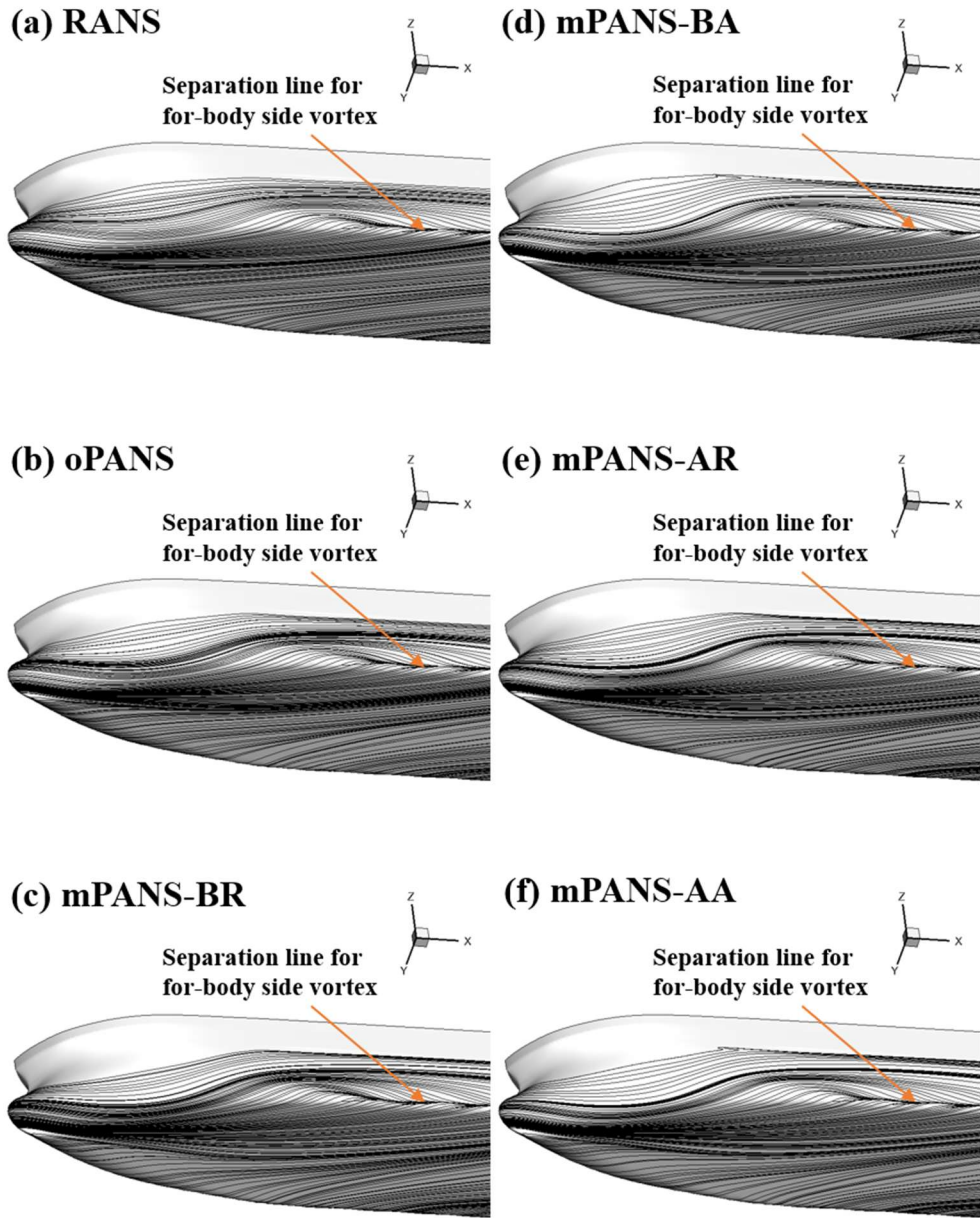


Figure 54 Instantaneous skin friction lines near the bow from the RANS, oPANS and mPANS-BR, mPANS-BA, mPANS-AR and mPANS-AA results

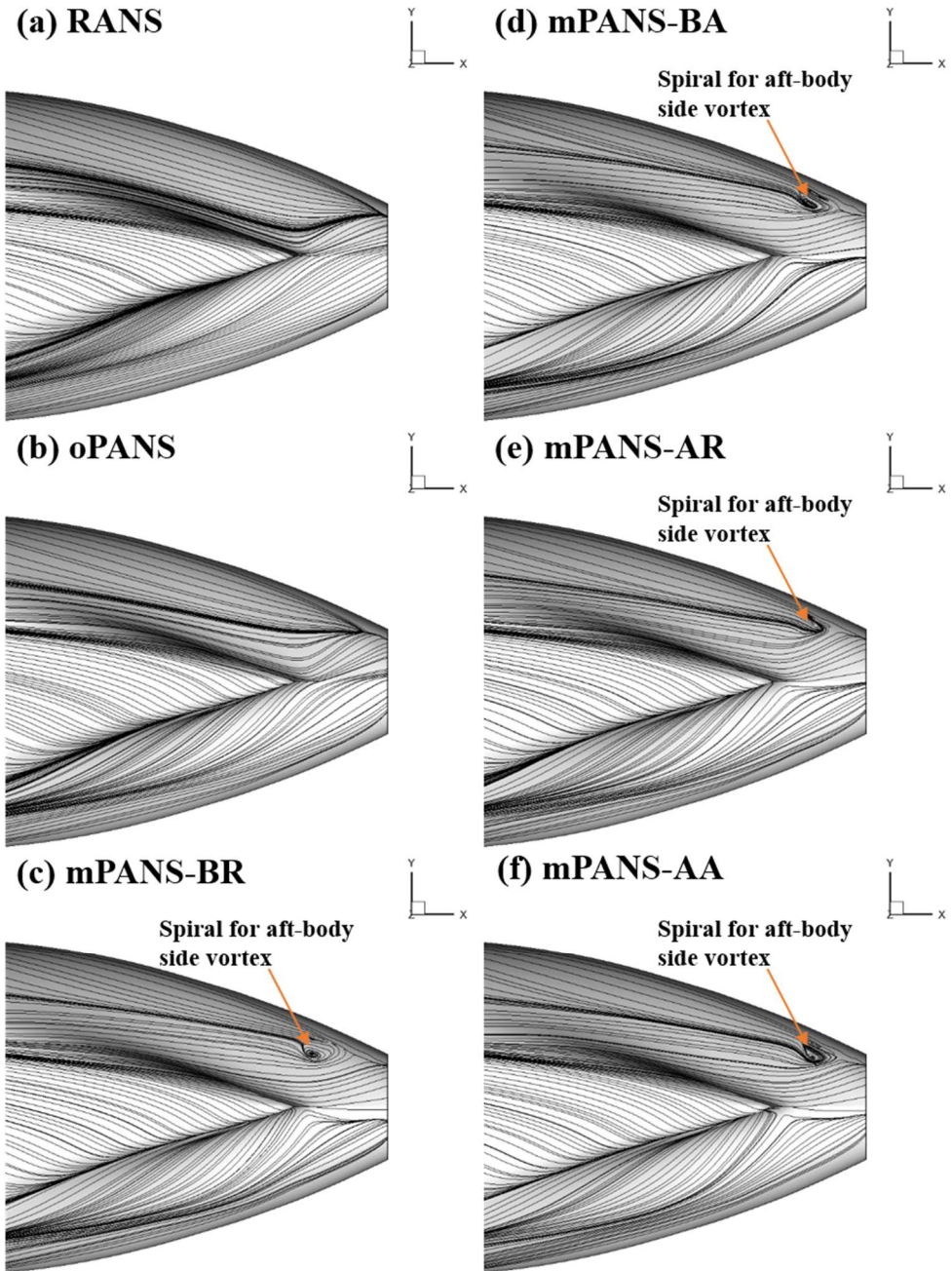


Figure 55 Instantaneous skin friction lines near the stern from the RANS, oPANS and mPANS-BR, mPANS-BA, mPANS-AR and mPANS-AA results

Chapter 5. Summary and Conclusions

In the present study, the modified formulations of the PANS model were suggested for accurate prediction of the turbulent secondary flow on the propeller plane of the KVLCC2. The mPANS models were developed using the open source CFD toolkit OpenFOAM. The main distinctive features of the mPANS models were to resolve the wide range of turbulent length scale by decreasing the f_k value in the region where the anisotropic behavior of turbulence dominates. To procure the information on the region where there is highly anisotropic turbulence exists, the budget analysis, and the anisotropy invariant map were adopted. The level of how much f_k should be reduced in the highly anisotropic region was determined by the model constants.

To assess capability of the mPANS models in predicting the secondary flow, the PANS simulations were performed for the square duct, and the PANS results were compared with the LES, RANS, and the previous DNS results. The simulations showed good agreement with the DNS results. With grid refinement, the statistical values predicted by the PANS models became close to those produced by the DNS. For the coarse grid, the PANS simulations showed closer agreement with the DNS results than the LES results. Therefore, when the relatively coarse grid was used, the PANS models would reproduce more improved results compared to the LES results.

The model constants were determined that can resolve the secondary flow in the square duct using the comparatively coarse grid suitable for the RANS simulation. To identify the reliability of the model constants, the mPANS models were applied to the prolate spheroid and KVLCC2. The mPANS simulations of the turbulent flow around the prolate spheroid with the 10°

angle of attack were conducted. The mPANS results were compared well with the experimental data for the pressure and skin friction coefficients, and it was confirmed that they well predicted the three-dimensional turbulent separated flow behind the prolate spheroid.

The mPANS models were applied to the flow around the KVLCC2 at the drift angles of 0° and 12° . At the drift angle of 0° , the statistical values of total resistance obtained by using the mPANS models were in good agreement (only below 1% deviation) with the experimental data. The mPANS models were applied on the medium grid and showed improved predictions of the hook shape pattern of the streamwise component of velocity on the propeller plane compared with the oPANS results. At the drift angle of 12° , the mPANS models presented reliable results for the forces and moment compared with the experimental data and numerical results obtained from the previous studies. However, the oPANS simulations failed to predict the aft-body side vortex formation as well as long fore-body side vortex formation on the medium grid. To yield accurate results on the medium grid, the mPANS models were applied. The mPANS models achieved to resolve the aft-body side vortex formation and longer fore-body side vortex formation than oPANS results. Thus, the mPANS models showed considerably improved accuracy for predicting the hook shape pattern of low velocity as well as the vortical structures compared with the oPANS results at a given level of physical grid resolution.

References

Abbas, N. and Kornev, N., 2016, "Validation of hybrid URANS/LES methods for determination of forces and wake parameters of KVLCC2 tanker at manoeuvring conditions," *Ship Technology Research*, 63(2), 96-109.

Abdol-Hamid, K. S. and Girimaji, S. S., 2004, "A two-stage procedure toward the efficient implementation of PANS and other hybrid turbulence models," Report No. NASA/TM 2004-213260.

Ahn, S., Choi, K. Y. and Simpson, R., 1989, "The design and development of a dynamic plunge-pitch-roll model mount," *In 27th Aerospace Sciences Meeting*, 48.

Antonia, R. A., Teitel, M., Kim, J. and Browne, L. W. B., 1992, "Low-Reynolds-number effects in a fully developed turbulent channel flow," *Journal of Fluid Mechanics*, 236, 579-605.

Brundrett, E. and Baines, W. D., 1964, "The production and diffusion of vorticity in duct flow," *Journal of Fluid Mechanics*, 19(3), 375-394.

Bhushan, S., Xing, T., Visonneau, M., Wackers, J., Deng, G., Stern, F. and Larsson, L., 2014, "Post Workshop Computations and Analysis for KVLCC2 and 5415." *In Numerical Ship Hydrodynamics*, Springer, Dordrecht, 265-318.

Carrica, P. M., Wilson, R. V. and Stern, F., 2006, "Unsteady RANS simulation of the ship forward speed diffraction problem," *Computers and Fluids*, 35(6), 545-570.

Carrica, P. M., Castro, A. M. and Stern, F., 2010, "Self-propulsion computations using a speed controller and a discretized propeller with

dynamic overset grids,” *Journal of Marine Science and Technology*, 15(4), 316-330.

Catalano, P., Wang, M., Iaccarino, G. and Moin, P., 2003, “Numerical simulation of the flow around a circular cylinder at high Reynolds numbers,” *International Journal of Heat and Fluid Flows*, 24(4), 463-469.

Chesnakas, C. J., Taylor, D. and Simpson, R. L., 1997, “Detailed investigation of the three-dimensional separation about a 6: 1 prolate spheroid,” *AIAA Journal*, 35(6), 990-999.

Choi, H. and Moin, P., 2012, “Grid-point requirements for large eddy simulation: Chapman’s estimates revisited,” *Physics of Fluids*, 24(1), 011702.

Craft, T. J., Launder, B. E. and Suga, K., 1997, “Prediction of turbulent transitional phenomena with a nonlinear eddy-viscosity mode,” *International Journal of Heat and Fluid Flow*, 18(1), 15-28.

Davidson, L. and Peng, S. H., 2003, “Hybrid LES-RANS modeling: a one-equation SGS model combined with a $k-\omega$ model for predicting recirculating flows,” *International Journal for Numerical Methods in Fluids*, 43(9), 1003-1018.

Deng, G. B., Queutey, P., and Visonneau, M., 1994, “Navier-Stokes computations of ship stern flows: a detailed comparative study of turbulence models and discretization schemes,” *Proceedings, 6th Symposium on Numerical Ship Hydrodynamics*, Iowa City, Iowa.

Demuren, A. O. and Rodi, W., 1984, “Calculation of turbulence-driven secondary motion in non-circular ducts,” *Journal of Fluid Mechanics*, 140, 189-222.

Domaradzki, J. A., Liu, W., Härtel, C. and Kleiser, L., 1994, “Energy transfer in numerically simulated wall-bounded turbulent flows,” *Physics of Fluids*, 6(4), 1583-1599.

Foroutan, H. and Yavuzkurt, S., 2014, “A partially-averaged Navier–Stokes model for the simulation of turbulent swirling flow with vortex breakdown,” *International Journal of Heat and Fluid Flow*, 50, 402-416.

Frendi, A., Tosh, A. and Girimaji, S., 2006, “Flow past a backward-facing step: comparison of PANS, DES and URANS results with experiments,” *International Journal for Computational Methods in Engineering Science and Mechanics*, 8(1), 23-38.

Fureby, C. and Karlsson, A., 2009, “LES of the Flow Past a 6: 1 Prolate Spheroid,” *In 47th AIAA Aerospace Sciences Meeting including The New Horizons Forum and Aerospace Exposition*, Orlando, Florida, January 5-8.

Fureby, C., Toxopeus, S. L., Johansson, M., Tormalm, M. and Petterson, K., 2016, “A computational study of the flow around the KVLCC2 model hull at straight ahead conditions and at drift,” *Ocean Engineering*, 118, 1-16.

Gaggero, S., Tani, G., Viviani, M. and Conti, F., 2014, “A study on the numerical prediction of propellers cavitating tip vortex,” *Ocean Engineering*, 92, 137-161.

Gaggero, S., Villa, D. and Viviani, M., 2017, “An extensive analysis of numerical ship self-propulsion prediction via a coupled BEM/RANS approach,” *Applied Ocean Research*, 66, 55-78.

Gavrilakis, S., 1992, “Numerical simulation of low-Reynolds-number turbulent flow through a straight square duct,” *Journal of Fluid Mechanics*, 244, 101-129.

Germano, M., 1999, "From RANS to DNS: towards a bridging model," In *Direct and Large-Eddy Simulation III*, 225-236, Springer, Dordrecht.

Gessner, F. B., 1973, "The origin of secondary flow in turbulent flow along a corner," *Journal of Fluid Mechanics*, 58(1), 1-25.

Ghassemi, H., 2009, "The effect of wake flow and skew angle on the ship propeller performance," *Transaction B: Mechanical Engineering*, 16(2), 149–158.

Girimaji, S. S., 2006, "Partially-averaged Navier-Stokes model for turbulence: A Reynolds-averaged Navier-Stokes to direct numerical simulation bridging method," *Journal of Applied Mechanics*, 73(3), 413-421.

Girimaji, S. S. and Abdol-Hamid, K., 2005, "Partially-averaged Navier Stokes model for turbulence: Implementation and validation," In *43rd AIAA Aerospace Sciences Meeting and Exhibit*, Reno, Nevada, January 10-13.

Hino, T., 2005, "Proceedings of CFD workshop Tokyo 2005," Tokyo, Japan.

Hoang, N., Wetzel, T. and Simpson, R., 1994, "Surface pressure measurements over a 6: 1 prolate spheroid undergoing time-dependent maneuvers," In *12th Applied Aerodynamics Conference*, Colorado, USA.

Hunt, J. C. R. and Graham, J. M. R., 1978, "Free-stream turbulence near plane boundaries," *Journal of Fluid Mechanics*, 84(2), 209-235.

Huse, E., 1972, "Pressure Fluctuation on the Hull Induced by Cavitating Propeller," *Norwegian Ship Model Experiment Tank Publication*, 111.

Ismail, F., Carrica, P. M., Xing, T. and Stern, F., 2010, "Evaluation of linear and nonlinear convection schemes on multidimensional non-orthogonal grids with applications to KVLCC2 tanker," *International Journal for Numerical*

Methods in Fluids, 64(8), 850-886.

Jeong, E. and Girimaji, S. S., 2010, "Partially averaged Navier–Stokes (PANS) method for turbulence simulations—Flow past a square cylinder," *Journal of Fluids Engineering*, 132(12), 121203.

Jovanovic, J., 2013, "The statistical dynamics of turbulence," Springer Science & Business Media.

Kajishima, T. and Miyake, Y., 1992, "A discussion on eddy viscosity models on the basis of the large eddy simulation of turbulent flow in a square duct," *Computers and Fluids*, 21, 151-161.

Kim, J., Moin, P. and Moser, R., 1987, "Turbulence statistics in fully developed channel flow at low Reynolds number," *Journal of Fluid Mechanics*, 177, 133-166.

Kim, W. J., Van, S. H. and Kim, D. H., 2001, "Measurement of flows around modern commercial ship models" *Experiments in Fluids*, 31(5), 567-578.

Kim, W. J., Kim, D. H. and Van, S. H., 2002, "Computational study on turbulent flows around modern tanker hull forms," *International Journal for Numerical Methods in Fluids*, 38(4), 377-406.

Krajnović, S., Lárusson, R. and Basara, B., 2012, "Superiority of PANS compared to LES in predicting a rudimentary landing gear flow with affordable meshes," *International Journal of Heat and Fluid Flow*, 37, 109-122.

Krajnović, S. and Minelli, G., 2015, "Status of PANS for bluff body aerodynamics of engineering relevance," *In Progress in Hybrid RANS-LES Modelling*, 399-410, Springer.

Kume, K., Hasegawa, J., Tsukada, Y., Fujisawa, J., Fukasawa, R. and Hinatsu, M., 2006, “Measurements of hydrodynamic forces, surface pressure, and wake for obliquely towed tanker model and uncertainty analysis for CFD validation,” *Journal of Marine Science and Technology*, 11(2), 65-75.

Lakshmipathy, S. and Girimaji, S. S., 2006, “Partially-averaged Navier-Stokes method for turbulent flows: kw model implementation,” *In 44th AIAA Aerospace Sciences Meeting and Exhibit*, 119.

Lakshmipathy, S. and Girimaji, S. S., 2010, “Partially averaged Navier–Stokes (PANS) method for turbulence simulations: flow past a circular cylinder,” *Journal of Fluids Engineering*, 132(12), 121202.

Lakshmipathy, S. and Togiti, V., 2011, “Assessment of alternative formulations for the specific-dissipation rate in RANS and variable-resolution turbulence models,” *In 20th AIAA Computational Fluid Dynamics Conference*, Honolulu, Hawaii, June 27-30.

Larsson, L., Stern, F. and Bertram, V., 2003, “Benchmarking of Computational Fluid Dynamics for Ship Flows: The Gothenburg 2000 Workshop,” *Journal of Ship Research*, 47(1), 63-81.

Larsson, L., Stern, F. and Visonneau, M., 2013, “CFD in ship hydrodynamics—results of the Gothenburg 2010 workshop,” *In MARINE 2011, IV International Conference on Computational Methods in Marine Engineering*, 237-259, Springer, Dordrecht.

Larsson, L., Stern, F. and Visonneau, M., 2013, “Numerical ship hydrodynamics: an assessment of the Gothenburg 2010 workshop,” Springer, Netherlands.

Launder, B. E. and Ying, W. M., 1973, “Prediction of flow and heat transfer in

ducts of square cross-section,” *Proceedings of the Institution of Mechanical Engineers*, 187(1), 455-461.

Launder, B. E., Reece, G. J. and Rodi, W., 1975, “Progress in the development of a Reynolds-stress turbulence closure,” *Journal of Fluid Mechanics*, 68(3), 537-566.

Launder, B. E. and Spalding, D. B., 1983, “The numerical computation of turbulent flows,” *Numerical Prediction of Flow, Heat Transfer, Turbulence and Combustion*, 96-116.

Lee, M. and Moser, R. D., 2019, “Spectral analysis of the budget equation in turbulent channel flows at high Reynolds number,” *Journal of Fluid Mechanics*, 860, 886-938.

Lee, S. J., Kim, H. R., Kim, W. J. and Van, S. H., 2003, “Wind tunnel tests on flow characteristics of the KRISO 3,600 TEU containership and 300K VLCC double-deck ship models,” *Journal of Ship Research*, 47(1), 24-38.

Li, D.-Q., 2006, “Validation of RANS predictions of open water performance of a highly skewed propeller with experiments,” *Journal of Hydrodynamics*, Ser. B, 18(3), 520-528.

Lumley, J. L., 1964, “The spectrum of nearly inertial turbulence in a stably stratified fluid,” *Journal of the Atmospheric Sciences*, 21(1), 99-102.

Lumley, J. L. and Newman, G. R., 1977, “The return to isotropy of homogeneous turbulence,” *Journal of Fluid Mechanics*, 82(1), 161-178.

Lumley, J. L., 1979, “Computational modeling of turbulent flows,” *Advances in Applied Mechanics*, 18, 123-176.

Luo, D., Yan, C., Liu, H. and Zhao, R., 2014, “Comparative assessment of

PANS and DES for simulation of flow past a circular cylinder,” *Journal of Wind Engineering and Industrial Aerodynamics*, 134, 65-77.

Nakos, D. E. and Sclavounos, P. D., 1990, “On steady and unsteady ship wave patterns,” *Journal of Fluid Mechanics*, 215, 263-288.

Naot, D. and Rodi, W., 1982, “Calculation of secondary currents in channel flow,” *Journal of the Hydraulics Division*, 108(8), 948-968.

Newman, J. N., 1987, “Evaluation of the wave-resistance Green function: Part 1—The double integral,” *Journal of Ship Research*, 31(2), 79-90.

Nikitin, N. V., Nicoud, F., Wasistho, B., Squires, K. D. and Spalart, P. R., 2000, “An approach to wall modeling in large-eddy simulations,” *Physics of Fluids*, 12(7), 1629-1632.

Nikuradse, J., 1926, “Untersuchung über die Geschwindigkeitsverteilung in turbulenten Strömungen.” Thesis, Gottingen, V.D.I.-Forsch..

Nisizima, S., 1990, “A numerical study of turbulent square-duct flow using an anisotropic k- ϵ model,” *Theoretical and Computational Fluid Dynamics*, 2(1), 61-71.

Madabhushi, R. K. and Vanka, S. P., 1991, “Large eddy simulation of turbulence-driven secondary flow in a square duct,” *Physics of Fluids A: Fluid Dynamics*, 3(11), 2734-2745.

Marquillie, M., Ehrenstein, U. and Laval, J. P., 2011, “Instability of streaks in wall turbulence with adverse pressure gradient,” *Journal of Fluid Mechanics*, 681, 205-240.

McCroskey, W. J., 1977, “Some current research in unsteady fluid dynamics,” *Journal of Fluids Engineering*, 99(1), 8-39.

Melling, A. and Whitelaw, J. H., 1976, "Turbulent flow in a rectangular duct," *Journal of Fluid Mechanics*, 78(2), 289-315.

Menter, F. R., 1992, "Influence of freestream values on k-omega turbulence model predictions," *AIAA Journal*, 30(6), 1657-1659.

Menter, F. R., 1994, "Two-equation eddy-viscosity turbulence models for engineering applications," *AIAA Journal*, 32(8), 1598-1605.

Menter, F. R., 1997, "Eddy viscosity transport equations and their relation to the k- ϵ model," *Journal of Fluids Engineering*, 119, 876-884.

Muzaferija S., 1999, "A two-fluid Navier-Stokes solver to simulate water entry," *Proceedings of Twenty-Second Symposium on Naval Hydrodynamics*, Washington, DC, 638-651.

Oyewola, O., Djenidi, L. and Antonia, R. A., 2004, "Influence of localised wall suction on the anisotropy of the Reynolds stress tensor in a turbulent boundary layer," *Experiments in Fluids*, 37(2), 187-193.

Pereira, F. S., Eça, L. and Vaz, G., 2017, "Verification and Validation exercises for the flow around the KVLCC2 tanker at model and full-scale Reynolds numbers," *Ocean Engineering*, 129, 133-148.

Peyret, R. and Krause, E., 2000, "Advanced turbulent flow computations," Springer Wein, New York.

Pinelli, A., Uhlmann, M., Sekimoto, A. and Kawahara, G., 2010, "Reynolds number dependence of mean flow structure in square duct turbulence," *Journal of Fluid Mechanics*, 644, 107-122.

Pope, S. B., 1975, "A more general effective-viscosity hypothesis," *Journal of Fluid Mechanics*, 72(2), 331-340.

Pope S. B., 2000, “Turbulent Flows,” Cambridge University Press, Cambridge, UK.

PRANDTL, L., 1926, “Über die ausgebildete Turbulenz,” In Verh. 2nd Int. Kong. Tech. Mech. Zürich, (English translation, NACA technical memoir), 435, 62–75.

Rahman, M. M. and Siikonen, T., 2006, “An explicit algebraic Reynolds stress model in turbulence,” *International Journal for Numerical Methods in Fluids*, 52(10), 1135-1157.

Raiesi, H., Piomelli, U. and Pollard, A., 2011, “Evaluation of turbulence models using direct numerical and large-eddy simulation data,” *Journal of Fluids Engineering*, 133(2), 021203.

Rhee, S. H. and Hino, T., 2000, “Computational investigation of 3D turbulent flow separation around a spheroid using an unstructured grid method,” *Journal of the Society of Naval Architects of Japan*, 188, 1-9.

Roache, P. J., 1994, “Perspective: a method for uniform reporting of grid refinement studies,” *ASME Journal of Fluids Engineering*, 116.

Roache, P. J., 1998, “Verification and validation in computational science and engineering,” Hermosa Publisher, Albuquerque.

Rodi, W., 1976, “A new algebraic relation for calculating the Reynolds stresses,” *Z. Argew. Math. Mech.* 56, T219–T221.

Schlatter, P., Örlü, R., Li, Q., Brethouwer, G., Fransson, J. H., Johansson, A. V., Alfredsson, P. H. and Henningson, D. S., 2009, “Turbulent boundary layers up to $Re_\theta = 2500$ studied through simulation and experiment,” *Physics of Fluids*, 21(5), 051702.

Scott, N. and Duque, E., 2005, "Using detached eddy simulation and overset grids to predict flow around a 6: 1 prolate spheroid," *In 43rd AIAA Aerospace Sciences Meeting and Exhibit*, Reno, Nevada, January 10-13.

Seo, J. H., Seol, D. M., Lim, T. G., Park, S. T., Han, B. W. and Rhee, S. H., 2013, "A stereo PIV measurement of a model ship wake in a towing tank with uncertainty assessment", *In: Proceedings of the 10th International Symposium on Particle Image Velocimetry (PIV13)*, Delft, The Netherlands.

Seo, J., Seol, D. M., Han, B. W., Yoo, G., Lim, T. G., Park, S. T. and Rhee, S. H., 2014, "Uncertainty Assessment of a Towed Underwater Stereoscopic PIV System," *Journal of the Society of Naval Architects of Korea*, 51(4), 311-320 (in Korean).

Seo, J., Seol, D. M., Han, B. and Rhee, S. H., 2016, "Turbulent wake field reconstruction of VLCC models using two-dimensional towed underwater PIV measurements," *Ocean Engineering*, 118, 28-40.

Sharma, D., 1974, "Turbulent convective phenomena in straight rectangular-sectioned diffusers, Ph.D. Thesis, University of London.

Shin, S. H., 2015, "Effects of propeller forces on the propeller shaft bearing during going straight and turning of ship," *Journal of the Society of Naval Architects of Korea*, 52(1), 61-69 (in Korean).

Song, C. S. and Park, S. O., 2009, "Numerical simulation of flow past a square cylinder using partially-averaged Navier–Stokes model," *Journal of Wind Engineering and Industrial Aerodynamics*, 97(1), 37-47.

Spalart, P. R., 1997, "Comments on the feasibility of LES for wings, and on a hybrid RANS / LES approach," *In Proceedings of first AFOSR international conference on DNS / LES*, Greyden Press.

Spalart, P. R., 1988, "Direct simulation of a turbulent boundary layer up to $Re_\theta = 1410$," *Journal of Fluid Mechanics*, 187, 61-98.

Stern, F., Agdrup, K., Kim, S. Y., Hochbaum, A. C., Rhee, K. P., Quadvlieg, F., Perdon, P.; Hino, T.; Broglia, R. and Gorski, J., 2011, "Experience from SIMMAN 2008—the first workshop on verification and validation of ship maneuvering simulation methods" *Journal of Ship Research*, 55(2), 135-147.

Stern, F., Sadat-Hosseini, H., Mousaviraad, M. and Bhushan, S., 2014, "Evaluation of seakeeping predictions. In Numerical Ship Hydrodynamics," Springer, Dordrecht, 141-202.

Speziale, C. G., 1987, "On nonlinear k_l and $k-\epsilon$ models of turbulence," *Journal of Fluid Mechanics*, 178, 459-475.

Speziale, C. G., 1998, "Turbulence modeling for time-dependent RANS and VLES: A review," *AIAA Journal*, 36, 173–184.

Strelets, M., 2001, "Detached eddy simulation of massively separated flows," *39th AIAA Aerospace Sciences Meeting*, Reno, Nevada, January 8-11.

Sung, Y. J. and Park, S.-H., 2015. "Prediction of Ship Maneuvering Performance Based on Virtual captive Model Tests," *Journal of the Society of Naval Architects of Korea*, 52(5), 407-417.

Tsai, C. Y. and Whitney, A., 1999, "Numerical study of three-dimensional flow separation for a 6: 1 ellipsoid," *In 37th Aerospace Sciences Meeting and Exhibit*, Reno, Nevada, January 11-14.

Uhlmann, M., Pinelli, A., Kawahara, G. and Sekimoto, A., 2007, "Marginally turbulent flow in a square duct," *Journal of Fluid Mechanics*, 588, 153-162.

Van Leer, B., 1979, "Towards the ultimate conservative difference scheme. V.

A second-order sequel to Godunov's method," *Journal of Computational Physics*, 32(1), 101-136.

Vartdal, B. J., Gjestland, T. and Arvidsen, T. I., 2009, "Lateral propeller forces and their effects on shaft bearings," *In First International Symposium on Marine Propulsors*, Trondheim, Norway, June 22-24.

Wetzel, T. G. and Simpson, R. L., 1998, "Unsteady crossflow separation location measurements on a maneuvering 6: 1 prolate spheroid," *AIAA Journal*, 36(11), 2063-2071.

Wilcox, D. C., 1993, "Comparison of two-equation turbulence models for boundary layers with pressure gradient," *AIAA Journal*, 31(8), 1414-1421.

Wilcox, D. C., 1988, "Reassessment of the scale-determining equation for advanced turbulence models," *AIAA Journal*, 26(11), 1299-1310.

Xiao, Z., Chen, H., Zhang, Y. and Fu, S., 2006, "Prediction for separation flows around a 6: 1 prolate spheroid using hybrid RANS/LES methods," *In 44th AIAA Aerospace Sciences Meeting and Exhibit*, Reno, Nevada, January 9-12.

Xing, T., Bhushan, S. and Stern, F., 2012, "Vortical and turbulent structures for KVLCC2 at drift angle 0, 12, and 30 degrees," *Ocean Engineering*, 55, 23-43.

Xu, H. and Pollard, A., 2001, "Large eddy simulation of turbulent flow in a square annular duct," *Physics of Fluids*, 13(11), 3321-3337.

Xu, H., 2009, "Direct numerical simulation of turbulence in a square annular duct," *Journal of Fluid Mechanics*, 621, 23-57.

Yoshizawa, A., 1984, "Statistical analysis of the deviation of the Reynolds

stress from its eddy-viscosity representation,” *Physics of Fluids*, 27(6), 1377-1387.

Zhang, H., Trias, F. X., Gorobets, A., Tan, Y. and Oliva, A., 2015, “Direct numerical simulation of a fully developed turbulent square duct flow up to $Re_\tau = 1200$,” *International Journal of Heat and Fluid Flow*, 54, 258-267.

초 록

본 연구에서는 주어진 격자에서 KVLCC2 선형의 프로펠러 면에서의 난류 2차 흐름을 정도 높게 모사하기 위해 개선된 PANS 모델을 제안한다. 이를 위해 소스코드가 공개된 OpenFOAM 을 이용하였으며, 해석된 결과를 모형 시험 결과와 비교하여 개선된 PANS 모델의 유효성을 확인하였다.

주어진 KVLCC2 격자에서 기존 PANS 모델을 이용하여 해석된 결과를 모형 시험 결과와 비교하였을 때 프로펠러 면에서 약한 hook 모양이 관찰되었다. 기존 PANS 모델은 Luo *et al.* (2014)가 제안한 공간상에서 변화하는 제어 변수 (f_k) 함수로서 난류가 국부적으로 등방성을 보인다는 가정을 기반한다. 많은 연구들에서 비등방적인 난류 모델이 정확한 hook 모양을 모사한 사례를 보여주고 있으며, 결과적으로 KVLCC2 의 프로펠러면에서의 hook 모양을 모사하는데 있어 난류의 비등방성은 중요한 역할을 한다고 생각할 수 있다. 따라서 난류의 비등방성이 높은 영역에서 더 많은 스케일의 난류 구조를 모사하기 위해 해당 영역에 f_k 를 감소시켰다. 난류의 비등방성이 높은 영역은 budget analysis 와 anisotropy invariant map 을 이용하여 확인하며, f_k 가 감소되는 정도는 모델 상수로 결정된다.

2 차 흐름을 추정하는데 있어 개선된 PANS 모델의 유효성을 확인하기 위해 사각 덕트에 대해 전산유체역학 해석을 수행하였다. 기존 연구 결과인 DNS 결과와 비교하였으며, PANS 결과는

DNS 결과와 유사한 속도 분포를 보였다. 하지만 DNS 결과와 비교를 위해 생성된 격자는 벽 근처에서 과밀한 격자로 인해 과도한 해석 시간을 요구됨에 따라 산업체에서 RANS 해석용으로 사용하기 어렵다. 따라서 사각 덕트에 대해 RANS 해석을 위한 격자를 생성하였으며, 기존 PANS 모델을 이용하여 전산유체역학 해석을 수행하였다. 하지만 기존 PANS 모델은 사각 덕트 내부의 2 차 흐름을 모사하는데 실패하였다. 따라서 RANS 해석용 격자에서 2 차 흐름을 모사할 수 있는 모델 상수를 결정하였으며, 결정된 모델 상수를 개선된 PANS 모델에 적용하였다.

프로펠러면에서의 저속 hook 모양은 선미의 기하학적인 변화로 인한 압력 구배로 발생한 선미 빌지 보오텍스로 인해 생성된다. 그러나 이는 사각 덕트 내부에서 발생하는 2 차 흐름의 발생 메커니즘과 차이가 있다. 따라서 압력 구배로 인해 발생하는 2 차 흐름을 발생시키는 메커니즘을 가지는 단순한 형상에 대해 개선된 PANS 모델을 적용하여 앞서 결정된 모델 상수의 유효성을 확인해야한다. 이를 위해 10 도 기울어진 prolate spheroid 에 대해 개선된 PANS 해석을 수행하였다. 모형 시험 결과와 비교하였을 때 prolate spheroid 주위에서 발생하는 2 차 흐름 뿐만 아니라 압력 및 마찰 계수들도 유사하게 추정하였다.

또한 개선된 PANS 모델을 이용하여 사향각 0 도와 12 도에서 KVLCC2 주위 유동장 해석에 적용하였다. 사향각 0 도에서, 개선된 PANS 모델로부터 계산된 저항은 모형 시험 결과와 매우 잘 일치하였다. 게다가 주어진 격자에서 개선된 PANS 모델은 기존 PANS 모델과 비교하였을 때 모형 시험과 유사한 hook 모양을

예측하였다. 사항각 12 도에서, 개선된 PANS 모델은 모형 시험 및 다른 전산해석결과들과 비교를 통해 무차원화된 힘과 모멘트에 대한 신뢰할 수 있는 결과를 제공함을 확인하였다. 게다가 개선된 PANS 모델은 기존 PANS 모델과 비교하였을 때 hook 모양뿐만 아니라 선체 주위의 와 구조를 정도 높게 모사하였다.

주요어: 2 차 흐름, 비등방성, PANS 방정식, 전산유체역학, 난류 모델

학번: 2016-37764